

Planck early results. VI. The High Frequency Instrument data processing[★]

Planck HFI Core Team^{**}: P. A. R. Ade⁵², N. Aghanim²⁹, R. Ansari⁴⁴, M. Arnaud⁴⁰, M. Ashdown^{38,3}, J. Aumont²⁹, A. J. Banday^{57,6,46}, M. Bartelmann^{56,46}, J. G. Bartlett^{2,36}, E. Battaner⁵⁹, K. Benabed³⁰, A. Benoît²⁸, J.-P. Bernard^{57,6}, M. Bersanelli^{18,23}, J. J. Bock^{36,7}, J. R. Bond⁵, J. Borrill^{45,54}, F. R. Bouchet³⁰, F. Boulanger²⁹, T. Bradshaw⁵⁰, M. Bucher², J.-F. Cardoso^{41,2,30}, G. Castex², A. Catalano^{2,39}, A. Challinor^{34,38,8}, A. Chamballu²⁶, R.-R. Chary²⁷, X. Chen²⁷, C. Chiang¹³, S. Church⁵⁵, D. L. Clements²⁶, J.-M. Colley^{2,1}, S. Colombi³⁰, F. Couchot⁴⁴, A. Coullais³⁹, C. Cressiot², B. P. Crill^{36,48}, M. Crook⁵⁰, P. de Bernardis¹⁷, J. Delabrouille², J.-M. Delouis³⁰, F.-X. Désert²⁵, K. Dolag⁴⁶, H. Dole²⁹, O. Doré^{36,7}, M. Douspis²⁹, J. Dunkley¹⁶, G. Efstathiou³⁴, C. Filliard⁴⁴, O. Forni^{57,6}, P. Fosalba³¹, K. Ganga^{2,27}, M. Giard^{57,6}, D. Girard⁴³, Y. Giraud-Héraud², R. Gispert²⁹, K. M. Górski^{36,61}, S. Gratton^{38,34}, M. Griffin⁵², G. Guyot²⁴, J. Haissinski⁴⁴, D. Harrison^{34,38}, G. Helou⁷, S. Henrot-Versillé⁴⁴, C. Hernández-Monteaigudo⁴⁶, S. R. Hildebrandt^{7,43,35}, R. Hills³, E. Hivon³⁰, M. Hobson³, W. A. Holmes³⁶, K. M. Huffenberger⁶⁰, A. H. Jaffe²⁶, W. C. Jones¹³, J. Kaplan², R. Kneissl^{19,4}, L. Knox¹⁴, M. Kunz^{11,29}, G. Lagache²⁹, J.-M. Lamarre³⁹, A. E. Lange²⁷, A. Lasenby^{3,38}, A. Lavabre⁴⁴, C. R. Lawrence³⁶, M. Le Jeune², C. Leroy^{29,57,6}, J. Lesgourgues³⁰, J. F. Macías-Pérez⁴³, C. J. MacTavish³⁸, B. Maffei³⁷, N. Mandolesi²², R. Mann⁵¹, F. Marleau¹², D. J. Marshall^{57,6}, S. Masi¹⁷, T. Matsumura⁷, I. McAuley⁴⁷, P. McGehee²⁷, J.-B. Melin⁹, C. Mercier²⁹, S. Mitra³⁶, M.-A. Miville-Deschênes^{29,5}, A. Moneti³⁰, L. Montier^{57,6}, D. Mortlock²⁶, A. Murphy⁴⁷, F. Nati¹⁷, C. B. Netterfield¹², H. U. Nørgaard-Nielsen¹⁰, C. North⁵², F. Novello²⁹, D. Novikov²⁶, S. Osborne⁵⁵, F. Pajot²⁹, G. Patanchon², T. Peacocke⁴⁷, T. J. Pearson^{7,27}, O. Perdereau⁴⁴, L. Perotto⁴³, F. Piacentini¹⁷, M. Piat², S. Plaszczynski⁴⁴, E. Pointecouteau^{57,6}, N. Ponthieu²⁹, G. Prézeau^{7,36}, S. Prunet³⁰, J.-L. Puget²⁹, W. T. Reach⁵⁸, M. Remazeilles², C. Renault⁴³, A. Riazuelo³⁰, I. Ristorcelli^{57,6}, G. Rocha^{36,7}, C. Rosset², G. Roudier², M. Rowan-Robinson²⁶, B. Rusholme²⁷, R. Saha³⁶, D. Santos⁴³, G. Savini⁴⁹, B. M. Schaefer⁵⁶, P. Shellard⁸, L. Spencer⁵², J.-L. Starck^{40,9}, V. Stolyarov³, R. Stompor², R. Sudiwala⁵², R. Sunyaev^{46,53}, D. Sutton^{34,38}, J.-F. Sygnet³⁰, J. A. Tauber²⁰, C. Thum³³, J.-P. Torre²⁹, F. Touze⁴⁴, M. Tristram⁴⁴, F. Van Leeuwen³⁴, L. Vibert²⁹, D. Vibert⁴², L. A. Wade³⁶, B. D. Wandelt^{30,15}, S. D. M. White⁴⁶, H. Wiesemeyer³², A. Woodcraft⁵², V. Yurchenko⁴⁷, D. Yvon⁹, and A. Zacchei²¹

(Affiliations can be found after the references)

Received 7 January 2011 / Accepted 20 July 2011

ABSTRACT

We describe the processing of the 336 billion raw data samples from the High Frequency Instrument (HFI) which we performed to produce six temperature maps from the first 295 days of *Planck*-HFI survey data. These maps provide an accurate rendition of the sky emission at 100, 143, 217, 353, 545 and 857 GHz with an angular resolution ranging from 9.9 to 4.4'. The white noise level is around 1.5 μ K degree or less in the 3 main CMB channels (100–217 GHz). The photometric accuracy is better than 2% at frequencies between 100 and 353 GHz and around 7% at the two highest frequencies. The maps created by the HFI Data Processing Centre reach our goals in terms of sensitivity, resolution, and photometric accuracy. They are already sufficiently accurate and well-characterised to allow scientific analyses which are presented in an accompanying series of early papers. At this stage, HFI data appears to be of high quality and we expect that with further refinements of the data processing we should be able to achieve, or exceed, the science goals of the *Planck* project.

Key words. cosmology: observations – cosmic background radiation – methods: data analysis – surveys

1. Introduction

*Planck*¹ (Tauber et al. 2010; Planck Collaboration 2011a) is the third-generation space mission to measure the anisotropy of the cosmic microwave background (CMB). It observes the sky in nine frequency bands covering 30–857 GHz with high sensitivity

and angular resolution from 31' to 4.4'. The Low Frequency Instrument (LFI; Mandolesi et al. 2010; Bersanelli et al. 2010; Mennella et al. 2011) covers the 30, 44, and 70 GHz bands with amplifiers cooled to 20 K. The High Frequency Instrument (HFI; Lamarre et al. 2010; Planck HFI Core Team 2011a) covers the 100, 143, 217, 353, 545, and 857 GHz bands with bolometers cooled to 0.1 K.

Early science papers using HFI data are based on the products of the HFI data processing centre (DPC). This paper describes the steps taken to transform the packets sent by the satellite into frequency maps, with the help of ancillary data, for example, from ground calibration. At this early stage in the analysis, the LFI and HFI DPCs agreed to focus the analyses on temperature maps alone, as obtained from the beginning of the first light survey on the 13th August 2009, to the 7th June 2010. These nearly ten months of survey data provide complete coverage of the sky by all detectors (by roughly 3 days more than

[★] Corresponding author: F. R. Bouchet, e-mail: bouchet@iap.fr

^{**} This list includes those who contributed substantially over the years to the development of the HFI instrument, its operation and its data processing, as well as all the members of the *Planck* science team.

¹ *Planck* (<http://www.esa.int/Planck>) is a project of the European Space Agency (ESA) with instruments provided by two scientific consortia funded by ESA member states (in particular the lead countries France and Italy), with contributions from NASA (USA) and telescope reflectors provided by a collaboration between ESA and a scientific consortium led and funded by Denmark.

the minimum duration needed), but only limited redundancy. Indeed the overlap between the two consecutive six-month surveys is only about 60%.

The products of the early processing phase were made available to the joint HFI plus LFI DPC team in charge of producing the *Planck* Early Compact Source Catalogue (ERCSC), and also to the CMB removal team, on the 17th July 2010, i.e. only 5 weeks after the data acquisition was complete. Indeed, the early papers are based only on non-CMB products, so the DPCs produced a reference set of maps with the CMB removed. The CMB removed versions of the maps were made available to all of the *Planck* collaboration on the 2nd of August, i.e. three weeks later. The speed in completing this relatively complex chain of tasks was made possible thanks to the many years of preparation within the DPC, and to the excellent performance of the HFI in flight (described in the companion paper by the [Planck HFI Core Team 2011a](#)). Of course, the accuracy of the processing presented here is not yet at the level required for precision CMB cosmology, but as we shall see, it has already reached an accuracy that is sufficient for many early science projects.

The HFI DPC is the organisation in charge of analysing HFI data and ensuring strict traceability and reproducibility of the results. It is in charge of preparing all the formal deliverables of HFI at the six frequencies of the instrument. In addition to the concomitant *Planck* Catalogue of Compact Sources (PCCS), the deliverables include maps of the sky, and their error properties, for all the HFI channels for the nominal survey duration of 15.5 months. Early in the mission design, it was decided to have separate DPCs for each of the HFI and LFI to make efficient use of the hardware expertise, which is critical in generating science quality data from such complex instruments. Nevertheless, wherever possible common tools have been developed jointly by the two DPCs, for example, the non-instrument specific parts of the *Planck* simulation pipeline. We have also exchanged calibrated processed data between the two DPCs, every alternate month since the start of regular observations, to allow cross-checks between frequency bands and various other tests.

The HFI DPC relies on a centralised data base and common software infrastructures operating on a reference hardware platform. This centralized backbone serves geographically distributed groups of scientists in charge of various aspects of code development and of validating results. The infrastructure also serves dedicated science groups of the HFI Core Team. Parts of that infrastructure (and data) are replicated at various DPC supporting computer centres to avoid excessive data transfers. The combined computing power at these centres has proved important for some DPC activities, in particular for end-to-end Monte-Carlo simulations. Appendix A gives an overview of the infrastructure that we have developed. This infrastructure evolved from the initial implementation of a breadboard model (used as a prototype in designing the ground segment), a development model (completed in January 2007 to validate the basic infrastructures), and a flight model designed to be ready before launch² to process the data and create clean calibrated maps for the full duration of the nominal mission. Our main tasks after launch were therefore to compare the in-flight performance of the HFI to the data derived from ground calibration, to identify, understand and model unanticipated systematic effects, and to quantify uncertainties in the data as accurately as possible.

² This flight readiness was checked through end-to-end tests on simulated data, based on knowledge of the instrument derived from the ground calibration campaigns.

The next section provides an overview of HFI data processing. Section 3 describes the preliminary part of the processing which assembles telemetry packets in time-ordered information objects (TOIs). Section 4 is devoted to the processing of the detector TOIs to produce cleaned timelines which are used to estimate the temporal noise properties in Sect. 5 and to determine the beams and the focal plane geometry in Sect. 6. Section 7 discusses the creation of maps and their photometric calibration, and Sect. 8 describes the CMB removal. Section 9 concludes with a summary of the characteristics of the data, as currently processed.

Appendices A to E provides details on the DPC infrastructure, the temporal noise determination, focal plane measurements, the determination of the effective beams or band-pass measurements at CO lines frequencies.

2. HFI data processing overview

The overall data flow follows a succession of distinct steps which we refer to as “levels”. The first, L1, begins with formatting the data received from the satellite to build a database of raw data. The temporal sequences of measurements are grouped into objects generically called TOI. The second level of processing, L2, produces maps of the sky from the raw TOIs, their characterisation, and a model of the instrument. This is the core of the DPC analysis, when instrumental effects are identified and corrected. The next level, L3, involves separating the sky emission maps into astrophysical components (including point sources) and their scientific characterization.

Functionally, the data analysis may be thought of as using data, y , related to an unknown source, x , through some function, F , describing the measurement process, to infer information on x from y . In addition, we need to estimate at least the covariance matrix of the errors on the estimate of x . Different choices of x and y describe different steps of the data analysis. For L2, the unknown x is the sky emission in different bands. The function F is then a description of how the instrument relates the sky to the data, where y is the TOI and associated calibration data. The difficulty is, of course, that F must be partly determined (or at least verified) from the flight data itself, which requires an iterative procedure involving a succession of analysis and synthesis steps.

In the analysis phase, a parametric model is constructed of the relationship linking the TOIs to the unknowns, together with estimates of the current values of the parameters. In the synthesis phase, this model of the measurements is used in conjunction with the TOIs to process the TOIs globally and to determine the unknowns. The results may then be used to improve the parametric model of the measurement to be used at the next iteration (e.g., by sampling the resulting sky map to obtain an improved signal predictor to be removed from the raw TOIs) for noise estimation. In practice, most of the L2 tasks are devoted to improving the instrument model (instrument temporal transfer function, noise properties, focal plane geometry, main beams, far side lobes, gains, identification of systematic effects, etc.).

Each new pass through the data results in new processed data and an improved understanding of the measurements. This understanding is retained through an update of the instrument model which therefore has a central (conceptual and practical) role. The instrument model (IMO) is a synthesis of the information (from ground test and flight data, simulations and theoretical considerations) required to perform the data processing. Implementation details may be found in the Appendix A.3. The

initial version of the *IMO* was derived pre-launch from an analysis of ground calibration data and was used for processing the First Light Survey, i.e. data acquired during the last two weeks of August 2009. The analysis of the First Light Survey verified that the satellite, instruments and their ground segments were all fully operational. The next *IMO* version included improved models derived from a detailed analysis of the calibration and performance verification phase (CPV) data acquired during the previous 1.5 months. Further versions of the *IMO*, and of the pipelines themselves were then derived after the completion of successive passes through the data. The data made available to the *Planck* consortium for the early science papers resulted from the fourth pass through the data.

We now provide an overview of the main steps involved in the data processing, which can be visualised with the help of Fig. 1. First, the L1 software fills the database and updates, daily, the various TOI objects as described in Sect. 3. The satellite attitude data, which we receive sampled at 8 Hz during science data acquisition and at 4 Hz otherwise, are densely sampled by interpolation to the 180.4 Hz acquisition frequency of the detectors. Raw TOIs and housekeeping data are then processed to compensate for the instrumental response and to remove estimates of known artefacts. To do so, the raw TOIs in Volts, are demodulated, filtered, deglitched, corrected for gain non-linearity on strong sources like Jupiter, and for temperature fluctuations of the environment using correlations with the signal TOIs from the two dark bolometers. Narrow spectral lines caused by the 4 K cooler are also removed before decorrelating the temporal response of the instrument. Finally, various flags are set to mark unusable samples, or samples where the signal from planets or other strong sources is important. The setting of flags is described further in Sect. 4.

The *Planck* satellite spins around an axis pointing towards a fixed direction on the sky, repeatedly scanning the same circle till it is repointed towards a new fixed direction. As the spin axis follows the Sun, the observed circle sweeps through the sky at a rate of ≈ 1 degree/day. Assuming a focal plane geometry, i.e. a set of relations between the satellite pointing and that of each of the detectors, one can proceed to build “rings” which are used to derive a new version of the *IMO*. A ring corresponds to a sky signal estimate along a circle which can be derived by analysing all the data acquired by a detector during each stable pointing period, when the spin axis is pointing towards an essentially fixed direction in the sky and the detectors repeatedly scan the same circle on the sky (up to a negligible wobbling of the spin axis). This redundancy permits averaging of the data on rings to reduce the instrument noise. The resulting estimate of the sky signal can then be removed from the TOI (by unrolling it periodically) to estimate the temporal noise power spectral density, which is a useful characterisation of the detector data after TOI processing. As described in Sect. 5, this noise may be described as a white noise component, dominating at intermediate temporal frequencies, plus additional low and high frequency noise (when passed by our high frequency filtering).

The effect on maps of the low frequency part of the noise can be partially mitigated by determining an offset for each ring. These so-called “destriping” offsets are obtained by requiring that the difference between intersecting rings be minimised. Once the offsets are removed from each ring, the rings can be simply co-added to produce sky maps. As explained in the map-making and calibration section (Sect. 7), a complication arises from the fact that the detector data include both the contribution from the *Solar* dipole induced by the motion of the Solar System through the CMB (sometimes referred to as

the “cosmological” dipole), and the *orbital* dipole induced by the motion of the satellite within the Solar System. The orbital dipole contribution must, of course, be removed from the rings before creating the sky map. While the orbital dipole can in principle be used as an absolute calibrator for the CMB detectors, it is rather weak and needs a long baseline to break degeneracies with other signals. For the time being, we use the Solar dipole as determined by WMAP, or a comparison with COBE/FIRAS at higher frequencies, as our calibrators at the map level. Since we need this calibration to remove the orbital dipole contribution to create the maps themselves, the maps and their calibrations are obtained iteratively. The dipoles are computed in the non-relativistic approximation. The resulting calibration coefficients are also stored in the *IMO*, which can then be used, for instance, to express noise spectra in noise equivalent temperatures (NETs).

The “destriping” offsets, once obtained through a global solution, are also used to create local maps around planets which, as described in Sect. 6 can be used to improve knowledge of the focal plane geometry stored in the previous version of the *IMO* and to improve measurements of the “scanning” beam (defined as the beam measured from the response to a point source of the full optical and electronic system, *after* the filtering done during the TOI processing step).

The ring and map-making stages allow us to generate many different maps, e.g., using disjoint sets of detectors, the first or second halves of the data in each ring, or from different sky surveys (defined, by convention, as the data acquired over exactly six months). The creation of “jackknife” maps, in particular, has proved extremely useful in characterising the map residuals.

Section 8 describes a further step, performed jointly with the LFI DPC, to estimate and remove the CMB contribution over the full sky in all of the channel maps. This was used by some of the scientific analyses reported in the *Planck* early release papers (though other analyses used specific CMB removal techniques, described in the relevant papers, e.g. using ancillary data available in their specific areas of the sky). The specific processing for extracting the *Planck* ERCSC from the HFI and LFI maps is described in a companion paper (Planck Collaboration 2011c) and additional details can be found in the ERCSC explanatory supplement (Planck Collaboration 2011v).

The properties of the data are summarised in the concluding Sect. 9.

As already stated, this paper does not address polarisation measurements from the polarisation sensitive bolometers (PSBs) on the HFI at the 100, 143, 217 and 353 GHz channels. The accuracy of their properties derived from ground calibration is sufficient for our current purposes, which is limited to using PSBs as contributors to the total intensity measurements. Ground measurements showed that the polariser orientations are within about 1 degree of their nominal values. Similarly, ground measurements showed levels of cross-polarization leakage of a few percent, which is good enough to use PSB TOIs to create the temperature maps discussed in this paper. Additionally, we have verified for Tau A, a bright polarised calibration source with a $S/N > 400$ in a single (unpolarised) detector scan, that in-flight determinations are consistent with pre-launch data.

3. From packets to time-ordered information

L1 is a collection of hardware and software items used to retrieve and gather data from the satellite and the ground segment. Functionally, L1 has two objectives. The first is to provide the instrument operation team with the tools required to monitor

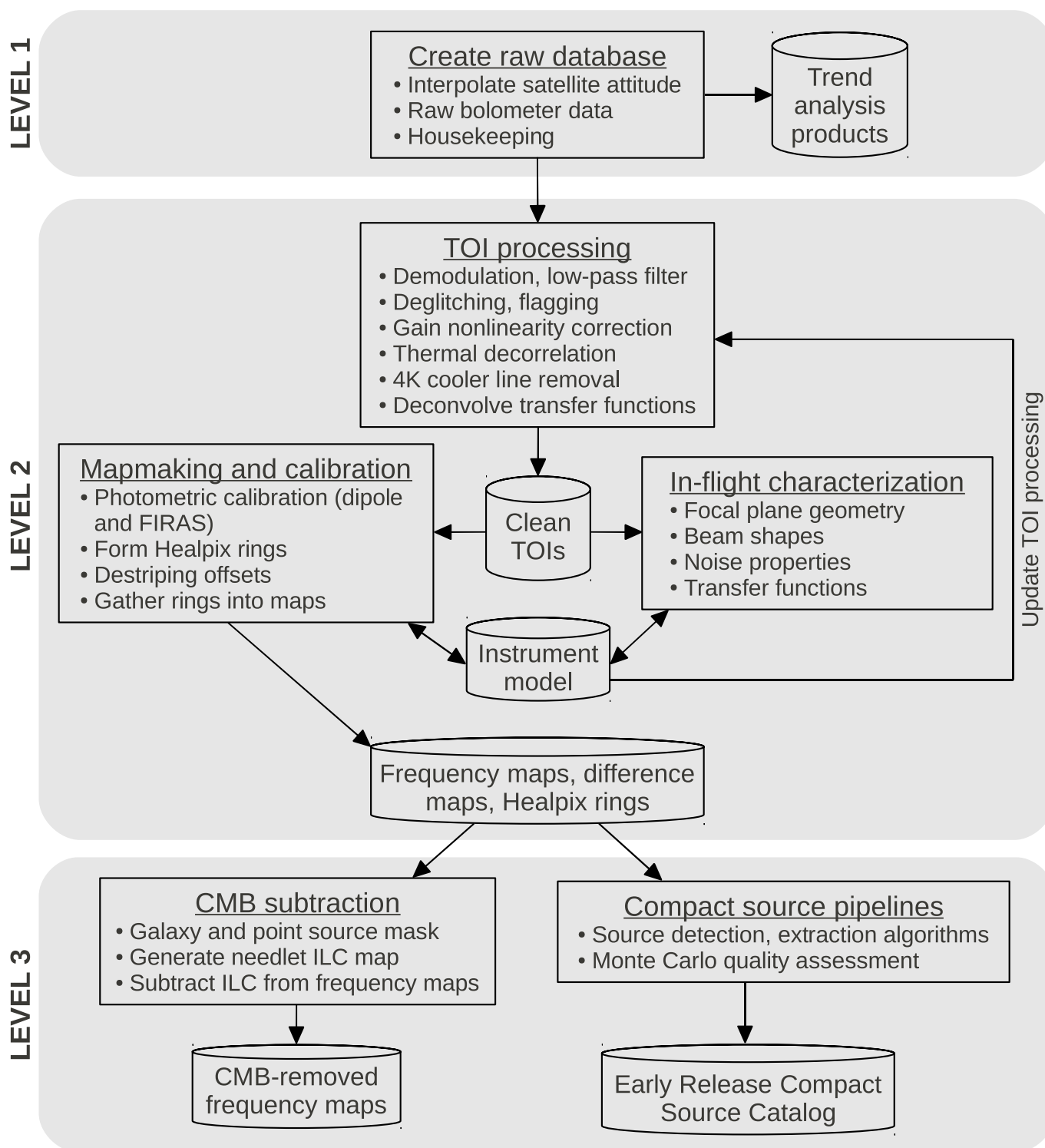


Fig. 1. Overview of the data flow and main functional tasks of the DPC. This flow diagram illustrates the crucial role of the Instrument Model (IM) which is both an input and an output of many tasks, and is updated iteratively during successive passes of the data.

the HFI instrument with a typical response time of a few seconds. Those tools are the SCOS³ visualisation tool and the HFI Quick Look Analysis (QLA) tool which enables the visualisation of lower level parameters, as well as command checking and acknowledgement. The Trend Analysis (TA) tool provides quasi-automated reports on the evolution of various instrument

parameters. The second L1 objective is to build TOI and ingest them into the DPC database for the next level of data processing.

The data set handled by the L1 consists of:

- the telemetry packets which are, either coming from the satellite in near real time during the daily telecommunication period (DTCP), or dumped daily from the satellite, consolidated and made available by ESA's Mission Operating Centre (the MOC);

³ SCOS-2000 is the generic mission control system software of ESA.

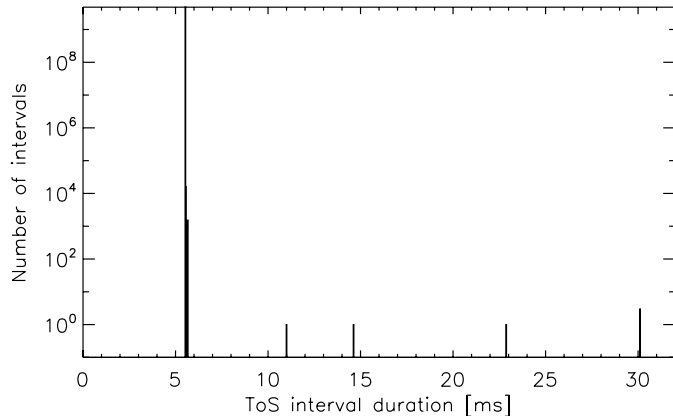


Fig. 2. Histogram of time differences between two successive samples. The time quantization step is $15\ \mu\text{s}$.

- auxiliary files such as pointing lists, orbit files, attitude data, on-board-time and universal time (OBT-UTC) time correlation data, telecommands history file as built by the MOC.

Regarding the data received from the satellite, L1 handles the satellite, sorption cooler and the HFI housekeeping data and the HFI “scientific” data, each with its own sampling rate. HFI housekeeping data include the 7 setup parameters for each detector (bias, voltage, gains, compression) and the HFI general configuration (thermometry, temperature control, power supply, state of coolers). From the housekeeping telemetry packets the parameters are extracted and stored in the data base.

Signals in a telemetry packet or house keeping parameters, usually come in ADU (analogue-to-digital unit). They are stored in the form in which they are received and often need to be combined in various ways and converted to appropriate physical units, which is done on-the-fly using a dedicated library (cf. Appendix A.4 describing the so-called transfer functions).

3.1. Building the HFI science TOIs

On board, the signal from the 72 HFI channels is sampled at $180.4\ \text{Hz}$ by the Read-out Electronic Unit (REU). 254 samples per channel are grouped into a *compression slice*. The Data Processing Unit (DPU) then builds a set of several telemetry packets containing the compression slice data and adds to the first packet the start time of the compression slice. When receiving this set of telemetry packets, the L1 software extracts the 72×254 samples and computes the time of each sample based on the compression slice start time (digitized with $15\ \mu\text{s}$ quantization steps) and a *mean sample time* between samples. For the nominal instrument configuration, the sample integration time is measured to be $T_{\text{samp}} = 5.54404\ \text{ms}$. At one rotation per minute, this corresponds to an arc of $2.0\ \text{arcmin}$ on the sky. This interval is quantized in units of $2^{-16}\ \text{s} = 15.26\ \mu\text{s}$, so that occasionally the time intervals differ by that amount, as can be seen from Fig. 2.

It should be noted that the time of sample (ToS) depends on the REU sampling time and the DPU clock. Although the REU sampling time was fixed once at the beginning of the mission by telecommand, it relies on the REU clock quartz frequency which depends slightly on its temperature. From the satellite Thermal Balance/Thermal Vacuum tests in Liège, this dependency has been computed to be about $7.1\ \text{ns}$ for a change of the REU temperature by one Kelvin. Given the observed temperature stability of the REU (a drift by less than $0.6\ \text{K}$ for the mission duration

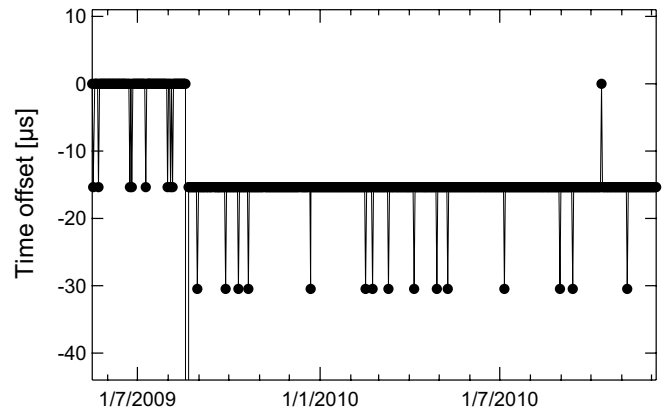


Fig. 3. Time offsets showing that the HFI DPU clock is in synchronisation with the satellite on-board time within a $15\ \mu\text{s}$ quantization step.

so far), this correction does not currently need to be taken into account in the ToS computation.

The ToS also depends on the DPU clock through the compression slice time stamping. Figure 3 shows that the DPU clock remains synchronised, within a $15\ \mu\text{s}$ quantization step, with the satellite clock, with the largest exception so far being the large step which can be seen on the plot around the end of August 2009. This was caused by a software patch of the satellite Command and Data Management Unit. This local desynchronization is small enough that it is ignored in the computation of the ToS for this analysis.

3.2. Statistics about the data gathered by L1

During the first year of survey (which excludes the commissioning and CPV phase, when the HFI was in specific modes of data production) the L1 handled 4.0×10^8 telemetry packets; 29% for satellite housekeeping; 6% for spacecraft housekeeping; 4% for HFI housekeeping; and 61% for HFI science data. The total number of housekeeping parameters stored in the database is 25 425.

Regarding HFI science packets, only 20 packets (i.e. $8.1 \times 10^{-6}\%$) have been lost at the satellite level for well understood technical reasons. None has been lost during transmission from space to the ground nor at the ground segment level.

A total number of 4.66×10^9 time samples have been stored in the database for each of the 72 detectors, leading to a total of 3.36×10^{11} science data samples.

3.3. Numerical compression of science data

The quantization performed during the compression process was tuned during the CPV and the early phase of the survey. The compression performance complies with the requirements and is detailed in Lamarre et al. (2010).

Because of the finite telemetry bandpass between the spacecraft and the ground station, the signal cannot be transmitted in some rare circumstances, specifically, large amplitude glitches (which, in any case, are flagged out during the deglitching process) and the Galactic centre region for the 857 GHz detectors (where less than 200 samples were lost during the March 2010 crossing). Because of the redundancies inherent in the *Planck* scanning pattern, and the irregular angular distribution of the small number of compression errors, no pixels are missing in the maps of the Galactic centre regions.

3.4. Pointing processing

As is described in the mission overview paper (Planck Collaboration 2011a), the DPCs retrieve the reconstructed pointing information of the satellite every day from ESA's Mission Operating Centre.

The main data consists of the attitude as a function of time, represented by a normalized quaternion. The attitude is the rotation linking a fixed reference frame on the satellite, in this case that formed by the telescope nominal line-of-sight and the nominal spin axis, with a sky reference frame in ecliptic J2000 coordinates. Both the raw attitude data (i.e. as provided by the on-board satellite pointing system) and a processed version of this data, are distributed to the DPCs. The main processing consists of filtering high frequency noise during the stable pointing periods (i.e. between slews). The order of magnitude of this high frequency noise can be roughly evaluated by measuring the mean quaternion distance $\Omega = \arccos(q_r q_f^{-1})$ between the raw quaternion q_r and the filtered one q_f (see below), which is of the order of 7 arcsec.

Other ancillary data are also retrieved which are either related to the performance of the pointing system (operating mode, quality of the attitude determination, time of firing of the thrusters) or are derived quantities (in particular the nutation, mean and instantaneous direction of the spin axis).

This data is retrieved by L1 in the form of two files: the Raw Attitude File (RAF) and the Attitude History File (AHF) which contains the raw and ground processed daily pointing information. Both are stored in the HFI database, and their content is used to compute the pointing at each data sample for each bolometer.

At this stage of the mission, we assume that the pointing reconstruction, once processed, is perfect and thus the computation of the pointing at each data sample is very simple. The filtered attitude is interpolated to the time of sampling of the bolometers using the spherical linear interpolation algorithm (Shoemake 1985), i.e. the attitude quaternion $q(t)$ at time $t_0 < t < t_1$ is computed from the AHF quaternions, $q_0 = q(t_0)$ and $q_1 = q(t_1)$, from a linear interpolation on the sphere which is given by $q(t) = (q_1 q_0^{-1})^{\Delta t} q_0$, where $\Delta t = (t - t_0)/(t_1 - t_0)$. This formula can be rewritten as

$$q(t) = \frac{\sin(\Omega(1 - \Delta t))}{\sin \Omega} q_0 + \frac{\sin(\Omega \Delta t)}{\sin \Omega} q_1, \quad (1)$$

with Ω the quaternion distance between q_0 and q_1 defined above.

The interpolation is done once (since all bolometers are sampled at the same time) and then submitted to the database. This has a cost in disk space but, in the future, may be used to correct for possible time dependent deformations of either the star tracker assembly or telescope assembly. No such correction has been applied at this stage, given the low level of deformation which has been measured so far (see Sect. 6).

The pointing for each bolometer is computed on the fly⁴ by combining the attitude with the location of the bolometer in the focal plane, as computed by the focal plane geometry pipeline (see Sect. 6) and stored in the mo. This means that a single pointing timeline is kept in the database, rather than one per bolometer, producing substantial savings of disk space (a pointing timeline requires eight times the storage space of a signal timeline:

⁴ This is done using the HFI pointing library, which can compute the pointing in different sky reference frames, using different pointing representations (Cartesian, spherical) and polarisation angle conventions (IAU or HEALPix).

four double precision values for the quaternions compared to one single precision value for the data).

The AHF and RAF are also used to obtain the reference times used to segment the data streams into rings (or pointing periods) which correspond to the intervals between successive depointing manoeuvres. These rings are used both as an aid to index data and as a basis for some of the data processing tasks⁵.

Finally a set of flags is created to identify the part of each ring that corresponds to the stable pointing period. Only this part of the data is currently used in further processing.

4. TOI processing

The TOI processing pipeline produces cleaned TOIs and associated flags for use in the subsequent data processing. The basic steps involved are: (1) signal demodulation and filtering; (2) deglitching, which flags the strongest part of the glitches and subtracts a model of their tails; (3) conversion from instrumental units (Volts) to physical units (Watts of absorbed power), including a correction for non-linearity; (4) decorrelation of thermal fluctuations; (5) removal of the systematic effects induced by the 4 K cooler mechanical vibrations; (6) deconvolution of the bolometer time constant. These steps are described in more detail in the remainder of this section.

4.1. Demodulation and initial filtering

The data are first demodulated from the AC bolometer modulation. A low-pass filter is then applied to the TOI in order to remove the modulation frequency carrier (at 90.19 Hz). This low-pass filter (a finite width digital symmetrical filter) is adapted to the temporal transfer function (see Sect. 4.6) using data from Mars crossings. Hence, the demodulated data $d(t_i)$ is filtered with a centred filter f_j of width $2N + 1$:

$$\text{TOI}_i = \sum_{j=-N}^{+N} d(t_{i+j}) f_j.$$

The optimization criteria to derive the filter coefficients include (1) to have an exact zero at the modulation frequency; (2) to minimize beam smearing in the in-scan direction (less than 20% increase of the in-scan beam width); and (3) to reduce the enhancement of high-frequency noise after the temporal transfer function deconvolution. It was found that a Kaiser-like filter (Kaiser 1974; Walraven 1984) with 13 points offers a good trade-off for the 100 and 143 GHz, while we use a 21-point filter for the 217 and 353 GHz, and a 3-point filter for the 545 and 857 GHz channels (this last filter is simply $\{\frac{1}{4}, \frac{1}{2}, \frac{1}{4}\}$).

Figure 4 displays the signal for three typical bolometers after demodulation. At 143 GHz, one clearly sees the CMB dipole pattern with a 60 s period. Both the 143 and 545 GHz bolometers clearly show the two Galactic plane crossings, also with a 60 s periodicity. The dark bolometer exhibits a rather constant baseline, as well as a population of glitches similar to those apparent in the 143 and 545 GHz detectors.

4.2. Glitch handling

Glitches result from the impact of cosmic rays in the vicinity of HFI detectors. As can be seen in Fig. 4, they are quite conspicuous in the raw data. We start by describing the glitch types we

⁵ The start and end time of rings are the actual times of thruster firings.

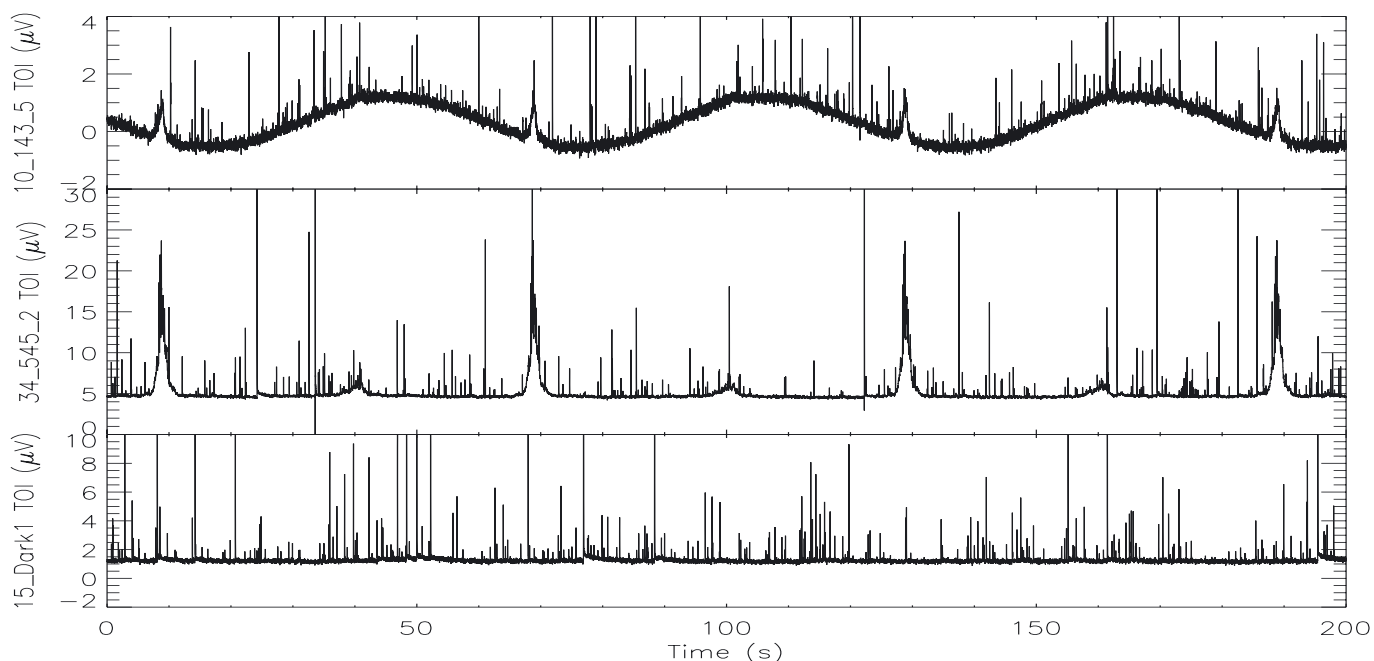


Fig. 4. Raw TOIs for three bolometers, the “143-5” (*top*), “545-2” (*middle*), and “Dark1” (*bottom*) illustrating the typical behaviour of a detector at 143 GHz, 545 GHz, and a blind detector over the course of three rotations of the spacecraft at 1 rpm. At 143 GHz, one clearly sees the CMB dipole with a 60 s period. The 143 and 545 GHz bolometers show vividly the two Galactic Plane crossings, also with 60 s periodicity. The dark bolometer exhibits a nearly constant baseline together with a population of glitches from cosmic rays similar to those seen in the *two upper panels*.

found in the data (see [Planck HFI Core Team 2011a](#), for a discussion of their physical origin), then we describe the method that we have developed to process them, and then we show how this processing modifies the data. Finally we address the question of errors in the data introduced by the deglitching process.

4.2.1. “Glitchology”

The shape of a typical glitch is characterised by a sharp rise followed by a slow decay. The occurrence of glitches are not correlated with each other (except between detectors belonging to the same PSB pair) and they are independent of the sky signal. This first finding was quantified by measuring the histogram of the time delay between two glitches and showing that it follows the expected exponential law for uncorrelated events. Nevertheless, we were not able to check this behaviour accurately below 20 sample intervals (≈ 100 ms) because of confusion between events. The “noise” in the data produced by glitches is naturally dealt with in the time domain, as its source is well localized in time. Three significant populations of glitches have been identified and characterized: *short glitches*, which are characterised by a fast decay (of a few milliseconds) followed by a low amplitude slower decay; *long glitches*, whose fast decay is followed by a long tail with time constants of about 60 ms and 2 s; even *longer glitches*, which show only a slow decay very similar to the second category. Figure 5 shows examples of these three glitch types. The population of long glitches predominates at low and intermediate amplitudes whereas the short glitches dominate at higher amplitudes (see Fig. 12 for a quantitative assessment).

Precise templates have been obtained for each glitch population in each bolometer by stacking many events (see [Planck HFI Core Team 2011a](#), for more details). Figure 6 summarizes the properties of the long glitch templates for all the 143 GHz detectors; each template is a sum of four exponentials, and the figure

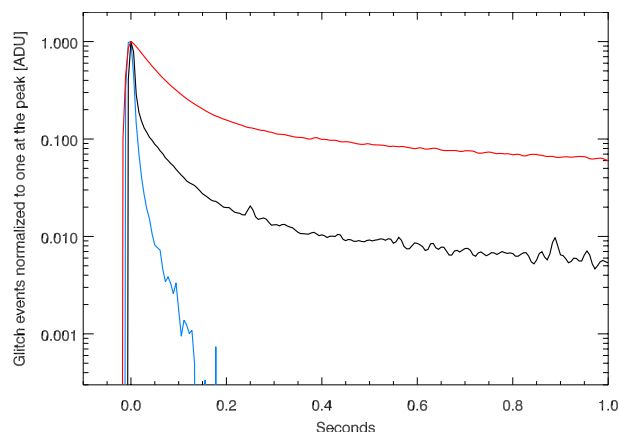


Fig. 5. Three examples of high amplitude glitch events for one bolometer. One event for each category of glitch is shown, normalized to unity at the peak. The blue curve shows a short glitch, the black curve a long one, and the red curve is for a very long glitch. Short and long glitches both display a fast bolometer time-constant decay; in the case of long glitches this is followed by an extended tail. Very long glitches are described by the same extended template as long glitches but do not show the fast bolometer time-constant decay.

displays, for each exponential, its amplitude and decay time. Note the long duration (~ 0.5 – 5 s) of the low-amplitude components. By comparing the long glitch templates for different bolometers, we observe that for PSB-a detectors long glitches have a 60 ms exponential decay with an amplitude relative to the peak of about 10%, whereas for PSB-b and SWB detectors this intermediate time-constant decay is at a substantially lower amplitude. The long time constant decay of long glitches of about two seconds produces noise excess at frequencies approximately 0.01 Hz, which is well above instrumental and photon noise for most of the detectors. The shape of the long glitch

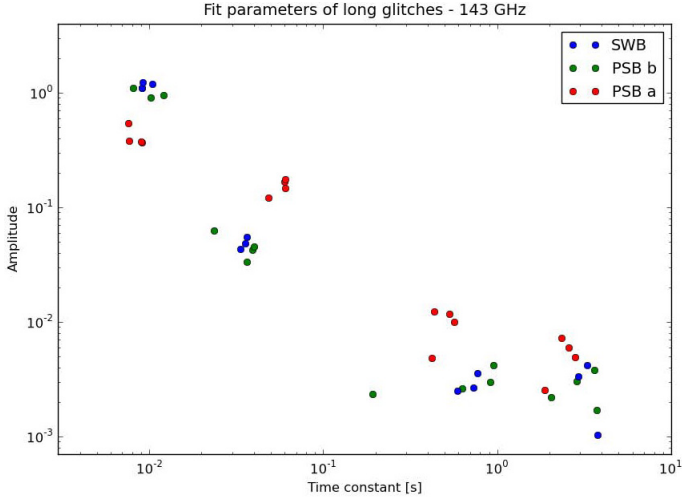


Fig. 6. Amplitudes of the components of the long glitch templates versus their exponential decay times. For each bolometer (here those at 143 GHz), the glitch template is fitted as a sum of four exponentials, $\sum_{i=1}^4 A_i \exp -t/\tau_i$ (and the plot shows A_i vs. τ_i). We observe some homogeneity in the grouping of the long glitch characteristics of the detectors, even more so within each detector type.

decay does not vary significantly over the time of the mission or as a function of amplitude.

Given a glitch rate of typically one per second, and their long decay times, we cannot simply flag them out, since that would lead to an unacceptably large loss of data. We therefore flag (and in practice discard) only the initial part of the glitch and fit the tail with a model which is subtracted from the TOI. The temporal redundancy of the sky observations is used to separate the glitch signal from the sky signal. Since each ring is scanned 40–70 times with excellent pointing accuracy (see the paper by [Planck Collaboration 2011a](#)) the *Planck* scanning pattern provides a high degree of redundancy. This redundancy is of crucial importance as it provides a way to separate from strong signals, such as point-sources, which will generally show similar temporal behaviour to the glitches. The algorithm used for the glitch processing iterates between the estimates of the signals from the sky and from the glitches, and hence should not bias the estimation of the final sky signal since, at convergence, the glitch detection is to first order independent of real sky signals.

Many previous bolometric CMB experiments have deconvolved the time streams prior to deglitching, which has the benefit of increasing the signal-to-noise on glitches and minimizing the fraction of flagged data. For a very good reason, this is not what is done in HFI; the populations of glitches each exhibit distinct transfer functions, so there is no single Fourier representation that would appropriately treat them all.

4.2.2. Glitch handling methodology

An initial estimate of the sky signal is obtained ring-by-ring by using only data within three times the dispersion around the median value in each sky phase bin (ring pixel) in order to mitigate the effect of possible outliers. A third-order polynomial interpolation within ring pixels is then performed to account for sub-pixel variations of the signal (e.g., large gradients close to the Galactic plane). This is used to subtract the estimated sky signal from the TOI at the exact time/position of the sample. The glitch detection threshold is first set relatively high to prevent errors in the reconstructed signal from inducing spurious detections.

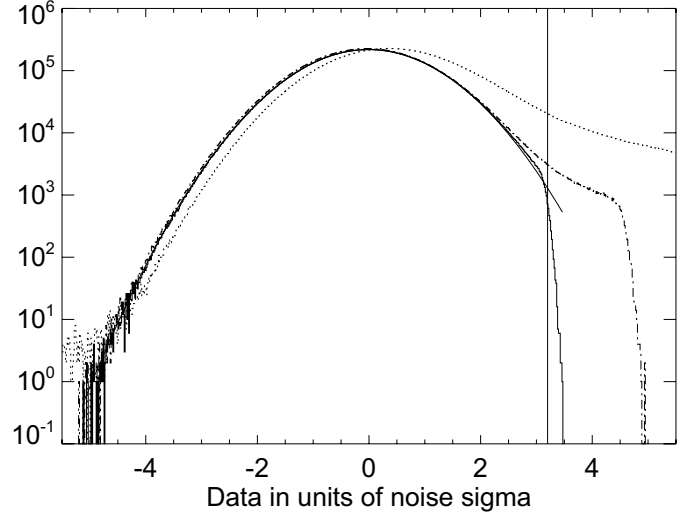


Fig. 7. The solid curve is the histogram of a series of bolometer values after deglitching with a 3.2σ threshold, subtracting estimates of the sky signal and glitch templates, as well as high pass filtering. A fit with a Gaussian is also shown. We do not see a sharp cut at 3.2σ because of the low pass filter applied to display the data. The dot-dashed curve is the same as before but after deglitching with a 4.5σ threshold. The dotted curve is for data without deglitching. A 3.2σ threshold offers a good trade-off between data losses and remaining contaminants.

Then the threshold is decreased by a constant ratio at each iteration as the estimate of sky signal and glitches improves. Usually some five iterations are needed for convergence. After the first iteration, the sky signal is re-estimated using a more elaborate method described later.

The final detection threshold of glitches is set to 3.2σ , where σ is the local noise level. This choice is a trade-off between the amount of data flagged and the number of small glitches left in data, as shown in Fig. 7. Reconstructed distributions of cosmic rays appear to show a break at lower amplitudes indicating that only a small fraction of the small glitches remain in the data.

Events with an amplitude larger than 3.2σ are detected in small data windows by finding their maxima after 3-point filtering of data. Very confused events are not distinctly detected using only maxima, but many are detected by applying a matched filter tuned to detect abrupt changes of slope. Data flagging and cleaning is performed progressively window by window. Each window is set with the maximum event of the interval at the center, provided it has not yet been flagged from the processing of other windows. Within a window, a multi-parameter fit of the amplitudes of long templates is performed jointly for all events which are eight samples after the maxima. This is done in practice by minimizing:

$$\chi^2 = \sum_{t=0}^{N_s} (d_k(t) - \sum_i a_i T_l(t - t_i) + K)^2 M(t), \quad (2)$$

with respect to the amplitude parameters a_i for all the events i in the window as well as an offset K , where N_s ($=1000$ in practice) is the number of sample per window, $d_k(t)$ is the signal-removed data value at sample t and iteration k , $T_l(t - t_i)$ is the normalized long glitch template at $t - t_i$ samples after the maximum located at t_i , and $M(t)$ is a mask function (which is zero within eight samples after the glitch maxima and also where data have been flagged at a previous iteration, and unity otherwise). All of the amplitude parameters are constrained to be positive. Joint fitting

is critical at this stage because of the high level of confusion between events. Low frequency drifts of noise are well represented by constants in intervals within windows (K in the expression above) and are fitted jointly with the glitch templates.

If events in the centre of the window have maxima above 10σ , and the fitted long templates are above 0.5 times the amplitude expected for long glitches, then the template is subtracted from the data using the fitted amplitude as follows:

$$d_{k+1}(t) = d_k(t) - \sum_j \hat{a}_j T_l(t - t_j), \quad (3)$$

where $d_{k+1}(t)$ is the cleaned data used for the next window at time t , \hat{a}_j the estimated template amplitude for event j such that all t_j are separated by less than eight samples starting from the event at the centre of the window. Samples around glitch maxima are flagged in intervals defined such that the expected remaining glitch signal in its tail is well below the noise rms. For glitches below 10σ , or for detected short glitches, nothing is subtracted from the data and the glitch is entirely flagged. The window is then moved to other events which have not yet been cleaned. In total, between 9 to 16% of the data are flagged, depending on the rate of glitches (see Fig. 11 below).

Once the templates have been removed window-by-window and the data flagged, a matched filter built from the long glitch template is applied to data. Rare events detected by the matched filter are flagged in long intervals. Up to 2% of the data are flagged in this way for bolometers with the highest rate of glitches.

At the end of this procedure, the sky signal is re-estimated after removing the glitch templates from the original data, using unflagged data only, and a new iteration of the whole detection procedure is performed. In contrast with the first iteration, we use for all ensuing ones a more elaborate method for this sky estimate. We fit splines with nodes at the location of ring pixels. This has proven to be very efficient at capturing sky variations within ring pixels. Simulations show that errors of less than 0.1% are made in the signal reconstruction of a Gaussian with a FWHM of three times the ring pixel size (close to the characteristic size of a point source in *Planck* data). Errors in the signal reconstruction by this method are dominated by the effect of small pointing drifts, which are of order 10 arcsec within a ring; this is significant only for the higher frequency channels at Galactic plane crossings or for exceptionally strong sources. We have increased the glitch detection threshold to account for signal reconstruction errors by adding quadratically a term in the noise rms proportional to the signal amplitude in each pixel. This correction is negligible for all the data except for planet transits in CMB channels (100, 143, 217 GHz) and is significant only within the Galactic plane and when scanning strong sources at higher frequencies.

We obtain convergence between signal and glitch template estimates for 99.99% of the rings. Nevertheless, the very few rings for which convergence is not reached can be detected by checking when glitch tail templates are subtracted systematically at exactly the same location in the sky for consecutive scan. These rings are discarded from the analysis.

4.2.3. Glitch handling results

Figure 8 shows examples of the deglitching process on the sky-subtracted data. The glitches in this segment are overlapping, a situation which arises quite often. Globally, glitch template correction is very effective, despite the fact that the glitch rate varies

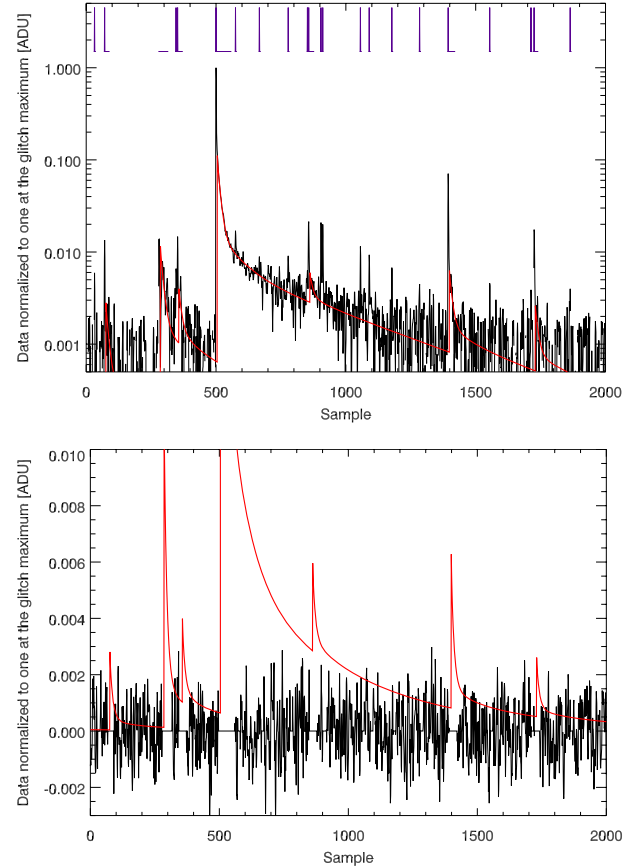


Fig. 8. *Top panel:* example of 2000 samples of sky subtracted data encompassing a large event in black and our best fit glitch templates (red). The purple ticks in the upper part of the figure show where data are flagged and indicate the detected position of glitches. *Bottom panel:* the cleaned residual in black (with the flagged areas set to zero) compared with the fitted template in red.

appreciably from bolometer to bolometer. Figure 9 compares the power spectra of noise in TOIs for all bolometers at 143 GHz (except 143-8, which is affected by random telegraphic signal (RTS) noise, see Sect. 4.7), with and without long glitch template subtraction. Flags have been applied in both cases (flagged samples have been masked and filled using a simple interpolation method). For this plot, the flags applied to estimate the noise power spectra without template subtraction are extended to mask the data for which the long glitch template is above one sigma of the noise. This has a non-negligible extra cost (up to 9% of the data for some bolometers) in the amount of data masked. We can see that the template correction reduces the spurious noise power by a factor of around 4 for a large fraction of the bolometers at frequencies in the range 0.02 Hz to 2 Hz, whilst simultaneously reducing the amount of data flagged for exclusion in the map-making stage. Nevertheless some low level residual is still expected in the data after template subtraction. We have performed simulations to assess the level of these residuals, see Sect. 4.2.4.

To evaluate the effects of glitch removal on the final maps, we have projected the correction TOI (the sum of the estimated glitch templates) into maps and computed the corresponding power spectra. Note that these correction time-line are generally non-zero nearly everywhere i.e. all samples are corrected by this “baseline removal”. A map and associated power spectrum are shown in Fig. 10 for one bolometer at 353 GHz. There is no obvious correlation of the glitch template estimation with the

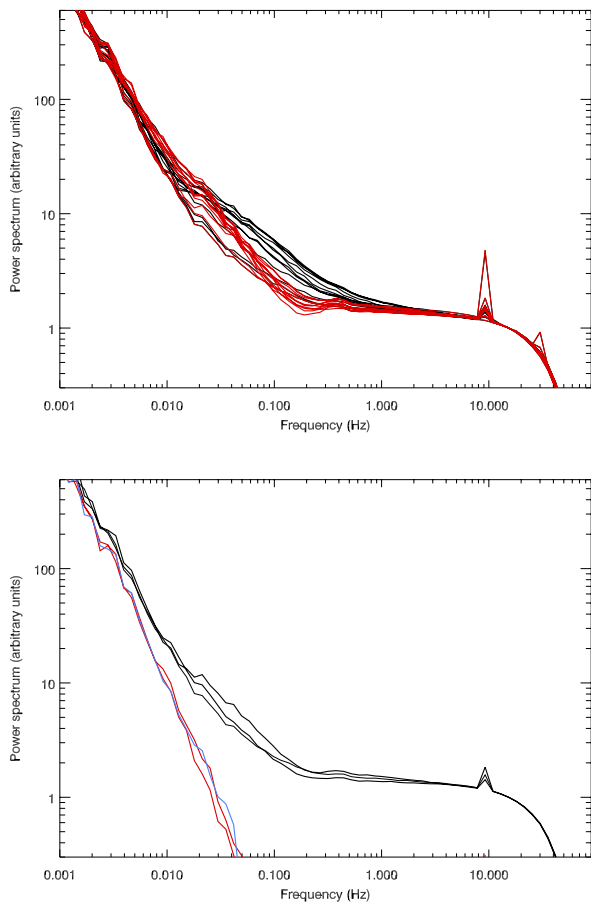


Fig. 9. **a) top:** power spectra of the noise in the TOIs for all bolometers at 143 GHz without (black) and with (red) subtraction of long glitch templates. The data corresponds to sky-subtracted TOIs, before any further processing; one can see, for instance, 4 K lines harmonics at 10 and 30 Hz which have not been removed at this stage (this is done later in the TOI processing pipeline). Two of the 143 GHz detectors have a rate of long glitches about a factor of five below that seen in those with the highest glitch rate. The power spectra for these two bolometers are those with the lowest amplitude at around 0.03 Hz; as can be seen from the figure, the template correction in these two cases has only a very small impact. As a result, these bolometers can be used to test for noise from sources other than glitches. This plot illustrates the efficiency of the template subtraction method in reducing contaminant noise in the frequency range 0.02 Hz to 2 Hz whilst simultaneously reducing the amount of flagged data. **b) bottom:** the auto-spectra after deglitching of 3 of the 143 GHz bolometers of the top panel, in black, are compared with their cross-spectra in blue and red. The blue curve corresponds to the cross-spectra of two bolometers in a PSB pair. This suggests that the decorrelation from common mode thermal fluctuations cannot have much of an effect on the noise at frequencies greater than the spin frequency at 0.02 Hz.

Galactic signal at that frequency, but we have noted some anti-correlation at 857 GHz, when the Galactic signal is strongest. This is expected since the glitch detection threshold is significantly increased for the highest frequencies in presence of strong signal. The power spectrum of the glitch template map is roughly proportional to $1/\ell$, as expected (Efstathiou 2007; Tristram et al. 2011). Conversely, we checked whether any CMB has leaked into the glitch time-stream, $g = g_0 + \alpha \text{CMB}$, by finding limits on α through cross-correlating our glitch maps with the 7 years WMAP ILC map. We then estimate α as the ratio of the cross-spectra (glitch X ILC)/(ILC X ILC) for $\ell < 300$; we found no

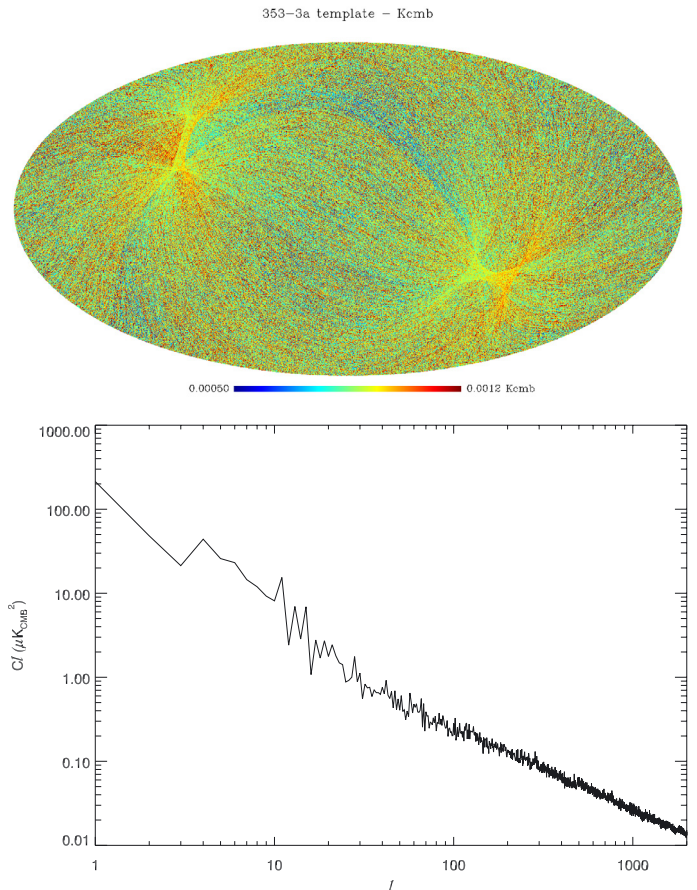


Fig. 10. **Top:** map in Galactic coordinates built by projecting the estimated long glitch template for one bolometer at 353 GHz. Comparison with the Jackknife map at the same frequency in Fig. 34 shows that, if uncorrected, that contribution would be the dominant part of the residual “noise”. **Bottom:** power spectrum of the map shown in the top panel.

evidence for leakage of the CMB into the 100, 143, and 217 GHz glitch time-streams. Indeed this leakage was constrained to be smaller than 0.01%.

We have also tested whether significant glitch residuals are left in the data near the event peaks after template subtraction, by multiplying the flag extents after each glitch peak by a factor of two. We applied this for all detectors at 143 GHz and computed the noise power spectrum of the combined 143 GHz map using jackknife analysis as described in Sect. 7.6. We found that the noise at small scales increased by a factor comparable to the square root of the inverse ratio between the number of hits with and without flag extension, as expected in the limit of no residual glitch contamination. The noise increased by a larger factor at the lowest multipoles. We interpret this as being due to the loss of accuracy of the destriping map making algorithm as a result of the extra data flagging.

Overall, 10 to 15% of the data are flagged as unusable due to the presence of glitches. Figure 11 summarizes the data loss caused by cosmic rays for each individual bolometer, while Table 1 gives the average over detectors within the same frequency channel. This is to be compared with other data losses, in particular the phases of depointing which are not used at present. A full ring has a mean duration of 46.5 min. On average, 3.8 min (8.3%) of data are taken during re-pointing manoeuvres between stable pointings. They are currently not used, so at present we lose about 20% of the data due to depointing and glitches. Data

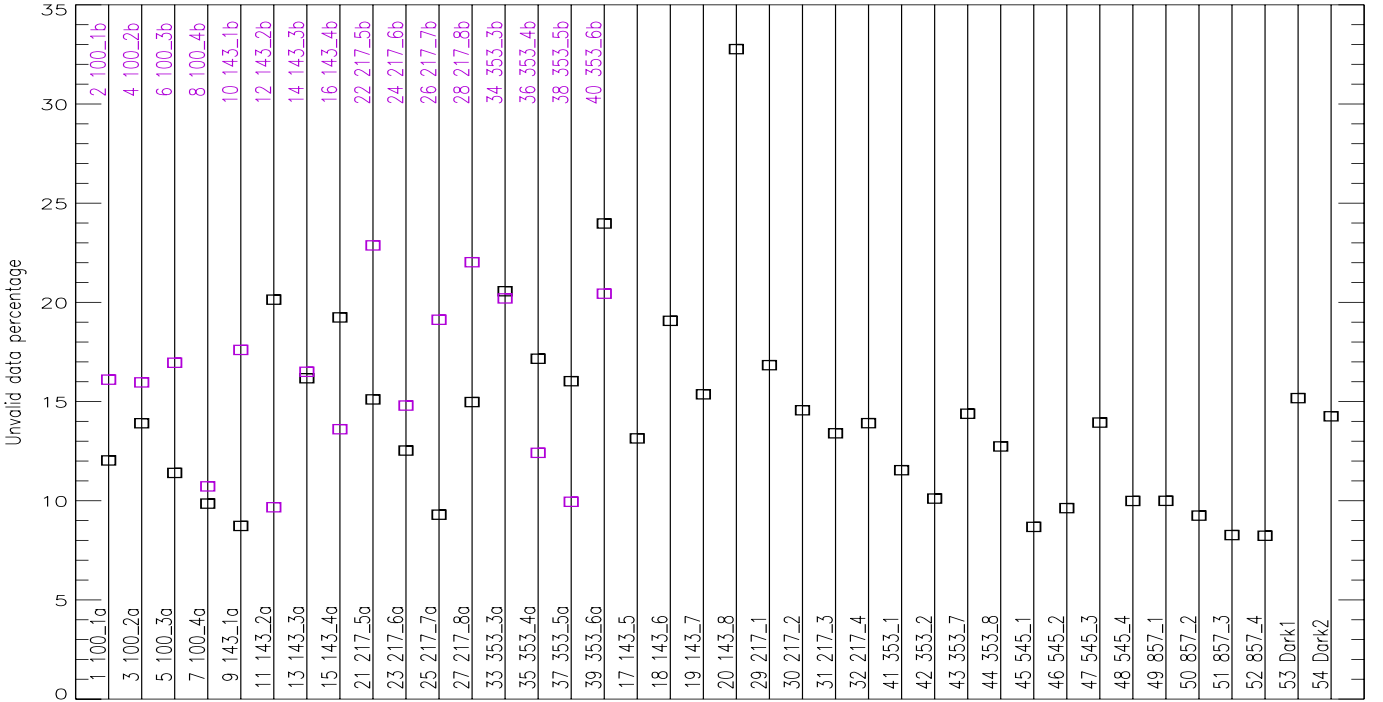


Fig. 11. Average fraction of data lost in the first sky survey for each bolometer as a result of glitches. The number for the 143_8 is not representative since it is corrupted by RTS.

Table 1. Summary of the average data loss because of glitches per bolometer frequency (the number in the first line correspond to the frequency of the channel).

	100	143	217	353	545	857	Dark
N_b	8	11	12	12	3	3	2
%	13.4	15.4	15.8	15.8	9.4	9.2	14.7

Notes. N_b is the number of bolometers used, i.e. excluding bolometers affected by RTS noise.

compression in the high frequency channels leads to negligible amounts of lost data. In addition, the deglitching processing produces anomalous results in some rings. Statistical inspection of all rings showed that 0.5% are anomalous and these are flagged and discarded from further analysis.

4.2.4. Glitch simulations and residuals

To assess the effect on the data of our glitch removal procedure, we have simulated TOIs of noise with glitches representative of the three populations described in Sect. 4.2.1. We have used, as a reference, the glitch amplitude distributions measured for one of the 143 GHz bolometers (cf. Fig. 12). Since the populations are not well separated in the data for glitch peak amplitudes below $\approx 40\sigma$ (where σ is the rms of the noise) the simulated distributions for all populations have been extrapolated using two-power law models at the faint end, keeping the sum of the distributions identical to the data down to about 5σ . Figure 12 compares the measured and the model distributions, as well as the recovered distributions after applying the glitch analysis on simulations. Distributions for other bolometers are rescaled in glitch amplitudes by a factor specific to each population. We have observed that this factor varies strongly from bolometer to bolometer for

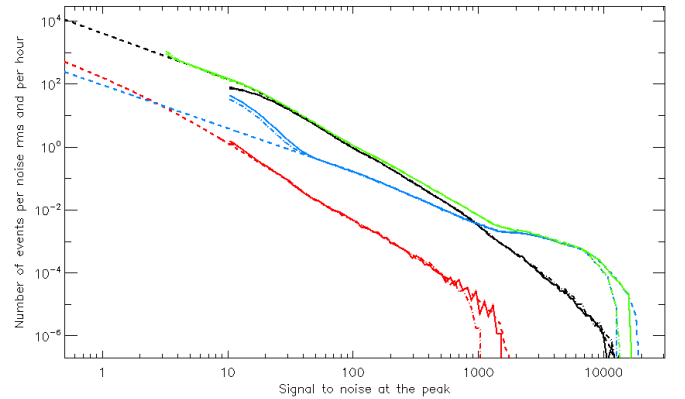


Fig. 12. Distributions of the three populations of glitches for one PSB-a bolometer at 143 GHz; black is for long glitches, blue is for short glitches, and red is for the very long ones. Green is for the total. The measured distributions from real data are displayed with solid curves, the model with dashed curves and the measured distributions in simulation with dot-dashed curves. One can see the excellent agreement between the estimated distributions from real data and from the simulations. The total distribution is well measured down to 3.2σ . The separation of glitches into different populations is not attempted below 10σ (σ stands for the rms of the noise), and is quite secure above 40σ for PSB-a, and above 200σ for PSB-b and SWB. A two-power law model with breaks has been used to represent the glitch populations at the faint end. For this bolometer, the breaks are fixed to $\approx 100\sigma$ for the short glitches, $\approx 20\sigma$ for the long and $\approx 3\sigma$ for the very long glitches.

the long glitch distributions, and is about constant for the short one.

The (sum of) four-exponential glitch templates used for the detection were also used to simulate the glitch tail profiles. The fast part with a decay given by the bolometer time-constant (not included in the tail templates) is added. Glitch amplitudes and

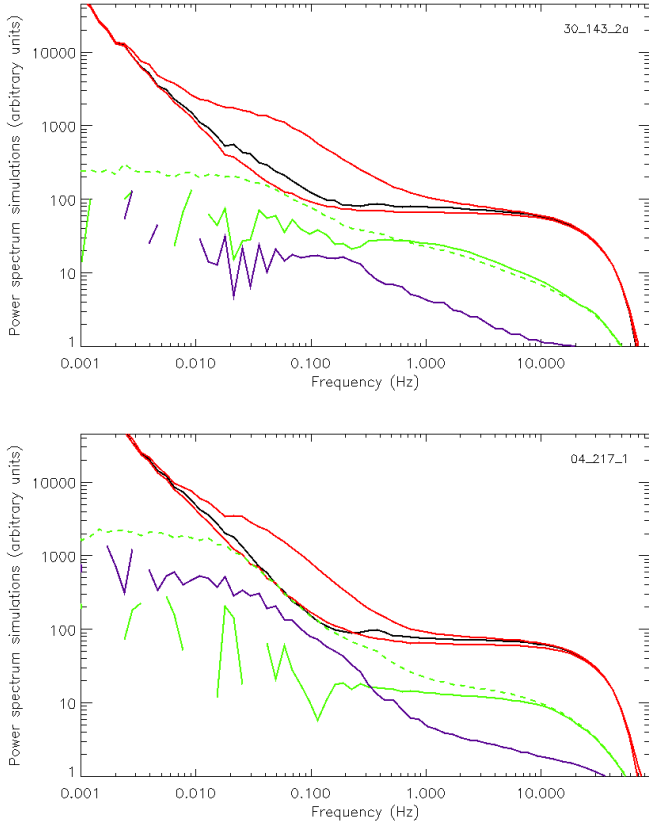


Fig. 13. Power spectra of the residual noise in simulations after template subtraction and flagging (in black) for one bolometer (PSB-a) at 143 GHz (*top panel*) and one SWB at 217 GHz (*bottom panel*). Both bolometers have high rates of long glitches. No other processing has been applied to the simulations, except a 3-point filter (as applied to real data before deglitching), the effect of which can be seen at frequencies above 10 Hz. This can be compared with the surrounding red curves. The top red curves in both plots correspond to the power spectra of the simulated data (pure noise+glitches) before template subtraction. The lower red curves correspond to the power spectra of the pure noise TOIs used in generating the simulations. The green dashed curves are the power spectra of the residual glitches remaining after flagging and template subtraction, which are measured from the difference between the estimated and the input TOIs of glitches. Those curves are not exactly equivalent to the difference between the black and the bottom red curves because some noise is subtracted by the template subtraction process. The green curves are the cross-spectra between the input TOIs of glitches and the cleaned data, and the blue curves show the cross-spectra between the recovered TOIs of glitches (which are subtracted from data) and the input noise TOIs.

sub-sample arrival times are set randomly according to Poisson statistics. Glitch profiles are integrated within samples. This gives some dispersion in the peak-to-template amplitude ratio depending on the arrival time within the sample integration duration, as observed in data. A non-linearity coefficient is also applied to the amplitude of the long glitch template relative to the fast part of the glitch, also as observed in data.

The excellent agreement between the recovered distributions in data and simulations displayed in Fig. 12 gives us confidence in our glitch modelling.

Figure 13 shows the noise power spectra after deglitching and template subtraction in simulations of two bolometers (one PSB-a and one SWB) with a high rate of glitches. Power spectra of the outputs are compared to input noise power spectra. We can

see a small residual contamination from glitches remaining at frequencies higher than 0.01 Hz for the PSB-a, which is at most at the level of the input noise around 0.04 Hz. For the SWB, the contamination is stronger and of the order of the noise between 0.01 Hz and 0.1 Hz. Residual contamination is at the 10–20% level above 0.2 Hz in both cases. The stronger residual contamination for a SWB (and PSB-b) as compared to a PSB-a, is explained by the fact that the intermediate 60 ms decay, which is a trigger for the template fitting, is lower in the SWB, hence the ≈ 2 s tail (mostly responsible for the noise excess) is removed less efficiently. Also, the knee frequency for the SWB at 217 GHz is higher than that for the PSB-a at 143 GHz. Nevertheless, at all frequencies the residual contamination does not exceed the input noise level.

Figure 13 shows the cross-spectrum between the template subtracted data and the input glitch TOI in simulations (green curve). The low level of relative correlations below 0.1 Hz as seen by comparing the green dashed and solid curves, indicates that the excess noise residuals associated with glitches are dominated by the errors in the glitch template fit, whereas above 0.1 Hz the high level of relative correlations show that the excess noise is due to unidentified (or unsubtracted) glitches below the detection threshold. This has been confirmed by inspection of the difference between input and recovered glitch TOIs. The measured cross-correlation between the input noise in simulations and the recovered glitch TOI (blue curve in Fig. 13) indicates that by removing the latter from the data, some detector noise is also removed. This is because errors in the glitch fit are naturally correlated with the noise in the data. This effect is at about the 20% level at 0.1 Hz.

To evaluate potential biases in the recovered sky signal which would be introduced by the deglitching procedure, we have computed, using simulations, the cross-power spectrum between the recovered signal residual, estimated from the difference of pure signal minus recovered signal phase binned rings, and pure signal phase binned rings for one detector at 143 GHz. Results are shown in Fig. 14 including and excluding the glitch flags to project the pure sky signal TOI. The recovered signal phase binned rings is a product of the deglitching procedure at the last iteration as already described. We do not see any significant correlations at 143 GHz nevertheless we see some small effect at the level of a tenth of a percent for the two highest frequencies. This is caused by the strong Galactic signal, which leads to a higher glitch detection threshold and hence less complete subtraction of glitches. We have also constrained potential biases on the signal by computing the cross-spectrum of the estimated sky signal from real data on rings with the estimated glitch templates projected on the same rings for one detector at 143 GHz. We have not found any significant correlation at any ring frequency after averaging the cross-spectra of a thousand rings. The same test applied at 545 GHz have shown a very small anti-correlation between the reprojected glitch templates and the galactic signal of the order of 0.04% of the signal. This is due to the fact that less glitches are subtracted on average while observing strong sources, as the detection threshold is increased depending on the intensity of the signal. This leads to a negligible bias after template subtraction.

4.3. Gain

Bolometers are non-linear devices. The voltage output must be converted to absorbed power by using a gain model. This is discussed in the companion paper by the [Planck HFI Core Team \(2011a\)](#). The slowly varying gain is corrected by using

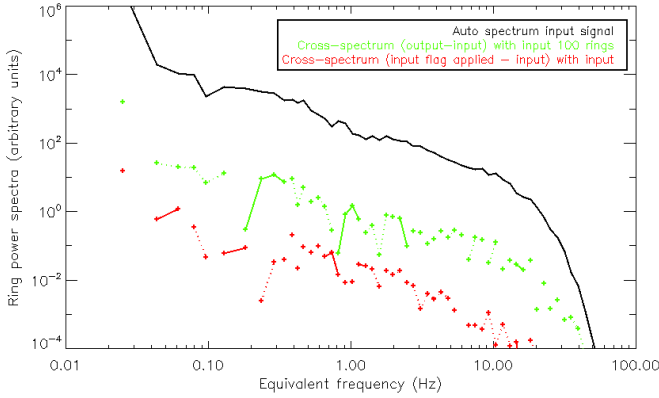


Fig. 14. In black: power spectrum of pure simulated signal at 143 GHz projected on 1.5 arcmin rings. In green: cross-power spectrum between (1) pure signal minus recovered signal and (2) pure signal. Solid lines join positive values and dotted lines negative values. In red: cross-power spectrum between (1) pure signal minus pure signal flags applied; and (2) pure signal. We see no apparent bias in signal estimation from either template subtraction or flagging.

parameters measured during the ground-based tests and in-flight calibration periods. The time response is dealt with in Sect. 4.6. The gain factor is typically of the order of 10^9 V/W. The gain non-linearity amplitude for typical signals (the dipole or the Galaxy) is of the order of a few parts in 10^4 .

4.4. Decorrelation of thermal fluctuations

The main thermal fluctuations identified originate from the bolometer plate at 103 mK and are monitored by four thermometers, one of which is used for long term (hour scale) regulation. Unfortunately, the thermometer data is seriously affected by glitches and proved to be unusable. We rely instead on the deglitched signal from the two dark bolometers, which are smoothed with a running window with a width of 2 min and combined to produce a template of the thermal fluctuations. Two correlation coefficients per bolometer, derived from two weeks of flight data acquired before the start of the survey, are used to decorrelate the bolometer signal using the template. This step reduces the correlation coefficient from ~ 0.5 to zero (although these coefficients have a rather large scatter of about 0.25 when computed on only 50 rings). Figure 15 displays the effect of the decorrelation on a few TOIs, and Fig. 16 shows the effect on a TOI power spectrum.

4.5. 4 K cooler line cleaning

The 4 K mechanical cooler induces some noise in the bolometer signal via electromagnetic interference and coupling, as well as microphonic effects. The 4 K coolers main operational frequency ($f_{4K} = 40.0834$ Hz) is locked-in with the signal modulation frequency ($f_{4K} = \frac{4}{9}f_{\text{mod}}$ with $f_{\text{mod}} = 90.1876$ Hz). The 4 K cooler systematic effects therefore show up in power spectra of the signal TOIs as narrow lines at predictable frequencies and with a power larger than the noise by one or more order of magnitude. Here we describe a simple method that we have used to remove these lines.

Lines at nine frequencies ($\sim 10 \times n$ Hz with $n = 1$ to 8, and at 17 Hz) were systematically found in the power spectra that could be traced to the 4 K cooler. They affect the 72 detectors

in different ways. Given a chunk of 54 data samples, taken at the acquisition frequency $f_{\text{acq}} = 2f_{\text{mod}} = 180.3751890$ Hz for a given detector, the 4 K cooler lines show a Fourier pattern at a period of $3n$ and 5 samples (i.e. at multiples of $f_{\text{acq}}/54$) for the nine lines.

The removal method assumes that the lines correspond to single Fourier components of the signal. We compute the a (cosine) and b (sine) coefficients of the Fourier series at the line frequencies over a given period of time, L_{cut} , from the input TOI (which is interpolated over flagged data). We then construct a timeline by summing the 9 cosine and sine components of the Fourier series and subtracting it from the initial data.

The cooler lines contribute coherently to the phase binned rings only when their frequencies are close to a multiple of f_{spin} . Given the roughly random variation of the spin rate (3σ) between 59.95 and 60.05 s (Planck Collaboration 2011a), this occurs in 1–2% of the rings. Indeed the natural line width is $f_{\text{spin}}/N_{\text{circle}}$, where $N_{\text{circle}} \sim 30$ –40 is the number of circles in a ring, to be compared to the separation between sky-signal harmonics of f_{spin} .

The sky signal may therefore impact on the measured cooler lines and the computed a and b coefficients for those rings. In the extreme case of strong sources this may induce ringing in the data. The effective frequency window width around each of the nine 4 K cooler lines for this analysis is defined by $\Delta f = f_{\text{acq}}/L_{\text{cut}}$. When a multiple of f_{spin} happens to fall into these windows, the a and b coefficients will be altered by the signal. Hence, the ringing increases inversely to L_{cut} requiring us to use larger values of L_{cut} .

On the other hand, the accuracy to which we remove the 4 K cooler lines from the TOI is limited by their time variability and therefore pushes us to decrease L_{cut} . To mitigate the variability of the lines and the ringing effect described above, a trade-off was chosen by taking $L_{\text{cut}} = 345\,600$ samples (31 min 56 s) for all channels (a multiple of 54 samples).

Figure 17 presents the power spectrum around nine of the 4 K lines. The 4 K lines are subtracted reasonably well except for the line at 70 Hz for the high frequency bolometers.

We have performed simulations to quantify the effect of the 4 K-line removal on the final HFI maps. The main adverse effect occurs when one of the removed 4 K lines happens to straddle one of the sky harmonics. In such cases the missing harmonics from the sky signal produces a “stitching” pattern on the map, which can be pronounced if there are strong signal gradients along the ring (e.g., due to a very bright point source). Typically, a point source produces a “stitching” pattern with an amplitude of about 10^{-5} of the source signal. Troublesome artefacts are rare enough that, for now, we either remove such rings from the analysis or discard “stitching”-related spurious sources from the ERCSC. The simulations show that a negligible number of spurious point sources remain.

4.6. Temporal transfer function deconvolution

A simple FFT is used with the processed TOI to deconvolve the temporal transfer function. This temporal transfer function is determined by using Mars crossings (see Sect. 6) and optimising the symmetry of the measured output beam profile (see Planck HFI Core Team 2011a). A regularisation filter (a low pass filter with a width of 5 Hz, specifically $\sin^2 \left[\frac{\pi}{2} \left(\frac{f_{\text{mod}} - f}{5 \text{ Hz}} \right) \right]$) is applied simultaneously to the inverse of the temporal transfer function. Before applying the FFT, the TOI samples which are flagged as invalid, are filled with a ring-based interpolation. The Jupiter

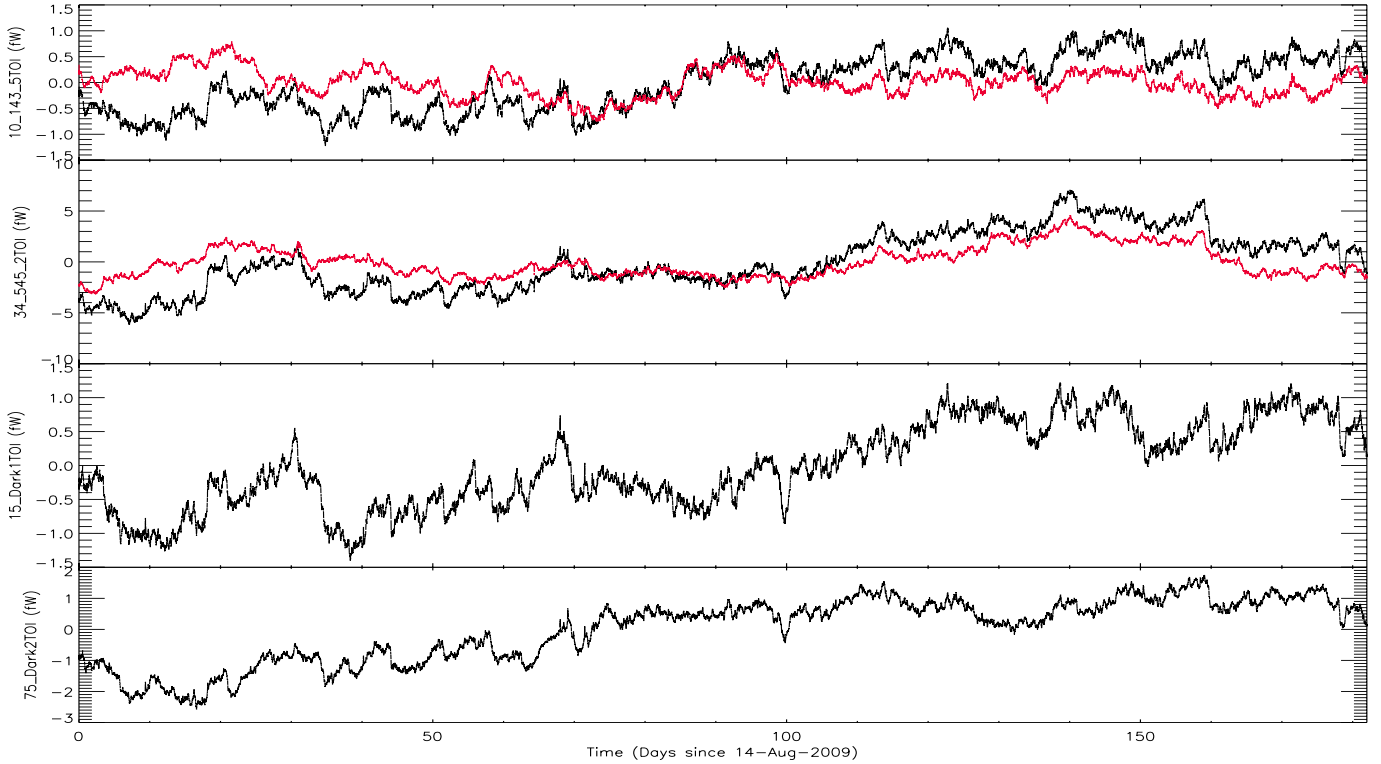


Fig. 15. Trend in processed TOIs of the 143-5 and 545-2 bolometers over the first sky survey period (180 days), before (*in black*) and after (*in red*) the 100 mK fluctuations are removed (as monitored by the two dark bolometers, Dark1 and Dark2, in the two lower plots). These data are averages over 1 min of processed TOIs, smoothed to one hour. For the dark bolometers, one unit (1 fW) is equivalent to about $10 \mu\text{K}$.

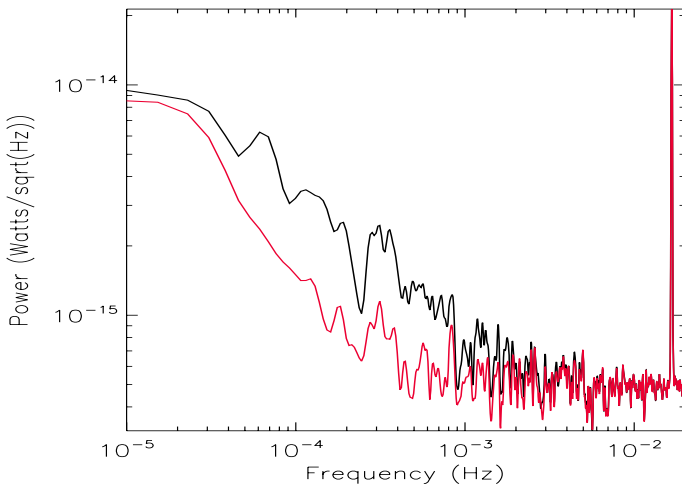


Fig. 16. Power spectrum of the TOI of the 143-5 bolometer, before (*in black*) and after (*in red*) the 100 mK fluctuations traced by the dark bolometers (smoothed by a 2-min box kernel) have been removed. The removal of 100 mK fluctuations affects only the very low frequencies below the first sky harmonic at $f_{\text{spin}} \approx 0.017 \text{ Hz}$.

signal is replaced by a combination of linear interpolation and noise to avoid long duration effects (ringing) of the deconvolution of this huge signal along the scan. These interpolated samples are flagged and not projected onto maps.

To provide an assessment of how uncertainties in our current knowledge of the transfer functions translate into processed data, we consider the statistical uncertainties in the determination, and propagated these uncertainties to source fluxes and angular power spectra. This was obtained by means of 50 Monte-Carlo simulations with the following elements: (i) sky simulation;

(ii) projection to time series for all the detectors within a frequency band, using one year of flight pointing data; (iii) convolution of each time series with a time response realization; (iv) deconvolution by the nominal time response function; (v) projection to a single map per band. An overview of the technical implementation of our simulations is given in Sect. A.7. The time response realizations are estimated as transfer functions in Fourier space, based on the model and error budget described in Planck HFI Core Team (2011a). The realizations include statistical errors, error correlations, and the estimated level of systematic error. Correlations among errors in transfer functions of different detectors are not included. Convolution and deconvolution transfer functions are normalized at the temporal frequency corresponding to the cosmic dipole signal observation, to mimic dipole/large-scale calibration. Moreover the time response is such that the point sources are not shifted in time. For the point source flux assessment, the simulated input sky included only point sources and diffuse Galactic emission. For assessing the impact on angular power spectra, the simulated sky was a realization of the CMB.

The results can be summarized as follows:

- aperture flux of point sources has an average error of 4% at 857 GHz and 0.5% at 143 GHz;
- the error on the angular power spectrum is order of 1% above multipole $\ell = 100$ and reduces to 0.1% at larger scales.

This sets the level of errors to which the results in the early papers need to be immune to, provided the errors on the transfer functions assumed here are realistic. We are gratified to have achieved this level of accuracy within only a month of the data being acquired. This rapid delivery of accurate processed data was one of the key elements which allowed the early science analyses described in this special issue. Nevertheless, the

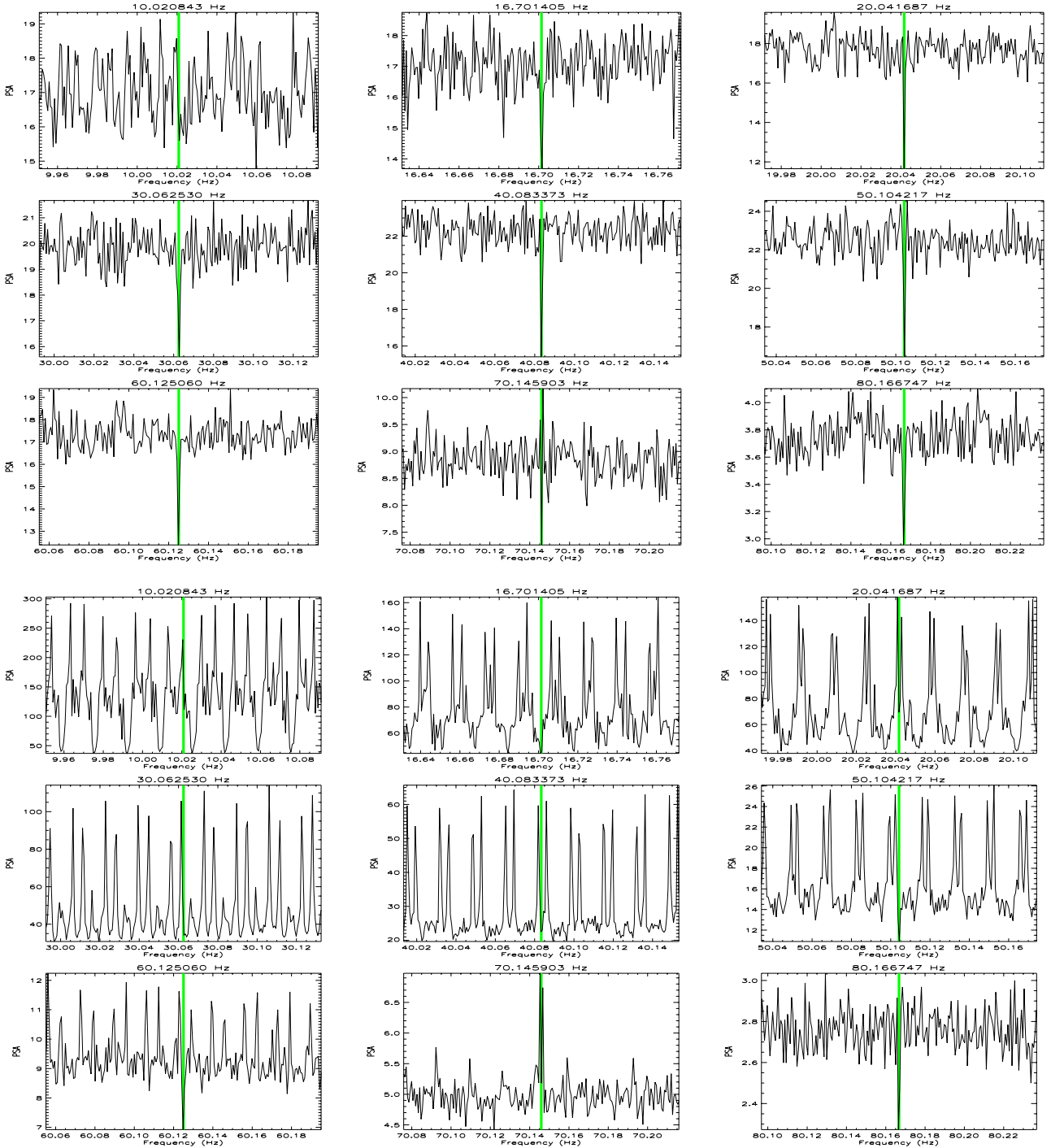


Fig. 17. The power spectrum amplitude around the nine 4 K lines for the two bolometers 143-5 (*upper panels*) and 545-2 (*lower panels*). The vertical bar shows the line frequency. The spectra are obtained by averaging 200 individual ring spectra (see Sect. 5) to reduce the noise. The residual lines are at most comparable to the noise level. The signal shows up at the harmonics of the spin frequency ≈ 0.16 Hz. In the CMB channel of the *top panel*, the high harmonics of the signal do not stand out against the noise, but they are clearly visible in the *bottom panel*. Note that the spin frequency variations between rings yield the complex signal line pattern of interleaved combs.

accuracy of the data is certainly not sufficient to reach the more demanding cosmological science goals of *Planck*. In the next two years, improving the fidelity of the data will be the major focus of work by the HFI Core Team. This task will be greatly aided by the increased level of redundancy offered by more data but we also expect to identify other systematic effects that will need correction, in addition to those described here. These will be described in detail in future papers.

4.7. Other sources of noise

Three bolometers (143_8, 545_3 and 857_4) have been identified as being affected by Random Telegraphic Signal (RTS, see [Planck HFI Core Team 2011a](#)). These detectors are not used to build frequency maps. There is no evidence for a significant RTS contribution to the noise of other detectors.

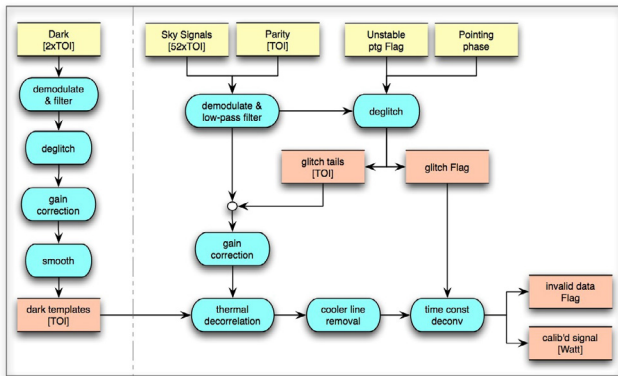


Fig. 18. TOI processing data flow. See text for details.

More quantitatively, we have used simulations to assess the minimum jump between signal levels that can be detected by a Viterbi-based algorithm (Viterbi 1967). We derive a best-fit distance between two states (D , measured in units of the noise rms of that bolometer), as well as the per-sample improvement in the fit from using two states, δL . For bolometers at frequency ≤ 353 GHz, there are only a few single rings which show $D > 1$ and $\delta L > 0.03$ in the real data whereas the algorithm finds all RTS rings in a simulations with $D > 0.5$. For higher frequencies, the upper limit on any RTS is somewhat less stringent. We conclude that the impact of any undetected RTS on the final data products is negligible.

Finally, as discussed earlier, there is a low frequency excess noise which is seen in all detectors and as a result the amplitude at the spin frequency $f_{\text{spin}} = 0.016$ Hz is higher by a factor of about three than the white noise level (as can be seen in Fig. 9a and 21), which as we shall see later results in increased noise at large scales in the maps, though at a significantly lower level than the cosmic variance. Given our study of glitch and RTS residuals, neither are likely to contribute significantly to this excess. One possible explanation mentioned in Planck Collaboration (2011b) may be thermal fluctuations linked to high energy cosmic ray showers which are not common to all detectors, as indicated by the weak level of cross-correlation, at low-frequency, shown in Fig. 9b.

4.8. The overall TOI processing pipeline

Figure 18 provides an overview of the TOI processing data flow. The dark detectors are processed first to prepare them for use as templates in the 100 mK decorrelation of the other detectors. Each bolometer is then processed independently of the others. The independence of the processing enables various jackknife tests to be constructed to assess errors. The TOI processing pipeline chains the modules described above in a specific order. Namely, the raw signal TOI in Volts is read from the database. It is demodulated and filtered. The deglitching step produces a flag TOI and a new bolometer TOI in which glitch tails have been corrected for. This new TOI is then gain-corrected. A (small) decorrelation from the smoothed dark templates is then applied. For Fourier-domain processing we need to fill the gaps. Hence, for invalid data samples, an interpolation is performed using the bolometer average signal computed from phase-binned ring derived by Fourier-Taylor expansion (see Sect. 5 and Appendix C.1.3 for details). We then remove the 4 K cooler lines and finally deconvolve the temporal transfer function. Two additional flags are created for use in the map-making

or noise estimation. These are: (1) flags around planets, asteroids, and comets⁶, as moving bodies should not be projected onto the maps; (2) flags of strong signals (mostly Galactic plane crossings) that are discarded from noise estimation and destriper offset computation. Note that the invalid data flag corresponds to data with the glitch flag set, together with the very few missing data samples from the telemetry and from compression saturation (for a huge glitch, on average, once every 500 rings and when we crossed for the Galactic centre at 857 GHz for the first time, see Sects. 3.2 and 3.3).

Examples of cleaned TOIs produced are shown in Fig. 19. The pipeline also produces TOI in which the ring average signal has been removed (see Fig. 20). This provides the basis for estimating the noise as detailed in the next section.

5. Detector noise estimation

In this section, we investigate the statistical properties of the detector noise timelines from flight data, both on raw and clean TOIs. Ground based measurement give only approximate indications of the noise characteristics as many features (e.g., long term drifts, microphonic noise) depend on the satellite environment and the instrument settings in-flight. The difficulty in interpreting flight data is to estimate the noise properties in the presence of signal, which is the goal of the approach described below.

It is shown in Appendix C that the joint maximum likelihood estimate of the signal and the noise spectral parameters (taken here as flat frequency bin powers) can be achieved by using the redundancy of the scanning strategy. In the case of the *Planck* scanning strategy, a flat weighting in the signal estimation on rings is very close to optimal, so there is no need to iterate the signal and noise power estimation.

The main difficulty in estimating the signal is to precisely sample the signal in phase on rings. This is achieved by making the assumption that the signal content is band-limited on the rings, together with an approximate (but arbitrarily accurate) irregular sampling method based on Fourier-Taylor expansions, leading to so-called Fourier-Taylor rings (FTR, see Appendix C.1.3). Note that this signal removal approach is only possible when the estimation is done on a ring-by-ring basis (map based signal estimation might replace it in the future).

The pipeline can thus be summarized as follows:

1. estimate the signal content of each ring using the scanning redundancy;
2. subtract this estimate from the original data timeline to produce an estimate of the noise content;
3. compute edge-corrected, averaged periodograms of the estimated noise timeline;
4. optionally adjust a parametric model of the noise spectrum to the periodograms to determine the noise parameters.

Each step is described in further detail in Appendix C. Step 3 is repeated on all rings, though other zones can also be defined and used for this purpose.

⁶ For definiteness, here follows the list of solar system moving bodies flagged out. 26 Asteroids: Hygiea, Parthenope, Nemesis, Victoria, Egeria, Irene, Eunomia, Psyche, Melpomene, Fortuna, Ceres, Massalia, Amphitrite, Pallas, Bamberga, Juno, Daphne, Eugenia, Vesta, Davida, Europa, Interamnia, Iris, Thisbe, Flora, Metis; 20 Comets: Broughton, Cardinal, Christensen, d'Arrest, Encke, Garradd, Gunn, Hartley2, Holmes, Howell, Kopff, Kushida, LINEAR, Lulin, McNaught, NEAT, Shoemaker-Levy4, SidingSpring, Tempel2, Wild2.

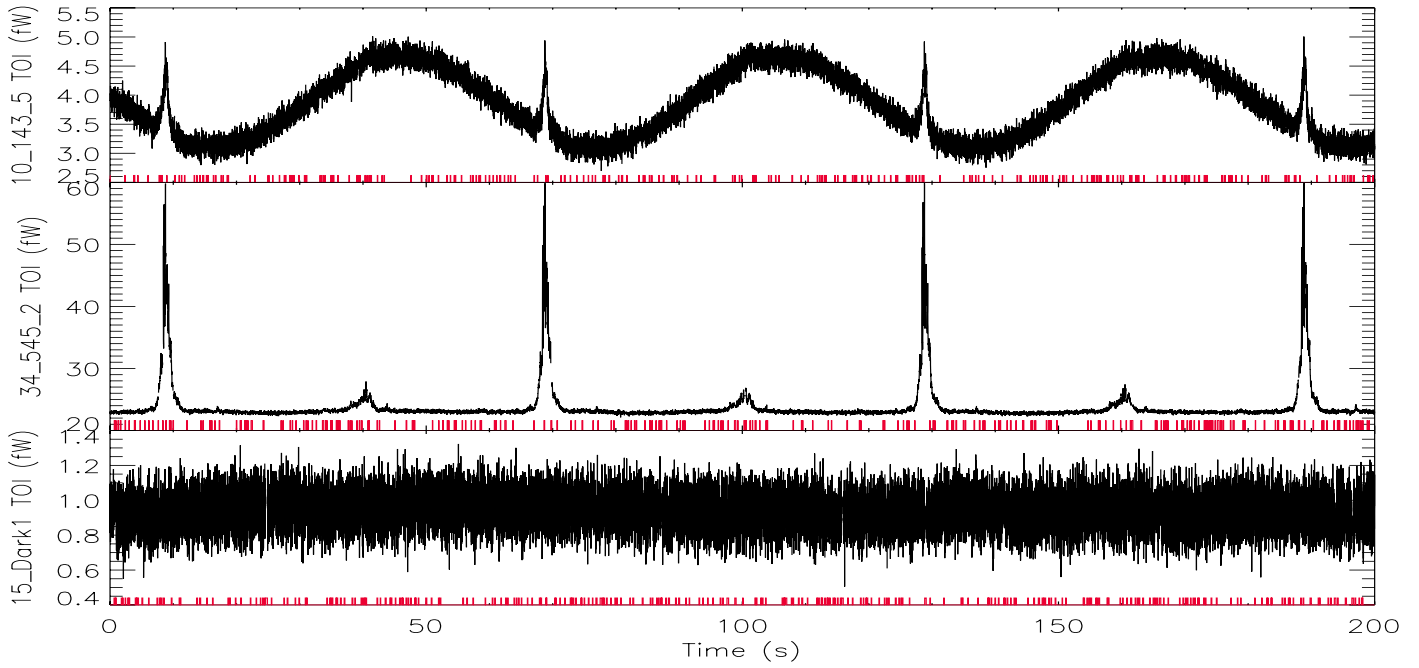


Fig. 19. Processed TOI for the same bolometers and time range as shown in Fig. 4. Times where data are flagged, are indicated by the red ticks at the bottom of each plot.

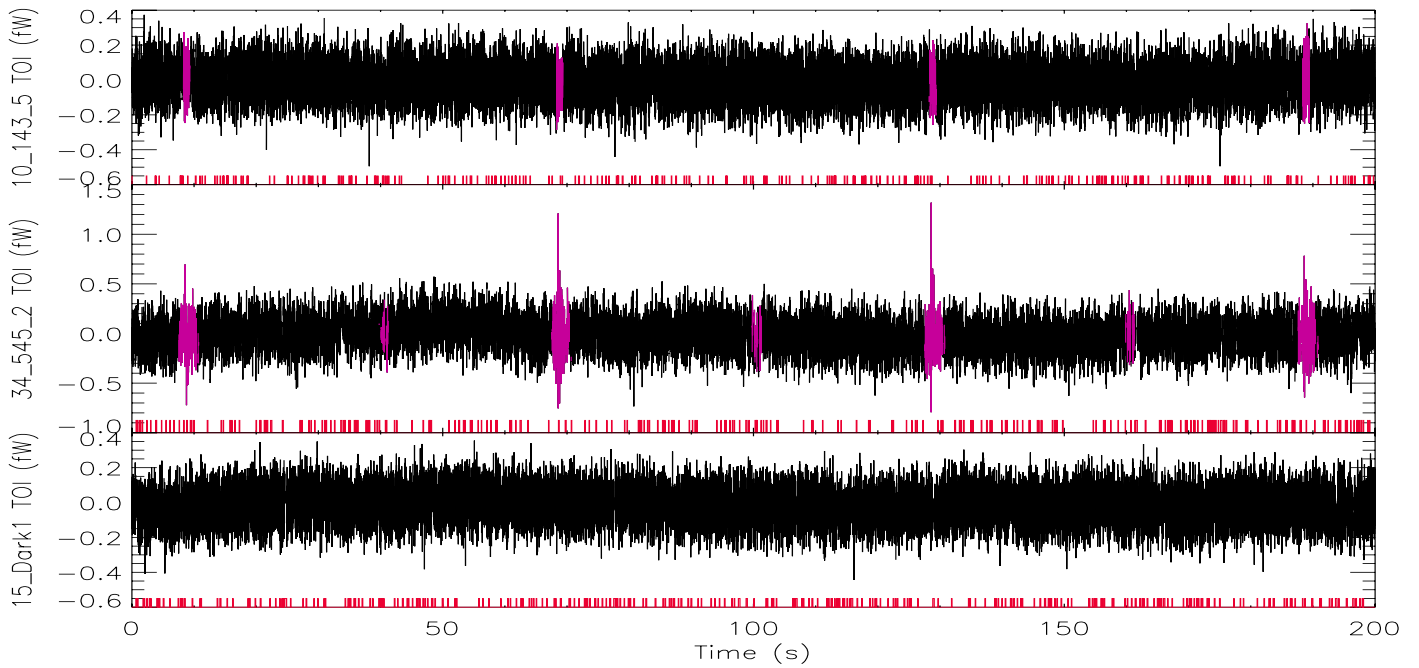


Fig. 20. Processed TOI as in Fig. 19, but with the ring averaged signal subtracted to enhance features near the noise limit. Times where data are flagged, are shown by the red lines at the bottom of each plot. Purple zones show where the strong signal flag is set and where the phase-bin ring average subtraction is not expected to yield a perfect cancellation of the signal.

The last step is implemented as a maximum likelihood estimate of the spectral parameters (e.g., Noise Equivalent Power or NEP, knee frequency and spectral index of low-frequency noise), where the distribution of the averaged periodogram estimate is approximated as a product of χ^2 distributions with the appropriate number of degrees of freedom. The noise parameters are determined from the spectra of all rings (or other zones), which is useful in monitoring the evolution of these parameters with time. The results discussed below were determined by fitting a pure white noise model in the 0.6–2.5 Hz frequency range.

Figure 21 shows the noise power spectrum estimates for three bolometers: 143–5, one of the most sensitive CMB-dominated channels (top); 545–2, operating at a frequency where the dust emission of the Galaxy and IR galaxies dominate the signal (middle); and the Dark1 bolometer (bottom). Several features are apparent in this figure. The spectrum is flat at intermediate frequencies, which gives an estimate of the bolometer’s NEP. At low frequencies, there is a rise of power that begins at effective knee frequencies considerably higher than those measured during ground based calibration. The extra low-frequency

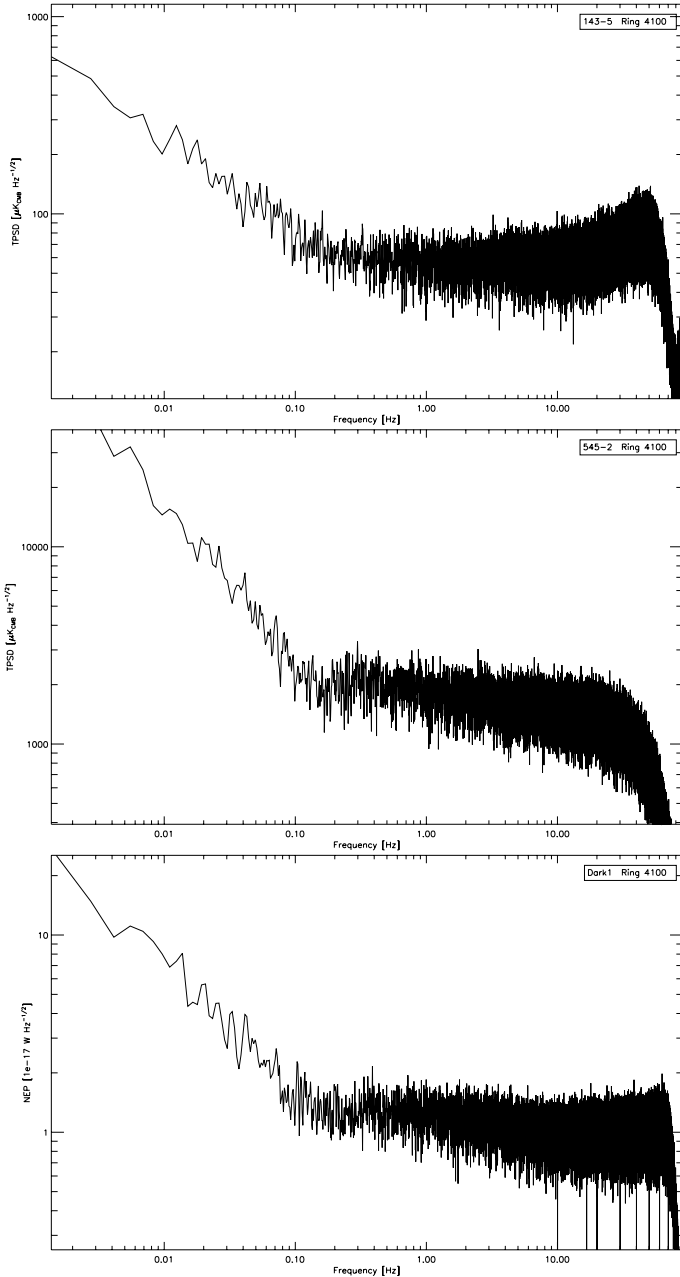


Fig. 21. Examples of noise power spectra for the bolometers 143-5 (top), 545-2 (middle), and Dark1 (bottom). The first two have been calibrated in CMB temperature units, by using the calibration coefficients derived during the map making step. The last spectrum is in Watts. The central region shows a nearly white noise plateau, with a low frequency “ $1/f$ ” component, and a high frequency cut-off due to the filtering of frequencies above the sampling frequency. At 143 GHz, the upturn due to the deconvolution of the (bolometer dependent) temporal transfer function is clearly seen (see details in Sect. 4.6).

power is believed to be mostly due to residual thermal fluctuations from cosmic ray hits (those which are not common to all detectors, see Sect. 4). The high frequency part of the spectrum shows a rise of power due to noise amplification by the transfer function deconvolution described in Sect. 4.6 and, in a few cases (not shown), weak residuals of lines induced by the 4 K-cooler that have not been completely removed.

Table 2 gives the average Noise Equivalent Temperatures per frequency channel (derived by using the calibration coefficients stored in the `imo` at the map-making stage) and, for

Table 2. Mean noise equivalent temperatures for each channel.

Frequency [GHz]	NET [$\mu\text{K}_{\text{CMB}} \text{s}^{1/2}$]	Goal
100P	65	100
143P	53	82
143S	41	62
217P	79	132
217S	68	91
353P	329	404
353S	220	277
545S	1410	1998
857S	41 220	91 000

Notes. P and S after the frequency value indicate polarised (PSB) and unpolarised (SWB) bolometers. The last columns give the HFI sensitivity goals, as can be found in Lamarre et al. (2010).

reference, the target values of the HFI as given in the HFI pre-flight paper⁷ (Lamarre et al. 2010). In the averaging per channel, some detectors showing pathological behaviour (Random Telegraphic Signal, sometimes referred to as “pop-corn” noise) were removed, as they are not used for map-making and other science analyses. The measured average NETs per channel are, in all cases, much better than the goal values. As described in the Instrument performance companion paper (see Planck HFI Core Team 2011a, and in particular Fig. 21), the performance improvement as compared to goals comes from a lower background (and therefore of the corresponding photon noise) than initially assumed.

6. Beams and focal plane geometry

The pipeline for geometrical calibration determines, simultaneously, the shape and location of the beam for each detector in the focal plane. Detector locations are determined as three-dimensional rotations with respect to the telescope attitude (Shuster 1993). Beam shapes are parametrized in two ways: (1) as asymmetric Gaussians; (2) with Gauss-Hermite polynomials of arbitrary order. A visualization of the focal plane is shown in Fig. 22.

The pipelines are capable of extracting measurements from planets as well as from fixed sources. Planet ephemerides are calculated using the Jet Propulsion Laboratory Horizons software⁸ (Giorgini et al. 1996) which is programmed with Planck’s orbital information. Movement over the course of a single planet observation is significant in some cases and must be taken into account. Here, a *single observation* refers to a set of adjacent rings containing the object, typically lasting for about one week. Our planet observations are summarized in Table 3.

Single observations of Mars and Saturn provide high signal-to-noise measurements of the beams and focal plane geometry. Neptune and Uranus also provide strong detections. However, measurements of extragalactic and Galactic sources are limited by CMB confusion and by low signal-to-noise. Jupiter’s very large flux drives some detectors nonlinear and therefore results in artefacts which are removed from the processed TOI. Mars and Saturn are therefore the primary calibrators used in this section.

⁷ The pre-flight paper provides goals for the polarised detectors in addition to the SWB only values of the Blue Book Planck Collaboration (2005). It also sets the 100 GHz channels goal twice worse than in the Blue Book.

⁸ <http://ssd.jpl.nasa.gov/?horizons>

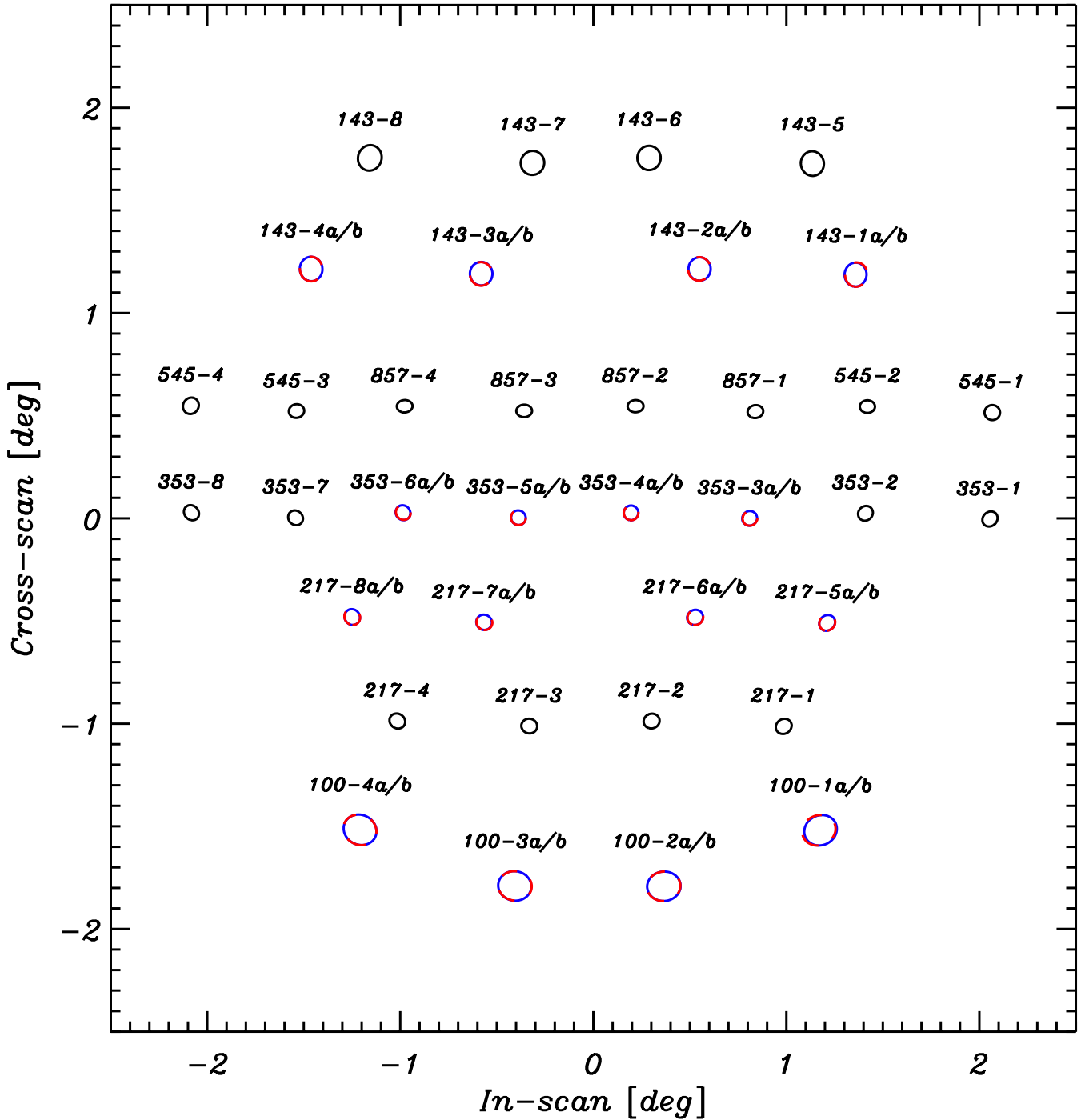


Fig. 22. The HFI focal plane on the sky. Individual detector locations are as measured, and beam shapes are represented by ellipses at the FWHM level. For polarized detectors, the beam shapes are over-plotted in red and blue and labelled (a/b) but are in practice indistinguishable by eye. Fits are on destriped data (except for 143-8) and represent the values from the Gaussian-only fits to the data.

From a measurement of the position of each detector, we can compute an overall rotation and scaling of the complete focal plane with respect to a fiducial model (e.g., the pre-flight optical model). These parameters can be used to track mechanical and optical changes in the telescope/detector system, although due to the phase shift induced by the transfer function, we are insensitive to any shifts in the scan direction.

Details of the algorithm for focal plane reconstruction, its pipeline implementation, and validation on simulations, along with a separate algorithm used to derive a preliminary estimate of the focal-plane geometry, are given in Appendix B.

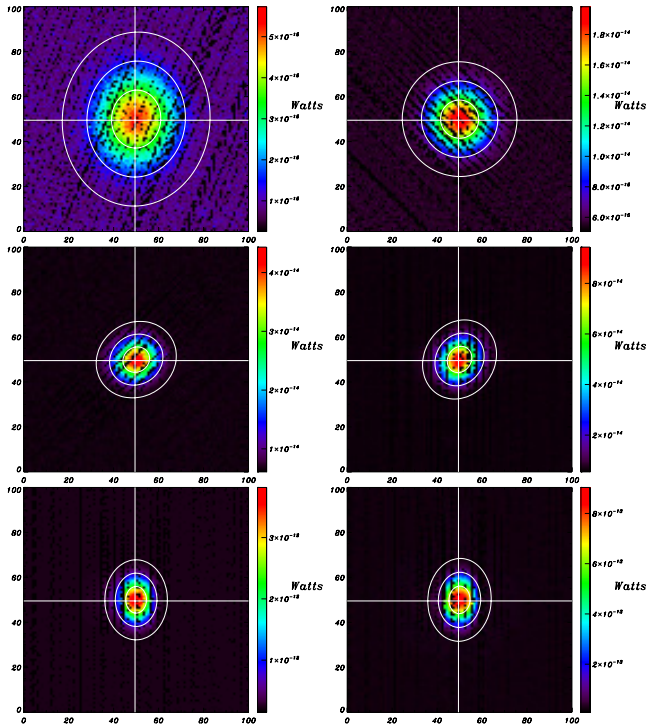
6.1. Results

6.1.1. Focal-plane geometry

In Fig. 23 we show maps made from the first crossing of Mars, which provides the highest signal-to-noise measurement (that is not subject to nonlinear response) of the focal-plane geometry and beam shapes. Using the algorithm described in Appendix B, we fit the data going into these “minimaps” to a Gaussian or Gauss-Hermite model, extracting the positions of the centre of the beams and beam shape parameters.

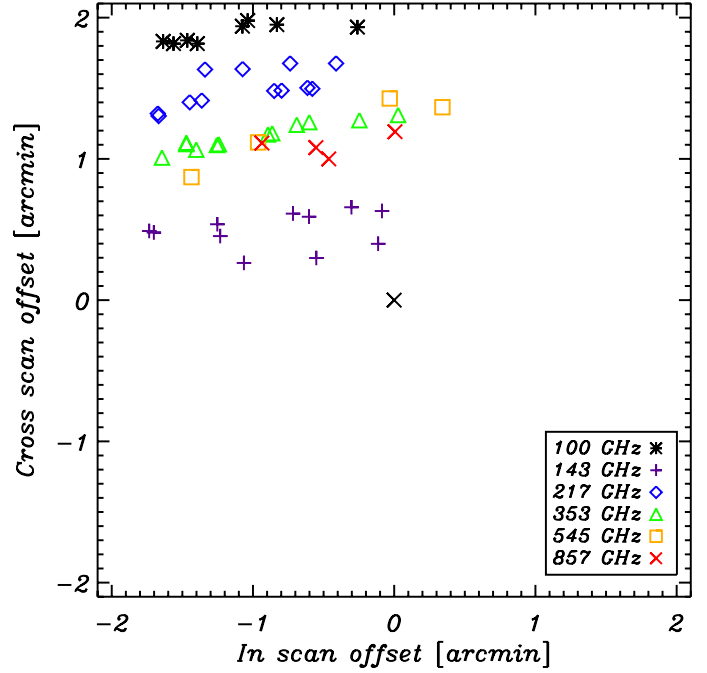
Table 3. Approximate dates and operational day (OD, counted since launch), of HFI observation of planets.

Planet	Date	OD
Mars	25/10/2009	165
Jupiter	28/10/2009	168
Neptune	03/11/2009	174
Uranus	08/12/2009	209
Saturn	05/01/2010	237
Mars	13/04/2010	335
Neptune	19/05/2010	371
Saturn	14/06/2010	397
Uranus	02/07/2010	415
Jupiter	05/07/2010	418

**Fig. 23.** Maps of Mars, for the 100-4a, 143-2a, 217-6b, 353-1, 545-2 and 857-1 detectors, along with the best-fit Gaussian beam. Note that the motion of Mars is taken into account. The stripes visible here are due to the spacing between successive rings, which is a significant fraction of the FWHM of the beam.

In Fig. 24 we show the individual detector positions with respect to the pre-launch Radio Frequency Flight Model (RFFM), in the scan direction (in-scan, horizontal) and perpendicular to it (cross-scan, vertical). We expect that some of the differences in the scan direction are due to residual phase shifts after the deconvolution of the time-stream filters (see Sect. 4 and Planck HFI Core Team 2011a). Although this makes it difficult to measure optical or mechanical differences in that direction, the measurement of these shifts and their incorporation into the pointing model enable us to completely account for that effect in subsequent analyses.

In fact, the pattern of individual detector shifts in Fig. 24 is a distorted and rotated image of the focal plane itself, indicating errors in the initial modelling. Using these data, and attempting to account for the per-detector phase shift introduced by transfer function deconvolution, we find an overall rotation of 0.15 degree and a scaling by a factor of 1.007 in both the in-scan and cross-scan directions. After such a scaling and rotation,

**Fig. 24.** Detector positions on the HFI focal plane for the first observation of Mars with respect to the input RFFM Model.

there is still a cross-scan rms scatter of 8 arcsec. As is evident from Fig. 24, these results require an overall rotation and scaling and are consistent with subsequent optical models of the *Planck* telescope.

To determine any systematic sources of error and to monitor possible time evolution of the detector positions, we show in Figs. 25 and 26 the residuals between different measurements of the focal plane. Figure 25 compares results from Mars transits in the first sky survey compared to the second. Figure 26 compares results from Saturn and Mars transits in the first survey. Comparison of the full set of planet observations yields an estimate of the remaining systematic error in the determination of the focal plane geometry to be approximately 20 arcsec cross-scan and 10 arcsec in-scan, considerably less than 10% of the beam FWHM in all cases.

The effect on astrophysical sources is shown in Fig. 1 of Planck Collaboration (2011), in which the locations of nearby galaxies as detected in the *Planck* Early Release Compact Source Catalogue (Planck Collaboration 2011c) are compared with measurements from IRAS. The rms difference, smaller than 1 arcmin, is dominated by confusion noise and pixelisation. We conclude that pointing errors are not significant for the HFI.

6.1.2. Scanning beams

In this section we discuss the measurement of HFI *scanning beams*, defined as the beam measured from the response to a point source of the full optical and electronic system, *after* the filtering described in Sect. 4 is applied. In the presence of low noise, perfect deconvolution, a perfect point source, full sampling and no filtering, this would be equivalent to the optical beam, i.e. the action of the telescope optics (mirrors and other optical elements) on the light path from infinity. We first concentrate upon the well-measured elliptical Gaussian parametrization. We compare the symmetrized Gaussian beam ($\sigma^2 = \sigma_1\sigma_2$ where σ_1, σ_2 are the major and minor beam widths) to the RFFM model as well as measurements of different planets. In Fig. 27

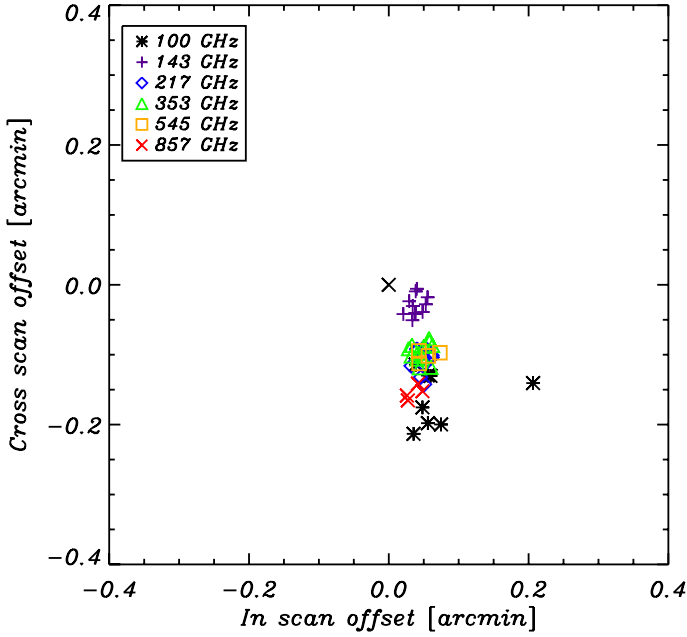


Fig. 25. Detector positions on the HFI focal plane for the second observation of Mars with respect to the first observation of Mars.

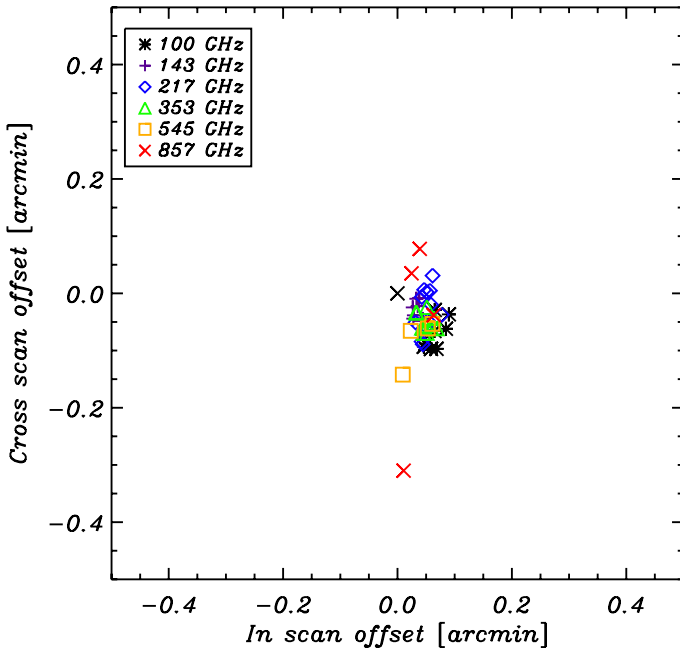


Fig. 26. Detector positions on the HFI focal plane for the first observation of Saturn with respect to the first observation of Mars.

we show measurements using Mars with respect to the model. Except for a subset of the 545 GHz detectors (which are highly non-Gaussian due to their multi-moded optics) the beams are typically narrower than the model. (The 857 GHz beams are also highly non-Gaussian, but happen to be better fit by a narrower beam). In Fig. 28 we compare the measurement of Mars with that of Saturn and in Fig. 29 we compare the measurements of Mars between the first and second surveys. These few-percent changes are consistent with variations in the sampling of the beam-shape between different observations and are comparable to the systematic errors resulting from small algorithmic differences (e.g., destriping). Finally, note that we expect that the fractional change in the size of Mars' disk due to the

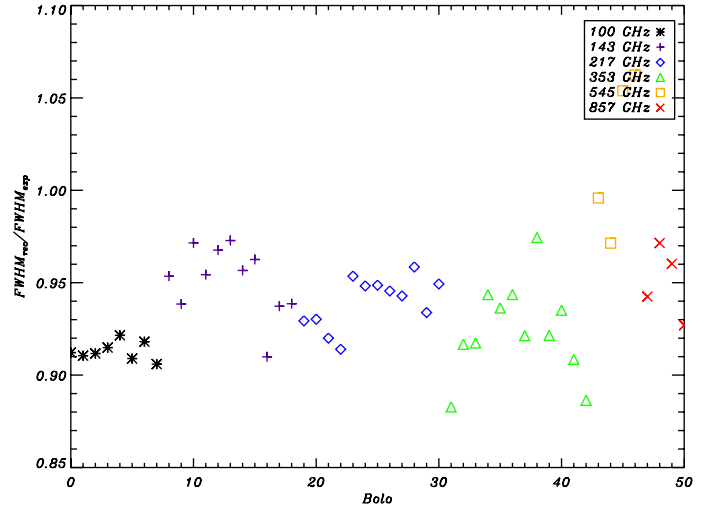


Fig. 27. The measured beam width (assuming a symmetrized Gaussian model) with respect to the RFFM model, for Mars.

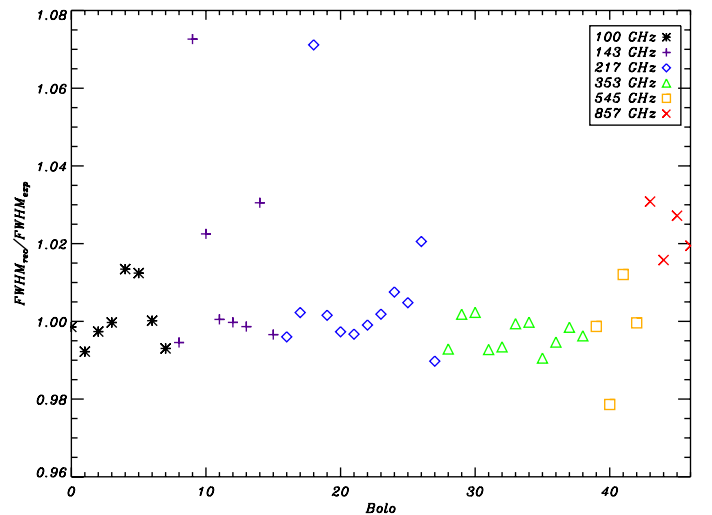


Fig. 28. The measured beam width (assuming a symmetrized Gaussian model) comparing the first scan of Saturn to the first scan of Mars.

variation in observation angle and distance is expected to be a far-subdominant value of 2×10^{-5} .

The more complex Gauss-Hermite model described in Appendix B allows us to take the full shape of the *Planck* beams into account. In particular a pure Gaussian fit typically misestimates the effective solid angle of the beam, and hence affects the flux calibration from known sources. The effect is greatest at 545 and 857 GHz, for which the Gaussian approximation typically underestimates the solid angle by 5%. At lower frequencies the effect is of order 1% when averaged over a frequency channel. In Fig. 30, we show the Gauss-Hermite fit for a number of detectors and the difference with an elliptical Gaussian fit. As expected, the effect of non-Gaussian beams is most significant for the two highest frequencies.

The statistical error on the FWHM of a channel-averaged beam is typically of order 0.05–0.15 arcmin. In practice, this is dominated by various systematic effects. For example, differences in the destriping method can give a 5–7% difference for a few detectors (but 1–2% is more typical). Other differences between analyses include pixelisation effects, the numerical likelihood maximization procedure, and the parametrization of the

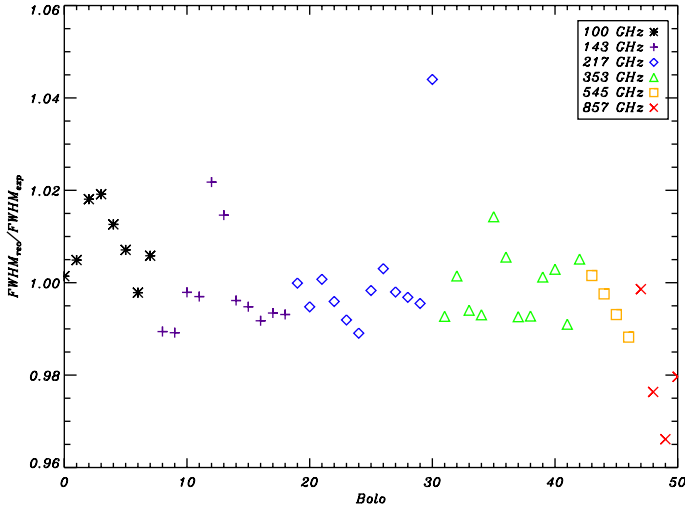


Fig. 29. The measured beam width (assuming a symmetrized Gaussian model) comparing the two observations of Mars.

beam-shape. Overall differences of a similar magnitude in the final solid angle result from the use of these alternate pipelines.

6.2. Effective beam per channel

Let us define the *effective beam* at the map level as the overall angular response to the sky in a map pixel, which results from the combined effect of the instrumental response, the scanning strategy and the data processing.

Scanning beams, described in the previous section, are an expression of our knowledge of the combined optical, electronic, and TOI processing induced response of each *Planck* detector to sky signals during the acquisition of each individual sample, that is during the ~ 5 ms period integration on the sky. Scanning beams are typically asymmetric, i.e. not fully rotationally symmetric around the pointing direction of a sample in the TOI.

The *Planck* scanning strategy is a combination of several rotations: satellite spin, slow (6 monthly period) precession of the spin axis around the anti-Solar direction in the L2 reference frame, and ecliptic motion of the anti-Solar axis of *Planck*. These combined motions result in a complicated pattern of pointing of each detector in the *Planck* focal plane. Over the course of the mission there is a build up of many observations in the areas near the ecliptic poles, while the broad band around the ecliptic equator is observed less frequently. In the vicinity of the ecliptic poles, the asymmetric scanning beams are pointed at the sky with very significant beam rotation, but the regions near the ecliptic plane see very reduced local scanning beam rotation.

Combination of all of the observations in a particular direction on the sky into a single pixel of a discretised sky map, results in the addition of all scanning beams viewing this particular region of the sky. We refer to the result of such addition as the effective beam.

We have developed two methods which can be used to estimate these effects, FICSBell (Hivon & Ponthieu, in prep.) and FEBeCoP (Mitra et al. 2011). The first method uses an approximate description of the scanning beam in harmonic space (retaining only the most relevant modes) while the second relies on an approximate description in pixel space (retaining only the pixels closest to the maximum). Both methods can be made precise to the desired level by increasing the computational cost. They are further described in the Appendix D. Both methods

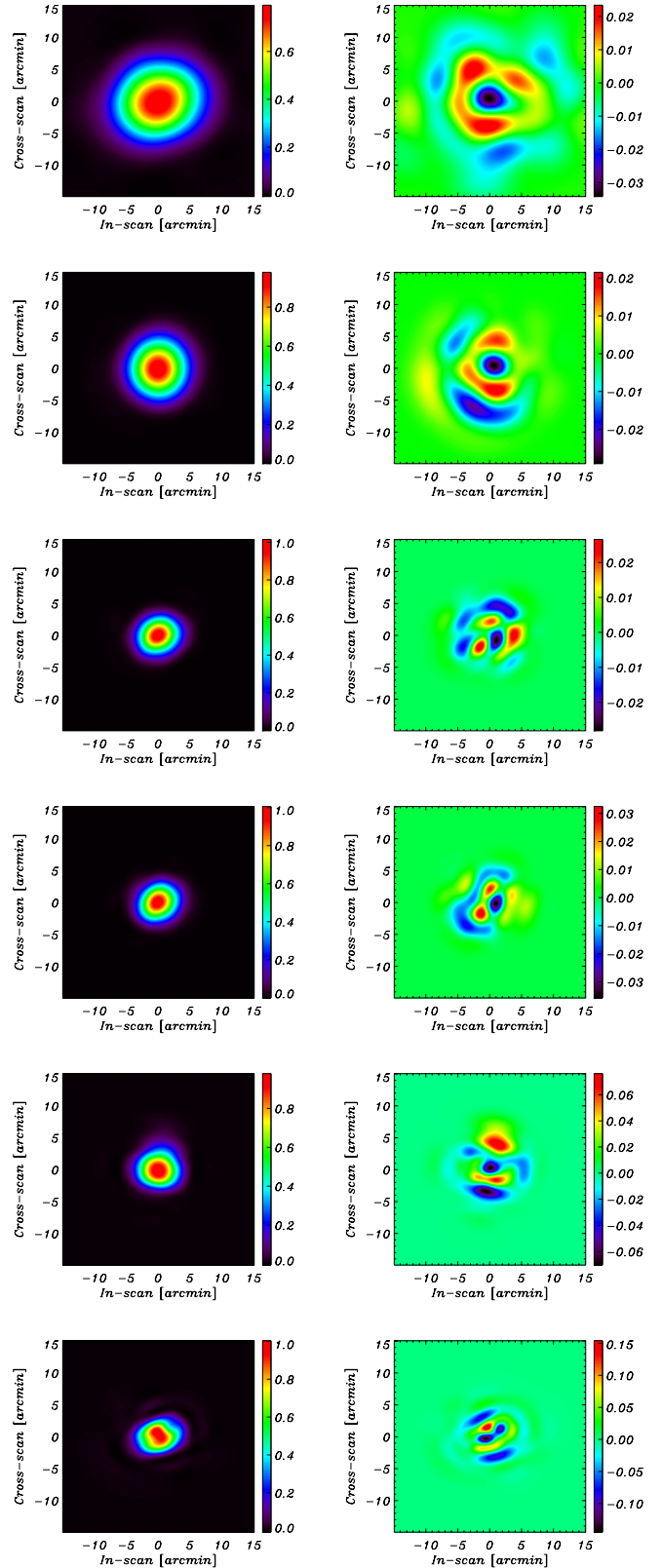


Fig. 30. Left Column: full Gauss-Hermite fit to the detector scanning beam, for 100-1a, 143-1a, 217-1, 353-1, 545-1 and 857-1, from top to bottom. Right Column: difference with an elliptical Gaussian fit.

show that the differences between the scanning beams and the effective beam are small, at the few percent level. The Fig. D.3 in the appendix shows a dispersion of few percent in the FWHM

and ellipticity around the sky and the mean characteristics are given in lines c1–c4 of the summary table, Table 4 (Sect. 9).

Both of these beams have been used in our paper on the power spectrum of CIB anisotropies with *Planck*-HFI (Planck Collaboration 2011n). FEBECOP was also used to estimate corrections to the derived flux of sources in the *Planck* ERCSC. One should note that the ERCSC production was done shortly after maps had been produced by the DPCs and used the best information on the scanning beams available at that time. This paper provides the best information available at the time of writing, i.e. a few months later, but is compatible with the characteristics described in the ERCSC paper and explanatory supplement (Planck Collaboration 2011c,v).

Observations of the outer planets suggest the presence of potentially significant shoulders in the sub-mm beams, as would result from the diffuse scattering from random surface errors of order $5\text{--}8\ \mu\text{m}$ on scales between 10 and 100 mm. Surface errors at this level are consistent with the estimates in Table 2 of Stute (2004), and meet the design specifications. The beam shoulder, which is typically evident at the -40 dB level, is not described by either the Gaussian or Gauss-Hermite expressions of the main beam. The integrated throughput of this shoulder constitutes less than 0.5% of the total solid angle of the scanning beam at frequencies below 353 GHz. However the contribution to the sub-mm channels is larger, with current estimates of 1.7, 4.8 and 7.2% of the total solid angle (as reported in Table 4, note b1) at 353, 545 and 857 GHz, respectively. Beam solid angles derived exclusively from the main beam will correspondingly under-estimate the true instrumental solid angle. Therefore, flux estimates of point sources will generally be under-estimated by a comparable amount. We note that aperture photometry of sources with a signal-to-noise ratio less than about 40 dB will suffer similarly from this bias.

6.3. Beam uncertainties

We now turn to the effect of uncertainties in the scanning beams on the knowledge of ERCSC point sources. An approximate estimate is obtained by comparing simulations using the Gaussian elliptical and the Gauss-Hermite description of the beams. In both cases, point-sources were detected in the simulated 857-GHz map using a Mexican-hat wavelet filter algorithm. Outside the Galactic plane ($|b| > 20^\circ$), 93.5% of input sources were detected using both beam models. Within the plane, this figure was 84.3%. We estimated point source fluxes by performing aperture photometry for the set of detected input sources with Galactic latitude $|b| > 20^\circ$.

Figure 31 shows the histogram of the ratio of aperture fluxes for the two beam models. The black curve shows the distribution from a point source only simulation, including only the beam difference of the point source signal. The red curve shows the distribution from a point source and diffuse component simulation, including point source signal differences and differences in the background subtraction due to the beam. From the latter we estimate an upper limit on aperture flux errors due to beam uncertainties of 0.5% at 143 GHz and 1.6% at 857 GHz. This confirms that flux error due to beam uncertainties are much smaller than the flux error due to source detection errors.

For both simulations, the known input source centre was used for the aperture photometry. By design this ignores the effect of source detection errors (for example, mis-estimation of the centres).

We also computed the median absolute deviation of the flux error due to detection errors as a function of absolute Galactic

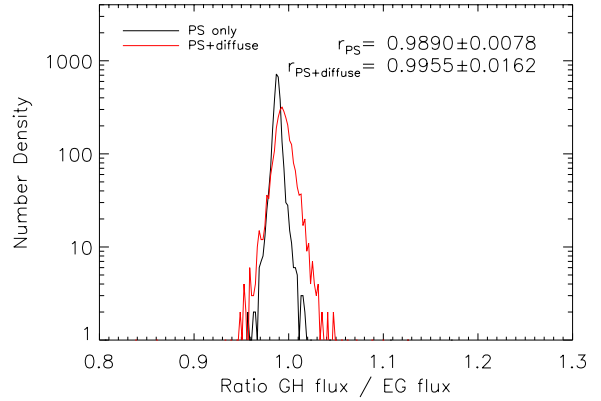


Fig. 31. Histograms of the ratio of aperture fluxes from 857 GHz simulations with elliptical Gaussian and Gauss-Hermite beams. The quoted values of r are the mean \pm the root-mean-square of the ratio across the source sample.

latitude and found that it varies from 10–15% in the Galactic plane to a few per cent at $b > 40$ deg.

7. Map making and photometric calibration

The path from TOIs to maps follows two steps, ring-making and map-making. The first step makes use of the redundancy of observations provided by the *Planck* spacecraft scanning strategy.

As discussed in Sect. 5, the in-flight noise of the HFI detectors after TOI processing is mostly white with a “ $1/f$ ” component at low frequency (see Sect. 5 and Planck HFI Core Team 2011a). To build sky maps and further reduce the low-frequency noise, we adopted a destriping approach in which the $1/f$ component, is represented by a uniform offset on a scan ring. Using one offset per ring, residuals of $1/f$ noise found in the cleaned map have been shown to be significantly below the white noise level in the map domain.

For a given channel, each measurement at the sample number i may be described as :

$$m_i = G \left(I_p + \frac{1-\eta}{1+\eta} (Q_p \cos 2\psi_i + U_p \sin 2\psi_i) \right) + n_i \quad (4)$$

where p denotes the sky pixel with Stokes parameters I , Q and U ; n_i is the noise realization; η is the cross-polarization parameter (equal to 1 for an ideal SWB and 0 for an ideal PSB); ψ is the detector orientation; and G is the detector’s gain.

Calibrating the detectors on an unpolarised source (with $Q = U = 0$), e.g., the orbital dipole, determines G . The photometric calibration is performed either at ring level using the Solar dipole, for the lower frequencies channels (see Sect. 7.4.1) or at map level using FIRAS data, for the channels at 545 and 857 GHz (see Sect. 7.4.2). The polarization response parameters (detectors orientations and cross-polarisation) have been extracted from ground measurements as described in Rosset et al. (2010).

7.1. Ring making

As an intermediate product, we average circles within a pointing period to make rings with higher signal-to-noise ratio. To avoid introducing any additional binning of the data, we choose a sky pixelisation as a basis for this ring making. We used the

HEALPix scheme (Górski et al. 2005) with $N_{\text{side}} = 2048$, corresponding to pixels with 1.7 arcmin on a side. Data are averaged in each scanned HEALPix pixel using the nearest grid point method. The resulting collection of HEALPix pixels visited during a pointing period is hereafter called a HEALPix Ring or HPR.

From the pointing direction and the satellite velocity at the time of each sample, the component of the calculated orbital dipole signal is averaged as described above and used for calibration. Once data are calibrated, it is subtracted before projection.

The orientations of the detectors are propagated using the averaged sine and cosine values (Eq. (4)) for the samples falling in each pixel of the HPR. Because of the low level of nutation of the satellite, the dispersion of the relative orientation within each bin is very low leading to a negligible error in the averaged orientation.

Samples flagged by the TOI processing pipeline as invalid, observations outside of the stable pointing periods, and those near known moving objects (planets, asteroids and comets) are removed from further analysis.

7.2. Destriping

Destriping algorithms simplify the map making problem and require substantially fewer computational resources than those for a full maximum likelihood solution. They are very close to optimal when certain conditions are satisfied (see, for example, Delabrouille 1998; Revenu et al. 2000; Maino et al. 2002; Keihänen et al. 2004; Ashdown et al. 2007)

In the destriping approach, the noise is divided into a low-frequency component represented by the offsets \mathbf{o} , unfolded onto the time-ordered data by the matrix $\mathbf{\Gamma}$, and a white noise part \mathbf{n} which is uncorrelated with the low-frequency noise. The signal part in the TOI is given by the projection of a pixelised sky map (or set of maps containing the 3 Stokes parameters, arranged as a single vector), \mathbf{T} via a pointing matrix, \mathbf{A} , leading to

$$\mathbf{d} = \mathbf{A} \cdot \mathbf{T} + \mathbf{\Gamma} \cdot \mathbf{o} + \mathbf{n}. \quad (5)$$

The maximum-likelihood offset coefficients, \mathbf{o} , can be found from the time-ordered data, \mathbf{d} , by solving

$$(\mathbf{\Gamma}^T \mathbf{N}^{-1} \mathbf{Z} \mathbf{\Gamma}) \cdot \mathbf{o} = \mathbf{\Gamma}^T \mathbf{N}^{-1} \mathbf{Z} \cdot \mathbf{d}, \quad (6)$$

where

$$\mathbf{Z} = \mathbf{I} - \mathbf{A} (\mathbf{A}^T \mathbf{N}^{-1} \mathbf{A})^{-1} \cdot \mathbf{A}^T \mathbf{N}^{-1}. \quad (7)$$

The HFI destriper module, `polkapix`, determines offsets (one offset per ring) from a set of input HPR. The algorithm is based on underlying reference (HEALPix) pixelisations of the I , Q and U sky signals. These underlying sky maps may have different resolutions for the temperature and polarization parts. To generate the temperature maps for the early analyses, only the temperature signal has been used to compute offsets, i.e. polarization effects have been neglected. We chose an intermediate resolution of $N_{\text{side}} = 128$ to increase the signal to noise ratio without correlating the offsets of too many neighbouring rings. At this resolution, it was necessary to mask the inner part of the Galaxy where the gradients in the sky signal are strong. The mask used is based on a Galactic cut at 7 MJy sr^{-1} on the IRAS $100 \mu\text{m}$ map (removing approximately 19% of the sky) and additionally includes some bright sources (see Fig. 32).

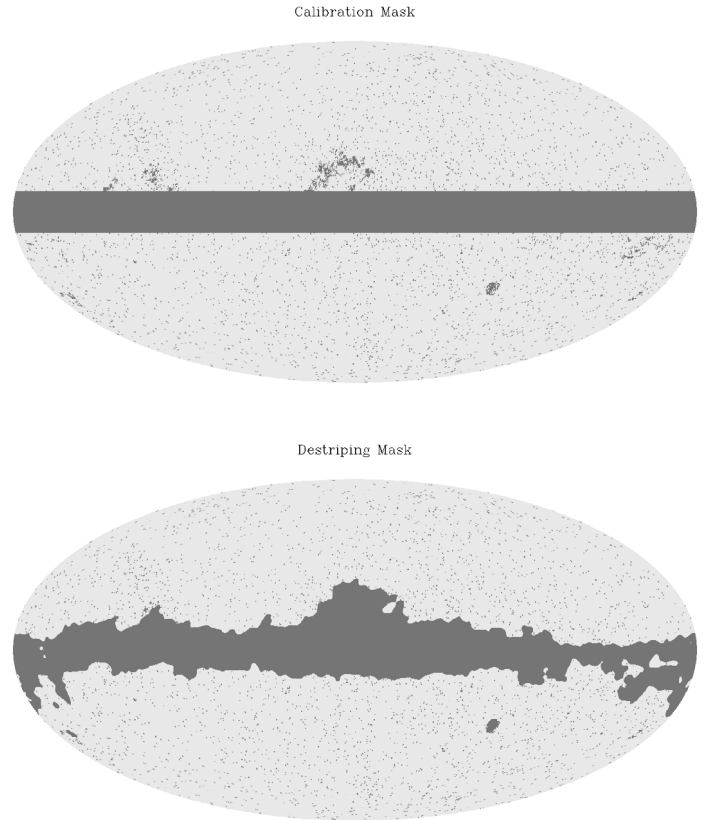


Fig. 32. Masks used for dipole calibration (*top*) and destriping (*bottom*). The former is less extended since the calibration methods include a Galactic template based on the *Planck* Sky Model.

7.3. Map projection

Cleaned maps are produced using a simple co-addition of the HEALPix Rings but taking into account the offsets estimated by the destriper module. Maps are produced for each detector independently and per frequency (combining all detectors of the same frequency channel). Polarization maps are also constructed for polarization sensitive channels, i.e. for frequencies up to 353 GHz. We account for the different noise level in the combined maps, weighting data from each detector using their NEP, as determined by the noise estimation pipeline (cf. Sect. 5). In each case, hit count maps are also produced (shown in Fig. 33), as well as maps of the 3×3 covariance matrix of I , Q and U in each pixel. Note that the ERCSC and the *Planck* early results papers are based on temperature maps only, even though polarization maps have been produced by the pipeline.

For jackknife tests and noise evaluation studies we produced several other maps by using various subsets of data including:

- two independent sets of detectors per frequency (so-called “half-focal plane” maps);
- separate sky surveys (so-called “survey” maps, based on six months of data);
- independent ring sets built using the first and second half of the stable pointing periods (so-called “half-ring” maps).

The last set of maps can be used to estimate accurately the high frequency noise (on time-scales less than the half-ring duration, i.e. about 20 min) in the rings, as well as in the maps.

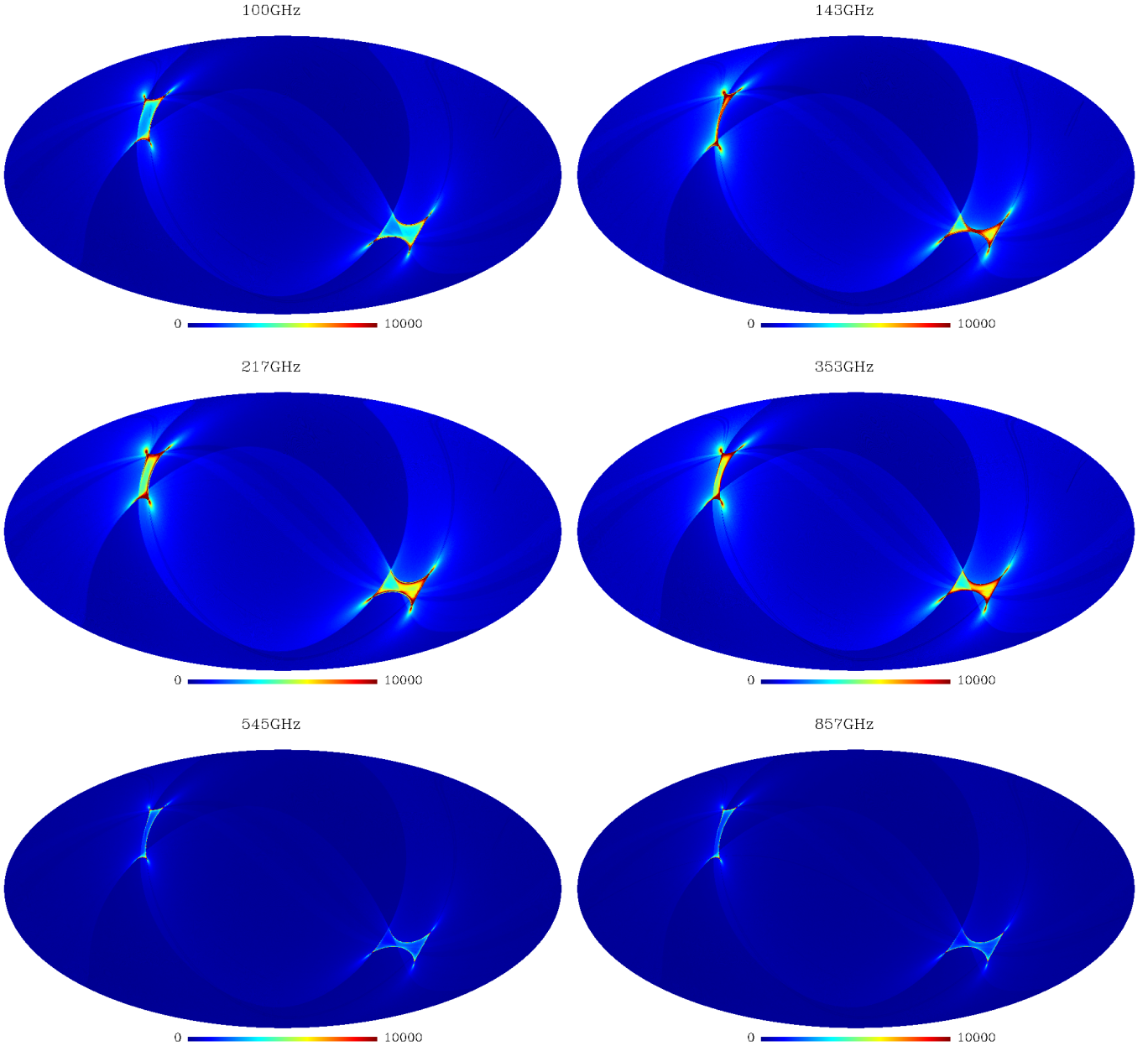


Fig. 33. Hit count maps at each frequency (from top left to bottom right: 100, 143, 217, 353, 545, 857 GHz) in 1.7 arcmin pixels ($N_{\text{side}} = 2048$).

Maps were also produced with `SPRINGTIDE` (Ashdown et al. 2007) and `MADAM` (Keihänen et al. 2005) and lead to consistent results.

7.4. Absolute photometric calibration

The primary absolute calibration of the *Planck* HFI instrument is based on extended sources. At low frequencies (353 GHz and below), the orbital dipole and the Solar dipole provide good absolute calibrators. At high frequencies (545 GHz and above), Galactic emission is used. The best available data, in term of spectral coverage and absolute calibration accuracy, are the COBE/FIRAS spectra. We used these data as an absolute photometric calibrator for the 857 and 545 GHz channels. Both calibration techniques (dipoles and Galactic emission) have been applied at intermediate frequencies (353 and 545 GHz) for

consistency checks. FIRAS data are also used at all frequencies to set the zero level in the HFI maps.

7.4.1. Absolute photometric calibration using the Solar dipole

Since we need to account for the orbital dipole, the dipole calibration is done at the ring level rather than the map level. The Solar dipole has been accurately measured by WMAP (Hinshaw et al. 2009). Gains are determined for each stable pointing period through a χ^2 minimization. Each input sample is modelled as:

$$m = g_d I_D + g_g T_g + C + \text{noise}, \quad (8)$$

where g_d is the gain, I_D is the dipole signal (including both Solar and orbital dipoles), C is a constant allowing for an offset. The Galactic signal is modelled using a template T_g derived

from the thermal dust maps in the Planck Sky Model (PSM, version 1.6.3) at each central frequency smoothed to match the detector beam. For each ring we fit for the gain and the coefficient of the Galactic template g_g and the constant C .

For calibration purposes, bright sources (detected by HFI or already known a priori) are masked and we use a Galactic latitude cut ($b < 9^\circ$) to avoid using the central part of the Galactic plane, where the model used by the PSM (from Finkbeiner et al. 1999) is not sufficiently accurate. The upper plot in Fig. 32 shows the actual mask used for calibration.

The main limitation of this approach is the contamination by Galactic foregrounds, especially their polarised component which is poorly known. This preferentially affects those rings where, because of the orientation of the spin axis, the amplitude of the dipole is small compared to the Galactic signal.

An average over time of the gains estimated on the dipole is used for the photometric calibration of each detector at frequencies of 353 GHz or less. We have restricted this computation to a time interval of the first survey, corresponding to rings 2000 to 6000, where the gain measurements appear less affected by systematic effects. On this interval, the rms of the ring-by-ring gains is of the order of 1%, or less, for frequencies up to 353 GHz. The same procedure applied to the second survey gives comparable results, except for a few bolometers that shows a yearly variation of less than 2%.

Note that the photometric calibration has to be done prior to the destripping so that the orbital dipole can be subtracted.

7.4.2. Absolute photometric calibration using FIRAS data: calibration factors and zero points

The scheme used for the photometric calibration of the *Planck* HFI on FIRAS data is very similar to that adopted by the Archeops collaboration (Macías-Pérez et al. 2007). For calibration of the *Planck* HFI, FIRAS data was processed as follows:

- conversion of the data from their original COBE quad-cube pixelisation to the HEALPix scheme by using a drizzling re-projection code (Paradis, in prep.);
- extrapolation of the data to obtain brightnesses at the nominal HFI frequencies. The FIRAS map at one selected frequency can be obtained by convolving the FIRAS spectra with the HFI bandpass filters. However, this method produces very noisy FIRAS maps at high Galactic latitude (especially for $\lambda > 700\mu\text{m}$). Since we are interested in both the Galactic plane and its surrounding, we have preferred to derive the FIRAS maps together with their errors using fits of FIRAS spectra. Each individual FIRAS spectrum is fitted with a black body, modified by a ν^β emissivity law. Since we are searching for the best representation of the data and not for physical dust parameters, we neglect the contribution of the cosmic infrared background. We moreover restrict the fit to the frequency range of interest, avoiding the need for a second dust component as in Finkbeiner et al. (1999).

The results of this processing consist of $N_{\text{side}} = 16$ HEALPix maps for the sky signal extrapolated from FIRAS data for each HFI detector, together with associated errors.

The HFI data have to be convolved by the FIRAS beam. This beam has been measured on the Moon. Due to imperfections in the sky horn antenna, the effective beam shows both radial and azimuthal deviations from the nominal 7° top hat beam profile. Since COBE rotates about the optical axis of the FIRAS instrument, on average, the beam must have cylindrical symmetry.

However, the time it takes to collect a single interferogram is less than a rotation period. Thus, a particular measurement beam may be asymmetric. Fixsen et al. (1997) estimate that the assumption of beam symmetry may produce residual beam shape errors of order of 5%, that are not taken into account in this analysis. We perform the beam convolution in HEALPix format. To simulate the movement during an integration of an interferogram, the HFI data were further convolved by a 2.6° top-hat in the direction perpendicular to the ecliptic plane (which is roughly the FIRAS scanning direction).

Following the IRAS convention, the spectral intensity data, I_ν , are expressed in MJy/sr at fixed nominal frequencies, assuming the source spectrum is $\nu I_\nu = \text{constant}$ (i.e. constant intensity per logarithmic frequency interval). Since the source spectrum is not a constant intensity per logarithmic frequency interval, a colour correction has to be applied to obtain an accurate intensity. The colour correction factor cc is defined such that:

$$I_{\nu_0}(\text{actual}) = I_{\nu_0}(\text{quoted})/cc, \quad (9)$$

where $I_{\nu_0}(\text{actual})$ is the actual specific intensity of the sky at frequency ν_0 , $I_{\nu_0}(\text{quoted})$ is the corresponding value given with the IRAS convention, and ν_0 is the frequency corresponding to the nominal wavelength of the considered band. With these definitions:

$$cc = \frac{\int (I_\nu/I_{\nu_0})_{\text{actual}} R_\nu d\nu}{\int (\nu_0/\nu) R_\nu d\nu}, \quad (10)$$

where $(I_\nu/I_{\nu_0})_{\text{actual}}$ is the actual specific intensity of the sky normalised to the intensity at frequency ν_0 and R_ν is the spectral response. We derive the colour correction for each FIRAS pixel using the HFI bandpass filters and the fits of FIRAS spectra.

Gains and zero levels are obtained for each detector by fitting:

$$I_{\text{FIRAS}}(\nu_0) \times cc = K \times I_{\text{HFI}}(7 \text{ deg beam}) + zp, \quad (11)$$

where K is the calibration factor for the two high-frequency channels and zp is the zero level value (I stands for the intensity). However, the fit is done for each detector, even for the low frequency channels, to set the zero levels of our maps.

In these low-frequency channels, we needed to add the CMB anisotropies to the FIRAS maps (or we could have removed them from the HFI data) in order for Eq. (11) to be valid. Currently, we are adding the WMAP CMB map (convolved by the FIRAS beam). But we also have to deal with the fact that there is a substantial contribution in some wavebands from CO lines (cf. Sect. 9.4). The FIRAS dataset we are using does not contain the lines (but the CO(1–0) is not detected in FIRAS). At this stage, we simply reduce the fit to the regions outside a CO mask derived from the Dame et al. (2001) survey, in order to minimize the contamination of the *Planck* 217 and 100 GHz channels before computing the zero levels.

Because of its high signal-to-noise ratio, the Galactic plane is the best place to perform the calibration of the HFI high-frequency data. Unfortunately, there are two problems that limit

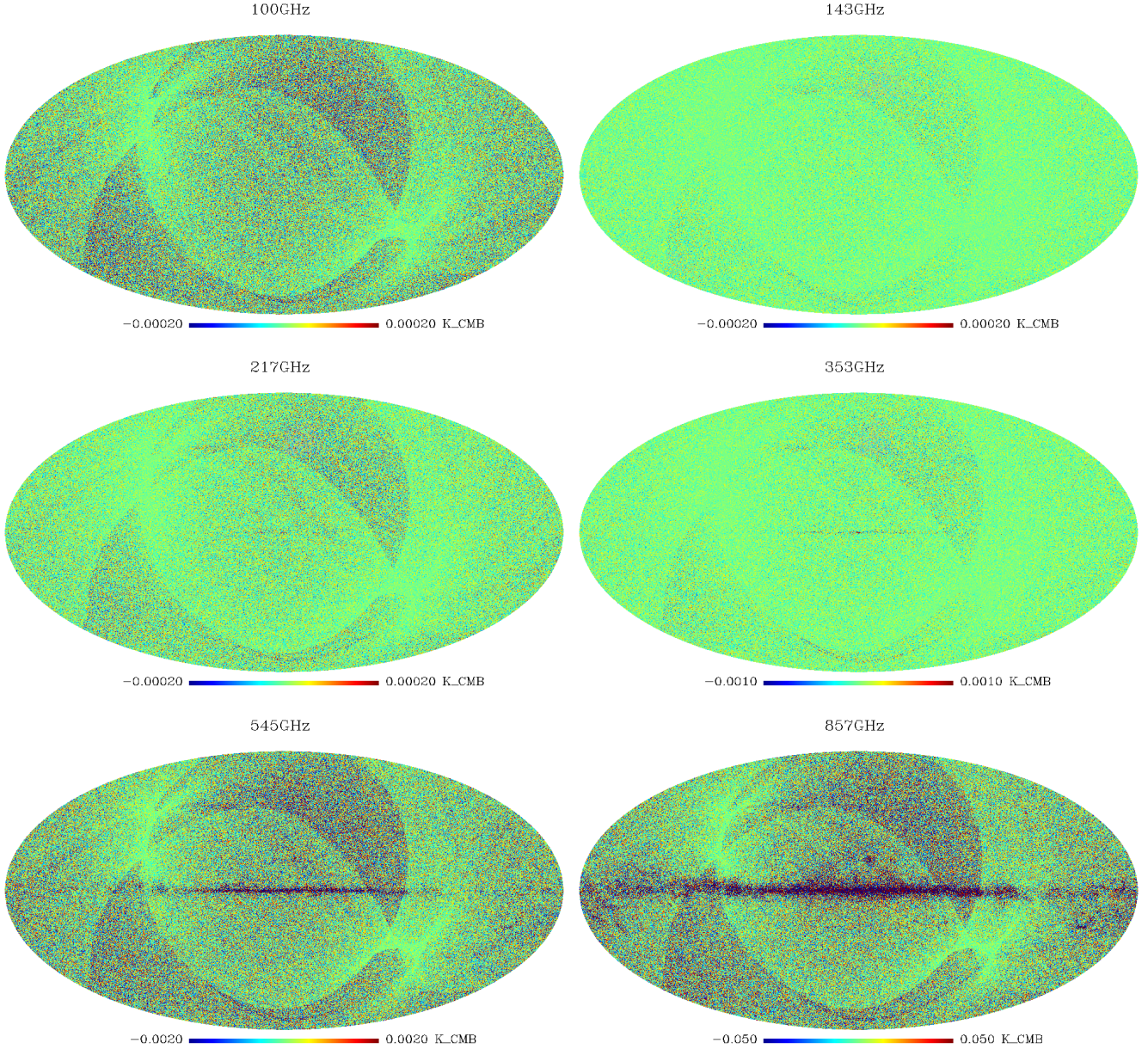


Fig. 34. Residual maps of the half differences between the maps made from the first and second half ring projection (*from top left to bottom right*: 100, 143, 217, 353, 545, 857 GHz) in 1.7 arcmin pixels ($N_{\text{side}} = 2048$). Note that the CMB channels at 100–217 GHz are all shown on the same color scale. In addition to the noise pattern, which is well traced by the hit maps of Fig. 33, one also sees small differences relative to the signal, when gradients of the signal are large (mostly in the Galactic plane) and sub-pixel effects become quite apparent.

the accuracy in the Galactic plane: (1) the lack of precise knowledge of the FIRAS beam; (2) The fact that the colour corrections are applied at the 7° resolution, whereas they should be applied to each HFI pixel prior to the convolution with the FIRAS beam. We thus applied Eq. (11) to bands slightly above the Galactic plane, i.e. for Galactic latitudes, $10^\circ < |b| < 60^\circ$, at latitudes low enough to have a reasonable signal to noise ratio. The fit is done on one averaged Galactic-latitude profile (i.e. one profile averaged over all longitudes).

Errors on K and z_p take into account only statistical errors on the FIRAS data. There are mostly the same for K and z_p and are about 0.4%, 0.8%, 2.5%, 5%, 15% and 20% at 857, 545, 353, 217, 143 and 100 GHz, respectively. However, the systematic errors are larger than the statistical errors at high frequencies. They have been estimated using the dispersion of the fitted values in

different parts of the sky. They are about 7% for K at all frequencies and about 2% for z_p (for 857, 545 and 353 GHz).

Because of: (i) the poor signal-to-noise of FIRAS data at low frequency, and thus uncertainties in the FIRAS spectra fits; (ii) the fact that we need to avoid bright regions with CO; (iii) the fact that we are calibrating outside the Galactic plane (due to FIRAS beam uncertainties), we compare the dipole/Galaxy calibration only at 353 GHz and 545 GHz. We find agreement within 2–3% at 545 GHz, and within 5–6% at 353 GHz.

7.5. Relative photometric calibration accuracy between channels

We evaluated the photometric calibration relative accuracy between frequency channels up to 353 GHz using several methods.

In the first, we compare maps in CMB dominated sky areas. The first step is to mask areas possibly contaminated by Galactic emission or point sources. We used a stringent mask, keeping only $\sim 6\%$ of the sky, which we obtained by setting a threshold on the 857 GHz intensity as measured by HFI, combined with a point source mask built using the HFI catalogue produced by the HFI pipeline (see the description in Sect. 8.1). We then smoothed the frequency maps to equivalent Gaussian FWHM of 1° . The scatter plot of the unmasked pixel values from each map is then fitted to a straight line. The slope of this line should be unity, as we calibrated both maps in K_{CMB} and selected sky areas where CMB dominates. The residual deviations from unity are below 1% for the 100–143 and 143–217 GHz and about 4% for 217–353 GHz comparison, where foregrounds are more important even in the small unmasked area that we used. The same method, applied to compare the HFI 100 GHz and the LFI 70 GHz maps, shows that their calibrations agree to within 0.5%.

In the second method, we used a spectral-matching technique which jointly fits all the spectra and cross-spectra of all HFI channels (Delabrouille et al. 2003; Cardoso et al. 2008), except the 857 GHz channel (actually, that channel is regressed out of the 5 lowest frequency channels before fitting). These auto- and cross-spectra are fitted via maximum likelihood to a model including contributions from the CMB, from foregrounds and from noise. The calibration coefficients are treated as additional parameters in the fits. Since the model includes a component capturing foreground emission, a relatively large fraction of the sky can be used to estimate the spectra: we used a mask excluding about 40% of the sky, based on the emission at 857 GHz and on the ERCSC and ESZ catalogues. The consistency of the estimates of the relative calibration coefficients was checked using jackknives: we compared the estimates obtained using the whole masked sky or only the northern or southern part of the sky. We also compared the estimates using the first or last part of the rings. In all cases, the discrepancy between all estimates was found to be well under 1%. Their mean value was found to agree with the photometric calibration to better than 1% for the 100, 143, 217 and 353 GHz channels. All those measurements were obtained by fitting the spectra over the multipole range $100 \leq \ell \leq 900$. The robustness of the results against the choice of multipole range was also investigated. Fits performed over the sub-ranges [100, 600], [200, 700], [300, 800], [400, 900] showed variations of the calibration coefficients of the order of half a percent.

Finally, we also computed the relative calibration of HFI channels using the CMB map (Delabrouille et al. 2009) derived by applying to the WMAP 5 year data the needlet ILC method described later in Sect. 8.3. This was done on a selected range in ℓ , with a smooth rise of the spectral window between $\ell = 15$ and $\ell = 50$, and a cut at high ℓ set by the signal to noise ratio of the CMB map derived from WMAP5. Different sets of masks based on ancillary data (H_α from Finkbeiner et al. (1999), 408 MHz from Haslam et al. (1982), $100 \mu\text{m}$ from Schlegel et al. (1998), or from our own 857 GHz map and *Planck* ERCSC sources) were used to perform the calibration. The relative calibration factors were then computed relative to our most sensitive 143 GHz channel for masks retaining different fractions of the sky (from 30 to 70%), and for maps produced with different detector sets, or based on halves of the ring data, or different hemispheres. The dispersion found (relative to the 143 GHz channel) was below about 1% for the 100 and 217 GHz channels, and about 2% for the 353 GHz channel.

These three lines of investigation therefore consistently provide an estimate better than 1% for the relative calibration

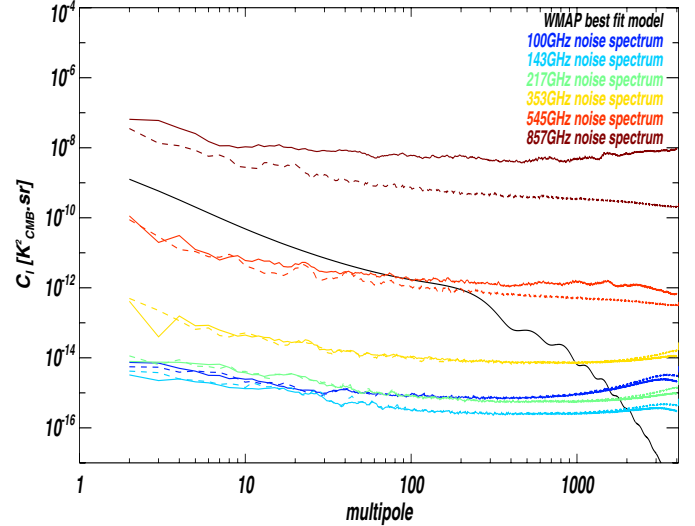


Fig. 35. Power spectra from the difference maps shown in Fig. 34, on the full sky (*solid line*) and after masking the Galactic plane (*dashed line*). The sky coverage correction was done according to Tristram et al. (2005). As expected, the difference is only substantial at high frequency, when gradients of the Galactic signal are large.

accuracy between the 100, 143, and 217 GHz channels. For the 353 GHz channel, we estimate the accuracy to be better than about 2%, on the basis of the two latter methods.

7.6. Jackknife tests and noise properties

An important characteristic of maps is obtained by analysing the “half-ring” maps. For each frequency, we constructed the half-difference between these two independent sets of half-rings maps; they are shown in Fig. 34. As a result of the *Planck* scanning strategy, the noise in these maps is inhomogeneous; it is largely dominated by white noise modulated by the hit count in each pixel, as can be seen from the hit maps shown in Figs. 34. In the high frequency difference maps (545 and 857 GHz), we also observe some additional residuals in the Galactic plane, where the gradients of the sky signal within the pixels are strong. This can be understood by noting the poor sampling of those pixels, together with that of the beam FWHM for these channels; this should be significantly reduced once more data is included.

In the harmonic domain (Fig. 35), the power spectra of these difference maps are almost flat over a wide range of multipoles. The effect of the time constant deconvolution is roughly compensated by the low-pass filtering resulting in a relatively small deviation from pure flat white noise at high multipoles ($\ell \sim 3000$). The average level between $\ell = 100$ and $\ell = 1000$ of these power spectra in the masked case provides an estimate of the white part of the noise in the maps which is given in line a3 of the summary table, Table 4. These levels are consistent with those obtained in clean region of the sky in the study of the cosmic infrared background fluctuations (Planck Collaboration 2011n).

8. CMB removal

This section was developed in common with LFI (Zacchei et al. 2011) and is reported identically in both papers.

In order to facilitate foreground studies with the frequency maps, a set of maps was constructed with an estimate of the CMB contribution subtracted from them. The steps undertaken

in determining that estimate of the CMB map, subtracting it from the frequency maps, and characterising the errors in the subtraction are described below.

8.1. Masks

Point source masks were constructed from the source catalogues produced by the HFI pipeline for each of the HFI frequency channel maps. The algorithm used in the pipeline to detect the sources was a Mexican-hat wavelet filter. All sources detected with a signal-to-noise ratio greater than 5 were masked with a cut of radius $3\sigma \approx 1.27$ FWHM of the effective beam. A similar process was applied to the LFI frequency maps (Zacchei et al. 2011).

Galactic masks were constructed from the 30 GHz and 353 GHz frequency channel maps. An estimate of the CMB was subtracted from the maps in order not to bias the construction. The maps were smoothed to a common resolution of 5° . The pixels within each mask were chosen to be those with values above a threshold value. The threshold values were chosen to produce masks with the desired fraction of the sky remaining. The point source and Galactic masks were provided as additional inputs to the component separation algorithms.

8.2. Selection of the CMB template

Six component separation or foreground removal algorithms were applied to the HFI and LFI frequency channel maps to produce CMB maps. They are, in alphabetical order:

- AltICA: internal linear combination (ILC) in the map domain;
- CCA: Bayesian component separation in the map domain;
- FastMEM: Bayesian component separation in the harmonic domain;
- Needlet ILC: ILC in the needlet (wavelet) domain;
- SEVEM: template fitting in map or wavelet domain;
- Wi-fit: template fitting in wavelet domain.

Details of these methods may be found in Leach et al. (2008). These six algorithms make different assumptions about the data, and may use different combinations of frequency channels used as input. Comparing results from these methods (see Fig. 39) demonstrated the consistency of the CMB template and provided an estimate of the uncertainties in the reconstruction. A detailed comparison of the output of these methods, largely based on the CMB angular power spectrum, was used to select the CMB template that was removed from the frequency channel maps. The comparison was quantified using a jackknife procedure: each algorithm was applied to two additional sets of frequency maps made from the first half and second half of each pointing period. A residual map consisting of half the difference between the two reconstructed CMB maps was taken to be indicative of the noise level in the reconstruction from the full data set. The Needlet ILC (NILC) map was chosen as the CMB template because it had the lowest noise level at small scales.

The CMB template was removed from the frequency channel maps after application of a filter in the spherical harmonic domain. The filter has a transfer function made of two factors. The first corresponds to the Gaussian beam of the channel to be cleaned; the second is a transfer function attenuating the multipoles of the CMB template that have low signal-to-noise ratio. It is designed in Wiener-like fashion, being close to unity up to multipoles around $\ell = 1000$, then dropping smoothly to zero

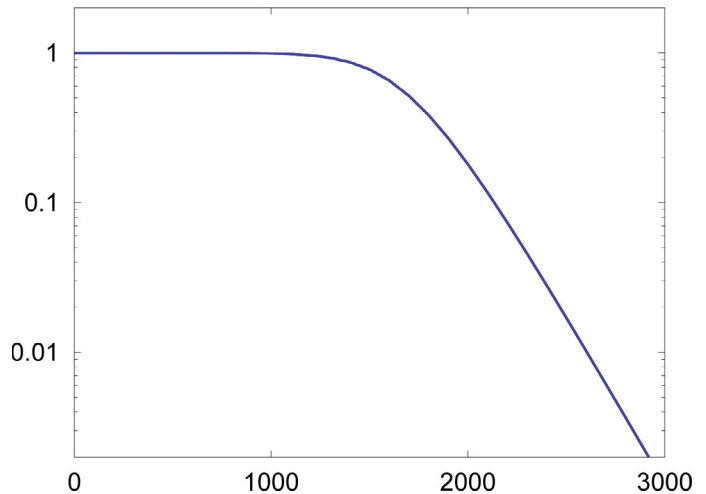


Fig. 36. Wiener-like filter function, plotted versus multipole, which was applied to produce the template for CMB removal.

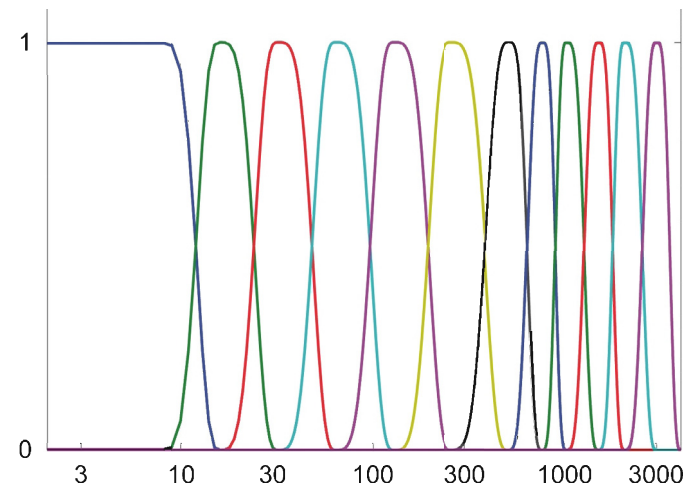


Fig. 37. The bandpass filters, plotted versus multipole, that define the spectral domains used in the NILC.

with a cut-off frequency around $\ell = 1700$ (see Fig. 36). All angular frequencies above $\ell = 3900$ are completely suppressed. This procedure was adopted to avoid doing more harm than good to the small scales of the frequency channel maps where the signal-to-noise ratio of the CMB is low.

8.3. Description of needlet ILC

The NILC map was produced using the ILC method in the “needlet” domain. Needlets are spherical wavelets that allow localisation both in multipole and sky direction. The input maps are decomposed into twelve overlapping multipole domains (called “scales”), using the bandpass filters shown in Fig. 37 and further decomposed into regions of the sky. Independent ILCs are applied in each sky region at each needlet scale. Large regions are used at large scales, while smaller regions are used at fine scales.

The NILC template was produced from all six HFI channels, using the tight Galactic mask shown in Fig. 38, which covers 99.36% of the sky. Additional areas are excluded on a per-channel basis to mask point sources. Future inclusion of the LFI channels will improve cleaning of low-frequency foregrounds such as synchrotron emission from the CMB template.

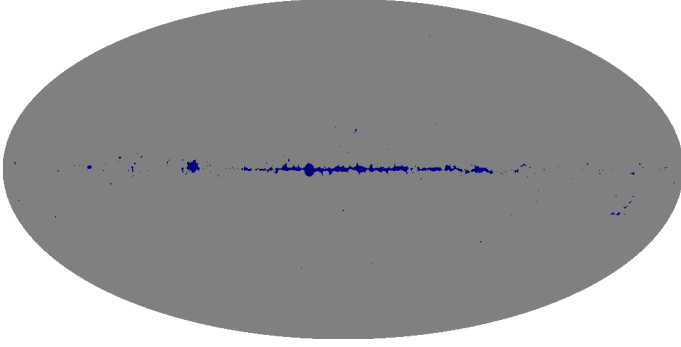


Fig. 38. Galactic mask used with NILC.

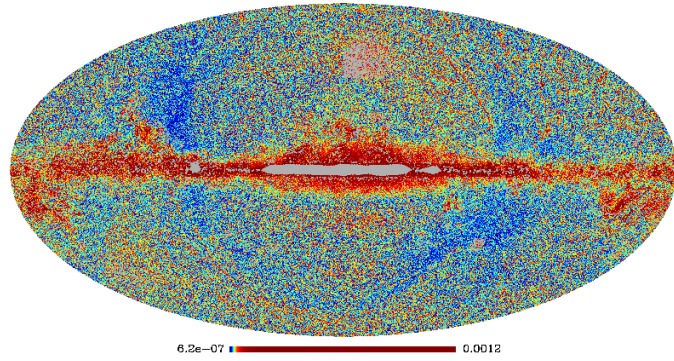


Fig. 39. Estimate of the rms error in the CMB subtraction. The map is histogram-equalised to bring out the details.

Before applying NILC, pixels missing due to point source and Galactic masking are filled in by a “diffusive inpainting” technique, which consists of replacing each missing pixel by the average of its neighbours and iterating to convergence. This is similar to solving the heat diffusion equation in the masked areas with boundary conditions given by the available pixel values at the borders of the mask. All maps are re-beamed to a common resolution of $5'$. Re-beaming blows up the noise in the less resolved channels, but that effect is automatically taken into account by the ILC filter.

The CMB template obtained after NILC processing is filtered to have the “Wiener beam” shown in Fig. 36. The ILC coefficients are saved to be applied to the jackknife maps for performance evaluation as described in Sect. 8.4.2

8.4. Uncertainties in the CMB removal

Uncertainties in the CMB removal have been gauged in two ways, firstly by comparing the CMB maps produced by the different algorithms and secondly by applying the NILC coefficients to jackknife maps.

8.4.1. Dispersion of the CMB maps produced by the various algorithms.

The methods that were used to produce the estimates of the CMB are diverse. They work by applying different algorithms (ILC, template fitting, or Bayesian parameter estimation) in a variety of domains (pixel space, Needlet/wavelet space, or spherical harmonic coefficients). Each method carries out its optimisation in a different way and thus will respond to the foregrounds

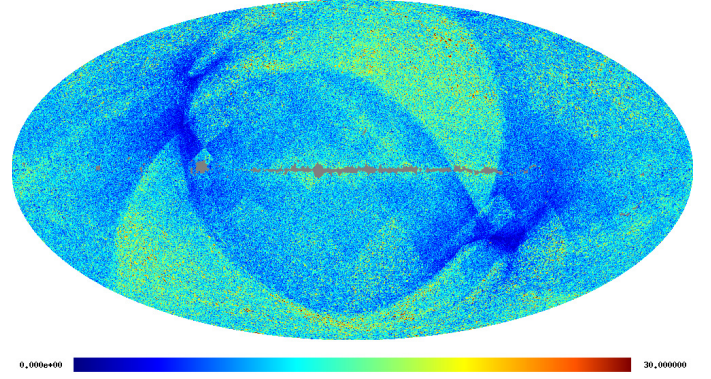


Fig. 40. Local rms of the noise (estimated by jackknife) in the NILC CMB map. The colour scale is from 0 to $30 \mu\text{K}$ per pixel at resolution $N_{\text{side}} = 2048$.

differently. Dispersion in the CMB rendition by different methods provides an estimate of the uncertainties in the determination of the CMB, and thus in the subtraction process. The rms difference between the NILC map and the other CMB estimates is shown in Fig. 39. As expected, the uncertainties are largest in the Galactic plane where the foregrounds to remove are strongest, and smallest around the Ecliptic poles where the noise levels are lowest.

8.4.2. CMB map uncertainties estimated by applying NILC filtering of jackknives

The cleanliness of the CMB template produced by the NILC filter can be estimated using jackknives. We apply the NILC filter to the maps built from the first and last halves of the ring set. The power distribution of the half-difference of the results provides us with a reliable estimate of the power of the noise in the NILC CMB template, (while previous results correspond to applying the NILC filter to the half-sum maps from which they can be derived).

The jackknives allow estimates of the relative contributions of sky signal and noise to the total data power. Assume that the data are in the form $X = S + N$ where S is the sky signal and N is the noise, independent of S . The total data power $\text{Var}(X)$ decomposes as $\text{Var}(X) = \text{Var}(S) + \text{Var}(N)$. One can obtain $\text{Var}(N)$ by applying the NILC filter to half difference maps, and $\text{Var}(S)$ follows from $\text{Var}(X) - \text{Var}(N)$. This procedure can be applied in pixel space, in harmonic space, or in pixel space *after* the maps have been bandpass-filtered, as described next.

We first used pixel space jackknifing to estimate the spatial distribution of noise. Figure 40 shows a map of the local rms of the noise. We applied the NILC filter to a half-difference map and we display the square root of its smoothed squared values, effectively resulting in an estimate of the local noise rms. Using the same approach, we obtain an estimate of the angular spectrum of the noise in the NILC map, shown in Fig. 41. That spectrum corresponds to an rms $[(1/4\pi) \sum_{\ell} (2\ell + 1) C_{\ell}]^{1/2}$ of $11 \mu\text{K}$ per pixel. The “features” in the shape of the noise angular spectrum at large scale are a consequence of the needlet-based filtering (such features would not appear in a pixel-based ILC map). Recall that the coefficients of an ILC map are adjusted to minimize the total contamination by both foregrounds *and* noise. The strength of foregrounds relative to noise being larger at coarse scales, the needlet-based ILC tends to let more noise in, with the benefit of better foreground rejection.

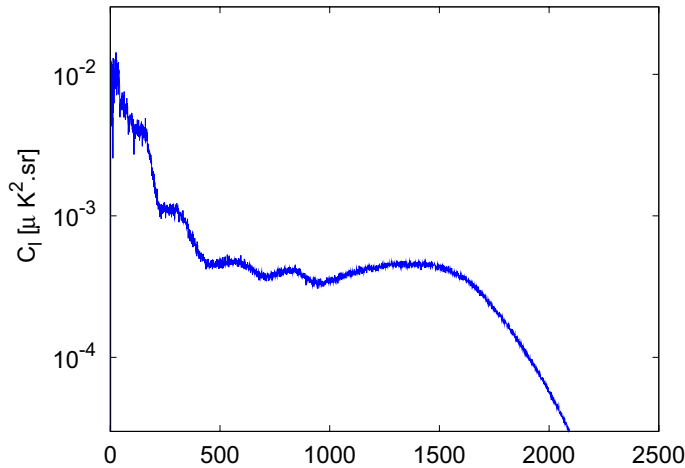


Fig. 41. Angular spectrum in μK^2 of the noise (estimated by jackknife) in the NILC CMB map. It corresponds to $11 \mu\text{K}$ per pixel.

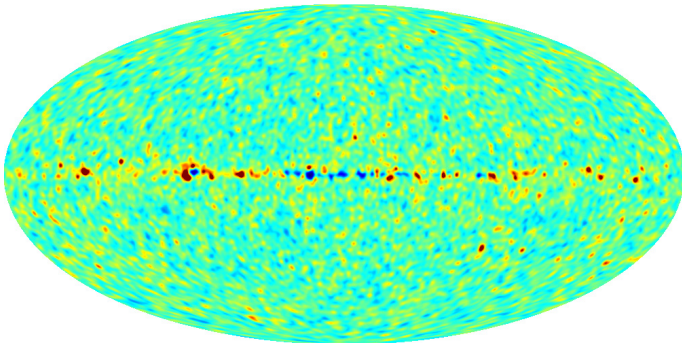


Fig. 42. Local power of the NILC CMB template in the range $\ell = 500 \pm 200$.

The half-difference maps offer simple access to the power distribution of the residual noise in the estimated CMB template. However, it is more difficult to evaluate other residual contamination, since all fixed sky emissions cancel in half difference maps. Any such large-scale contamination is barely visible in the CMB template, since it is dominated by the CMB itself. However, contamination is more conspicuous if one looks at intermediate scales. Figure 42 shows the local power of the CMB template after it is bandpassed to retain only multipoles in the range $\ell = 500 \pm 200$. This smooth version of the square of a bandpassed map clearly shows where the errors in the component separation become large and so complicate some specific science analyses.

9. Summary of processed data characteristics and conclusions

The data provided to the *Planck* collaboration by the HFI DPC consisted of:

1. channel (frequency) maps (e.g., Fig. 43);
2. hit count maps (Fig. 33);
3. half-ring maps (Fig. 34);
4. error map of the CMB template used for CMB removal (Figs. 39 and 42); and
5. masks (e.g., Fig. 38).

Channel maps were provided both with and without CMB removal. Table 4 summarizes their characteristics (prior to CMB

removal). It gives most of the information needed to make use of the maps. Further details and comments are given below.

9.1. Sensitivity

The numbers given in line a3 of the table directly indicate the white noise contribution to the rms in pixels of 1 degree on a side. They show that, with the current processing, the white noise level is slightly larger (or smaller) than the “Blue Book” values (Planck Collaboration 2005) (renormalised by duration i.e. by $\sqrt{14/10}$) by 20% (100 GHz), 11% (143 GHz), 8% (217 GHz), 25% (353 GHz), 16% (545 GHz) and -35% (857 GHz). These numbers pertain to the actual maps and do not include data from the RTS bolometers ($\sim 8\%$ of the 143 GHz data, and 25% at 545 and 850 GHz), or from the depointing manoeuvres or glitch flagging (another $\sim 20\%$ data loss in all bolometers). One should also bear in mind that any comparison in Kelvin at the highest frequencies is very sensitive to spectral band assumptions.

9.2. Angular response

Scanning beams: are determined from planet scans (lines b1–b4). They include the effect of the optical beam, of the electronic detecting chain, and of the TOI processing pipeline. This is an important intermediate product, although it is usually not relevant for astrophysical applications.

Effective beams: provide the response of a map pixel to the sky (lines c1–c4). Compared to the scanning beams, they further account for the combined effect of the scanning strategy and additional data processing. Different applications need different levels of accuracy and detail, from the mean FWHM of a symmetrical Gaussian description (line c1) to an actual Point Spread Function at each specific map location. For the time being, the dominant source of uncertainty remains the systematic uncertainties in the scanning beams. Mean ellipticities are given in line c3.

9.3. Photometric accuracy

The photometric calibration of the 100 to 353 GHz channels relies on the Solar dipole. Comparing the common CMB component at these frequencies shows that the relative accuracy between these channels is better than 2%, and is more probably at the per cent level. For the two highest frequencies, we use a comparison with FIRAS and find systematic variations as large as 7%, while the zero points of the maps are better than 2 MJy sr^{-1} (Lines d1–d4).

9.4. Spectral response and conversions

Line e1 provides a unit conversion coefficient, U , based on the knowledge of HFI spectral transmissions, which is accurate to better than one per cent. Other lines provide color correction factors for different power-law emission. The last line provides an estimate of the correction factor required to perform CO corrections (line e4). We now turn to details of its derivation and use.

Figure 44 shows the average band passes for each of the HFI frequency bands. The vertical bars show the rest frame frequencies of various CO-transitions. Appendix E details how ground data has been reprocessed to allow computation of the CO correction factor described below.

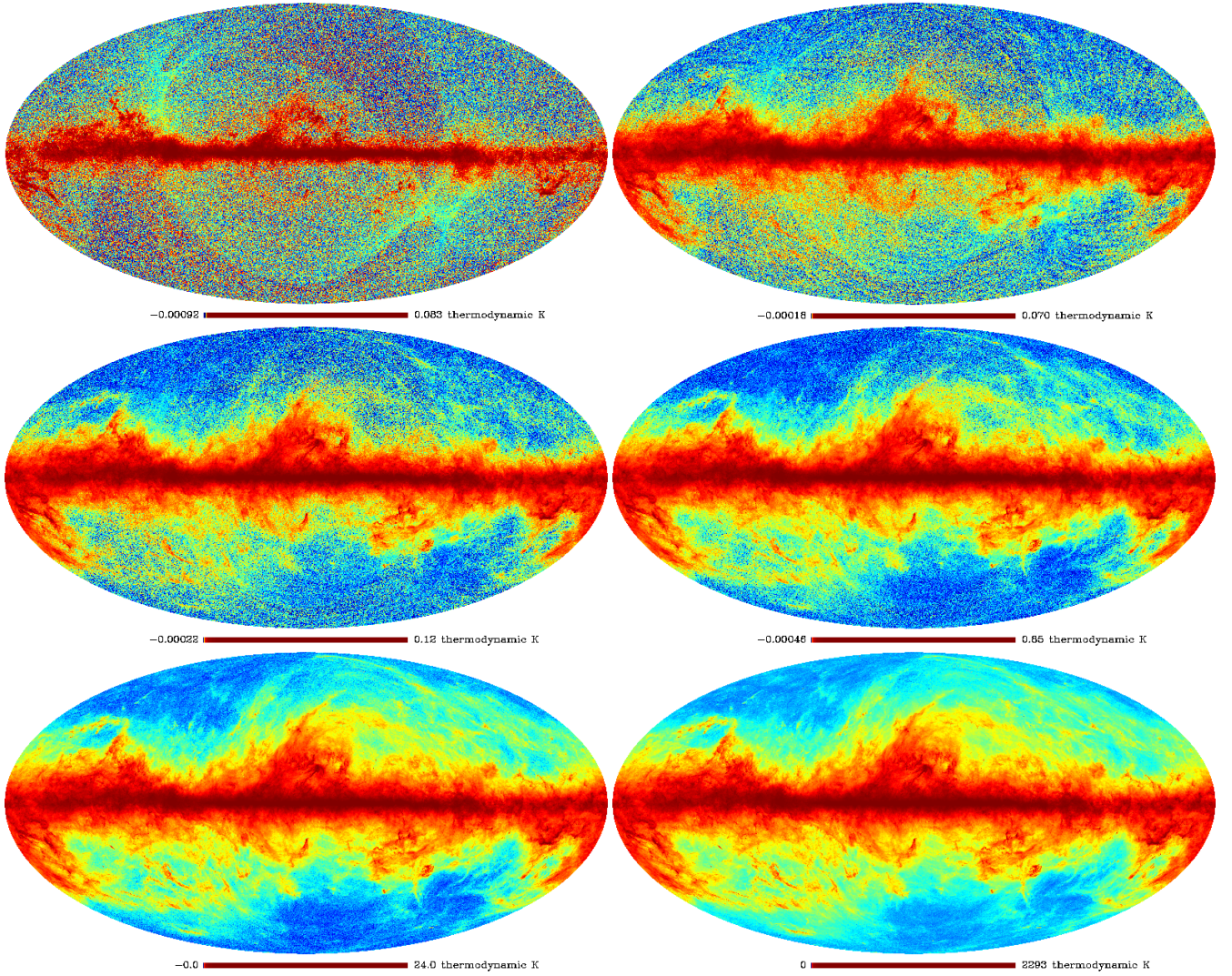


Fig. 43. CMB-removed channel maps. From left to right and top to bottom, 100, 143, 217, 350, 545, and 857 GHz. At high Galactic latitudes of the 100 and 143 GHz channel maps, the noise modulation caused by varying integration times is clearly visible, cf. Fig. 33.

A CO brightness temperature equivalent to a given CMB flux is determined by equating the integrated intensity of each. For the CMB, the intensity is taken to be $\Delta T_{\text{CMB}}(\partial B_\nu/\partial T)|_{T_{\text{CMB}}}$, similar to the approach used in colour correction. The CO flux is expressed as the product of Rayleigh-Jeans temperature and the spectral line width in velocity units, i.e. $\text{K}_{\text{RJ}} \text{ km s}^{-1}$. For CO regions of interest to HFI, i.e. the ones with excitation of the lowest rotational CO transitions, the CO gas temperatures are such that a Doppler broadening line profile may be assumed with $v \approx v_{\text{CO}}(1 - v/c)$ ($v \ll c$). The CO brightness temperature is defined in terms of an equivalent temperature for a Rayleigh-Jeans black body. Thus, the integrated CO flux may be expressed as $\int \Delta T_{\text{CO}} \tau(\nu)(v_{\text{CO}}/c)(\partial B_\nu/\partial T)|_{\text{RJ}, T_{\text{CO}}, v_{\text{CO}}}(v_{\text{CO}}/c) dv$. Furthermore, as the CO transitions occur at discrete frequencies, with a Doppler line-width much less than the transition frequency ($\sim 10^6$ Hz versus $\sim 10^{11}$ Hz), and much narrower than the available knowledge of the HFI detector spectral response ($\sim 10^8$ Hz), the velocity distribution of CO intensity may be approximated by a delta function at v_{CO} . Therefore, the conversion between CO brightness temperature and CMB temperature may be expressed as follows

$$F_{\text{CO}} = \frac{\tau(v_{\text{CO}})(\partial B_\nu/\partial T)|_{\text{RJ}, T_{\text{CO}}, v_{\text{CO}}}(v_{\text{CO}}/c)}{\int \tau(\nu)(\partial B_\nu/\partial T)|_{T_{\text{CMB}}} dv} \times 10^6. \quad (12)$$

Table 4 lists the average CO conversion factors (in μK_{CMB} per $\text{K}_{\text{RJ}} \text{ km s}^{-1}$ unit) and the associated uncertainties, determined using Eq. (12) for the main CO transitions of concern; similar data are available for the individual HFI detectors and the other transitions within HFI bands.

Statistical errors are computed for each of the detectors from the respective spectral bandpass uncertainties assuming Gaussian errors. The systematic errors account for spatial variations of those coefficients due to both spectral mismatch between detectors and non uniform weighting across the sky. Notice that the uncertainties are of the order of 10% and therefore of the same order as the calibration errors on the currently available templates, which are evaluated to be in the 10–20% range (Dame et al. 2001; Onishi et al. 2002).

Typically, it is found that in large molecular clouds the relative contribution of the CO line to the 100 GHz band is of the order of 10% (up to 30% in some locations).

9.5. Conclusions

This paper has covered the processing completed to date to enable early scientific analysis and produce the *Planck* Early Release Compact Source Catalogue (ERCSC). Many aspects

Table 4. Summary of the main characteristics of HFI early maps.

HFI Early maps – Main characteristics								
a^1	ν	[GHz]	100	143	217	353	545	857
a^2	N_{Bolo}		8	11	12	12	3	3
a^3	c_{WN}	[$\mu\text{K degree}$]	1.6	0.9	1.4	5.0	70	1180
b^1	θ_S	[arcmin]	9.53	7.08	4.71	4.50	4.72	4.42
b^2	$\Delta\theta_S$	[arcmin]	0.10	0.12	0.17	0.14	0.21	0.28
b^3	e_S		1.20	1.03	1.13	1.10	1.17	1.35
b^4	$\Delta\alpha_S$	[degree]	0.80	2.08	0.28	0.28	0.13	0.07
c^1	θ_M	[arcmin]	9.88	7.18	4.87	4.65	4.72	4.39
c^2	σ_{θ_M}	[arcmin]	0.04	0.02	0.03	0.04	0.06	0.05
c^3	e_M		1.15	1.01	1.06	1.05	1.14	1.19
c^4	σ_{e_M}		0.02	0.01	0.02	0.02	0.03	0.05
d^1	CMB relative calibration accuracy		$\leq 1\%$	$\leq 1\%$	$\leq 1\%$	$\leq 2\%$		
d^2	CMB absolute calibration accuracy		$\leq 2\%$	$\leq 2\%$	$\leq 2\%$	$\leq 2\%$		
d^3	FIRAS gain calibration accuracy						$\sim 7\%$	$\sim 7\%$
d^4	FIRAS zero point uncertainty [MJy sr^{-1}]		0.8			1.4	2.2	1.7
e^1	F_U	[$\text{MJy sr}^{-1}/\text{mK}_{\text{CMB}}$]	2.42×10^{-1}	3.69×10^{-1}	4.81×10^{-1}	2.88×10^{-1}	5.83×10^{-2}	2.24×10^{-3}
e^2	ΔF_U		$\leq 1\%$	$\leq 1\%$	$\leq 1\%$	$\leq 1\%$	$\leq 1\%$	$\sim 3\%$
e^3	$C(\alpha), \alpha = -2$		1.011	1.025	0.999	0.997	0.998	1.011
	$C(\alpha), \alpha = 0$		0.999	0.985	1.009	1.011	1.012	0.999
	$C(\alpha), \alpha = 1$		1.008	0.980	1.027	1.031	1.035	1.007
	$C(\alpha), \alpha = 2$		1.027	0.985	1.053	1.060	1.068	1.024
e^4	F_{CO}	[$\mu\text{K}_{\text{CMB}}/\text{K}_{\text{RJ}} \text{ km s}^{-1}$]	14.2 ± 1.0		44.2 ± 1.0	171.0 ± 6.0		

Notes. The first column refers to following notes pertaining to the content of the line, while the units are between brackets [] at the right of Col. 2. ^(a1) Channel map reference frequency, and channel identifier. ^(a2) Number of bolometers whose data was used in producing the channel map. ^(a3) This estimate of the small scale noise in the maps comes from the average level between $\ell = 100$ and $\ell = 1000$ of the power spectra of the Jackknife map (1st versus 2nd half of rings), with 40% of it masked, of Fig. 35. ^(b1) Average FWHM of the *scanning beam*, θ_S , determined on planets (Mars); it is obtained by unweighed averaging the individual detectors FWHM. Each FWHM is that of the Gaussian beam which would have the same solid angle ($\Omega_S = 2\pi(\theta_S/2\sqrt{2\ln 2})^2$) as that determined by using a full Gauss-Hermite expansion on destriped data. FWHM from straight Gaussian Elliptical fit would rather give 9.45, 7.01, 4.68, 4.45, 4.48 and 4.22 arcmin. ^(b2) Uncertainty in determining the scanning beam FWHM, θ_S . This conservative uncertainty is derived through the dispersion of results of several methods. ^(b3) Ellipticity of the scanning beam. The formal uncertainty on these numbers is quite small, always smaller than 1%, but it is likely misleading. This formal uncertainty is defined as the square root of the second diagonal element of E_S , the 3×3 covariance matrix for fitting $(\theta_S, e_S, \alpha_S)$ to the data. ^(b4) Typical uncertainty in determining the direction of the scanning beam elongation. (Square root of the third diagonal element of the covariance matrix E_S defined in note $b3$.) ^(c1) Average FWHM of the *effective beam* at map level, θ_M . This gives the typical width of the beam, as an average over 3000 locations in the map of the local effective beam resulting from combining many measurements per pixel. It tends to increase the beam FWHM by a few percent with respect to the scanning one. ^(c2) Standard deviation of the variation of the FWHM of the effective beam at the map level (at the location of the *Planck* ERCSC sources), assuming the input scanning beam is exact. This line shows that the variation of the effective beam FWHM from one location to the other is smaller than the uncertainty on the scanning beam FWHM quoted above. ^(c3) Average ellipticity of the effective beam at the map level. ^(c4) Standard deviation of the ellipticity of the effective beam at the map level. ^(d1) Relative calibration accuracy between frequency channels. Estimate based on cross-correlation between maps of the CMB component, see details in Sect. 7.5. ^(d2) Estimate based on simulations of the calibration procedure on the solar system kinematic dipole. This assumes WMAP determination is exact, and perfect data (e.g., no LFER-induced systematics). ^(d3) Estimate of the systematic error (which dominates the error budget) through the dispersion of estimates obtained in different regions of the sky. ^(d4) Overall error on the map zero point, for a $\nu I_\nu = \text{constant}$ spectrum. ^(e1) This unit conversion factor, F_U , relies on the knowledge of the spectral bands. ^(e2) Uncertainty estimate of the unit conversion factor. ^(e3) Colour correction $C(\alpha)$, assuming a sky emission of the form $I_\nu \propto \nu^\alpha$. This factor C is the one by which the flux of the source need to be multiplied in order to compare with the HFI map or catalogue value. All colour corrections quoted are good at the 2% level or better. ^(e4) CO correction obtained as described in Sect. 9.4. These factors corresponds to the CO lines J 1–0, J 2–1 and J 3–2 (respectively) at 100, 217 and 353 GHz.

will be improved in later data passes, using the knowledge gained from this round of analysis and further rounds using more data. Examples of possible improvements include an improved deglitching by further tuning of the method we use (in particular for PSB-b and SWB bolometers), a better knowledge of the effective beams through all of its components (in particular the instrument temporal transfer function, and the scanning beams derived from more planet scans), an improved pointing solution, a further reduction of 4 K line residuals, the use of the orbital dipole as a primary calibrator, modelling the zodiacal light contribution and far side lobes of the beams, and quantifying polarization systematics.

At this stage, *Planck* data appears to be of high quality and we expect that with further refinements of the data processing we

should be able to achieve, or exceed, the science goals outlined in the “Blue Book” *Planck* Collaboration (2005).

Acknowledgements. A description of the *Planck* Collaboration and a list of its members with the technical or scientific activities they have been involved into, can be found at http://www.rssd.esa.int/index.php?project=PLANCK&page=Planck_Collaboration.

Appendix A: Overview of the DPC infrastructure

The HFI Data Processing Centre can be thought of as a centralized backbone providing hardware and software infrastructures to a relatively large number of geographically distributed groups of developers and other R&D groups in the HFI and LFI core

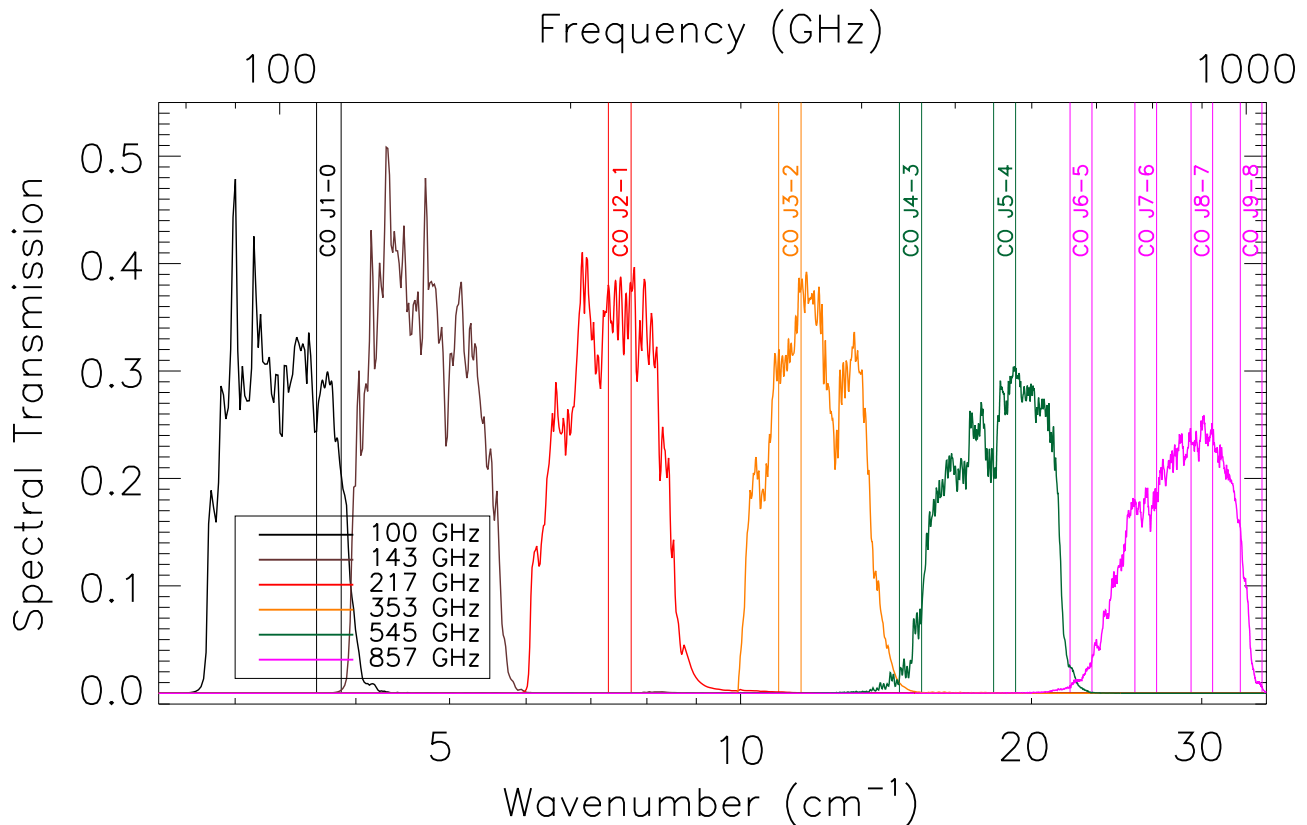


Fig. 44. The average spectral response for each of the HFI frequency bands. The vertical bars represent the spectral regions of CO transitions and are interpolated by a factor of ~ 10 .

teams. This appendix provides brief overviews of the main HFI infrastructures elements.

A.1. Code and configuration management

The modules in the pipeline have been programmed by the scientists and engineers of the HFI DPC in C, C++, Fortran and Python. IDL is also available and used for post-processing, analysis, and for interactive work. All codes are shared and tracked in a common versioning system (CVS), and are grouped into *packages* which can be tagged with their version number. In addition to this versioning system, a set of scripts based on CMT⁹ are used to define and build (executable) code releases based on a specific tag of each CVS package included. Each code release includes basic libraries (e.g., to access the data), modules (basic executables), and pipelines (scripts that execute many modules). CMT provides a build system (based on a set of *make* rules) that ensure that a given code release is built in a coherent manner, i.e. tracking the library dependencies and versions, including the versions of the compiler and other external libraries. Several code releases are maintained, but old releases are deleted. Developers can build a local (edited) version of any package but using the libraries from the release. They can thus test their code before committing it to CVS, tagging it, and finally *announcing* it so that it will be included in the next release. Code releases are built at irregular intervals (daily to weekly) depending on needs (new features, corrections, bug fixes).

⁹ <http://www.cmts.org/>

A.2. Data management – HFI-DMC

All data after L1 processing are stored in the HFI Data Management Component (DMC) database, which is therefore the reference database. In fact, only the metadata are effectively stored in a PostgreSQL¹⁰ database. The data themselves are stored on disk as binary files of a machine-dependent size optimized for read and write speed. Data access is possible only via queries of the database. This induces a bottleneck in the system when many modules need simultaneous access to a given data object, and thus query the database at the same time. Different technical solutions, including the quick spawning of part of the database have been implemented to alleviate this problem. For massively parallel modules, a parallel query layer based on the MPI library¹¹ has been developed. The system is able to sustain up to 600 concurrent operations on the same database object without noticeably slowing down due to the centralized database. Without our optimization, the centralized database model would develop a bottleneck after a few concurrent operations on the same object (typically the number of available cores on the server). With our modifications, a central metadata handling system can provide efficient object management over a parallel system and also control of concurrent access properties such as locking.

To optimise read and write rates, an HFI-DMC object can be stored in different physical locations (node memory, node local disk, cluster disk array, etc.). The use of local memory or disk is used intensively in the Monte-Carlo pipeline to avoid the overheads of transferring data to cluster disks. In this way pipelines

¹⁰ <http://www.postgresql.org/>

¹¹ <http://www.lam-mpi.org>

can read/write many TB of (temporary) data very rapidly without using resources other than those of the nodes on which they are running.

The metadata stored in the database proper consists typically of generic file access information (name of the creator, date of creation, data rights, history) which is analogous to the fits file metadata (for example for HEALPix maps, the ordering, Nside...), as well as the list of all access rights to the data, with a link to the pipeline, module or interactive session that is responsible for that access.

Pipelines, modules, or interactive (IDL or Python) sessions that need access to the data must use a dedicated library which interfaces with the database, and stores a trace of the access as a dedicated, pure metadata object in the database. Hence, module parameters, the version of the pipeline or module as well as the release within which it has been compiled and run is stored in the database. Log files are maintained external to the database, as for the data, but are referenced therein.

All of this information can easily be queried using command line interfaces, or through a dedicated web interface.

Thus, at any stage, the full history of any data hosted in the database can be obtained (using for example a dedicated web page). Furthermore, computations applied to any data can be reproduced simply by re-running the different pipelines or modules (in the same version, with the same release) with their parameter files, provided a released version of the code has been used.

A.3. The IMO database

The purpose of the IMO (instrument model) is to store the current knowledge about the HFI behaviour in a unique location within the DPC. The IMO is necessarily restricted in complexity and is tailored specifically for use in processing the data. The IMO is:

- a database of the fixed parameters of subsystem models;
- complementary to TOIs and Maps in the DMC;
- DPC oriented; i.e. a simplified (effective rather than physical) instrument model for the data processing and simulations;
- accessible via modules in C, Fortran, Python and IDL;
- browsable on the internet and can be exported to xml format;
- maintained as a consistent unit (global changes increment the major version counter).

Note that “transfer functions” (see below) in L1 use the same IMO than other processing levels. This saves storage as only raw data are stored and on-the-fly conversions are made to retrieve objects in physical units. It also ensures that L2 and L1/QLA use the same functions and the same parameters.

The IMO contains either direct values (e.g., a detector gain, a FWHM) with uncertainties and units, or links to DMC objects (e.g. bandpass tables, beams maps). There is one distinct IMO for each “instrument” (CQM, PFM, Flight). Although limited in scope, the current reference version for the flight instrument contains about 17 000 values.

Finally, one should note that it is possible to create sets of IMOREALISATION(s) for Monte-Carlo purposes. Each Monte-Carlo iteration use one version of an IMOREALISATION attached to the same IMO object. Simulations can use IMOREALISATION information if specified, otherwise they use the IMO. An IMOREALISATION therefore provides a way to redefine, at each Monte-Carlo iteration, some instrument properties based on the same global instrument definition.

A.4. Common libraries

Apart from the IO library interfacing programs with the database, a few common libraries are included in the HFI releases. Most of them are well known mathematical libraries (FFTW¹², NAG¹³, LAPACK¹⁴, GSL¹⁵). We are also including in our releases classical IDL libraries such as the Astronomy User’s Library¹⁶, as well as Python packages such as matplotlib¹⁷, Cython¹⁸, numpy and scipy¹⁹. Finally, we are using HEALPix²⁰ (Górski et al. 2005), its Python wrapper healpy²¹ as well as libpsht²² (Reinecke 2011).

The HFI DPC also developed and maintains three specific libraries:

- the first is a set of *transfer functions*, interfaced with the database, that can be automatically applied to data at read time. Thus, many virtual views of the data can be built whilst saving disk space. These different views can be simple unit changes, or more complex combinations combining and processing several objects (e.g., a voltage from a stored resistance and a current);
- the second is a *pointing library* which is used to compute bolometer pointings. Only the attitude of the satellite is stored in the database. Pointings for each individual bolometer are computed on the fly, combining the attitude with the location of the detectors in the focal plane reference frame. At low computing cost, the library can also change the reference frame into which the pointing is expressed, or the convention used to express it (e.g., Cartesian coordinates or RA and Dec). The library is interfaced with the database so that the locations of the detectors in the focal plane are retrieved from the IMO directly. The definition of this pointing (as a maximum of some analytical approximation of the optical beam) can be easily changed;
- finally, the third library is dedicated to the computation of the *orbital dipole*. It is also interfaced with the database, and has directly access to the data describing the orbit of the satellite.

A.5. Data flow management – THINC

Pipelines represent an important part of the DPC code. They are collections of modules (or other pipelines) linked by their dependency relations. To pipe the execution of computational tasks, modules and pipelines must be described by a “prototype”, i.e. the definition of the content of their parameter files along with rules to be imposed on those parameters (e.g., that one parameter must be bigger than another, or that a list must have the same number of elements as another). These prototypes also allow for automatic documentation as well as automatic production of template parameter files or pipelines.

The THINC tool is a Python library interfaced with a runtime environment that allows one to describe pipelines and execute them. Pipeline descriptions are in fact Python scripts interfaced

¹² <http://www.fftw.org/>

¹³ <http://www.nag.co.uk/>

¹⁴ <http://www.netlib.org/lapack/>

¹⁵ <http://www.gnu.org/software/gsl/>

¹⁶ <http://idlastro.gsfc.nasa.gov/contents.html>

¹⁷ <http://matplotlib.sourceforge.net/>

¹⁸ <http://www.cython.org/>

¹⁹ <http://scipy.org/>

²⁰ <http://HEALPix.jpl.nasa.gov>

²¹ <http://code.google.com/p/healpy/>

²² <http://sourceforge.net/projects/libpsht>

with the THINc runtime and the database. The script sets the content of the parameter file of each executable that is part of the pipeline. The runtime deduces the data flow relationship from those parameters looking for corresponding output and inputs, takes care of the submission of the executable to the batch system, and monitors the correct execution of each computational task. Since pipelines are Python scripts, direct access to the data is also possible within the script (for example, reading a database object that has been produced by a module and deciding on the execution of the rest of the pipeline accordingly). The runtime also detects such access, and makes sure that the data flow is still correct. Finally, all information related to the pipeline (parameter files, log files...) is committed to the database and can be queried later on, for example, to check whether the results of a given pipeline are consistent between releases.

The THINc tool has several execution models that can be selected by users. Indeed HFI-DPC infrastructure needs to and is used on various platform types, massive computations need adaptations to the local hardware.

Finally, in one year (Oct.-2009 to Oct.-2010), using MAGIQUE-III (one of the dedicated computers of the HFI-DPC, see below) 559 000 processes were executed, reading or writing 7.5 Peta-Bytes, using 450 000 CPU hours.

A.6. Hardware

HFI-DPC has a dedicated computing facility hosted by the Institut d'Astrophysique de Paris called MAGIQUE-III. MAGIQUE-III is a cluster consisting of 284 Xeon processors/1128 cores built by IBM. The theoretical peak performance of the whole cluster is around 13 TFlops. A GPFS parallel file system of around 100 TB usable storage is available and visible by all the login and compute nodes.

The nodes are interconnected with a high-speed (20 Gbit/s) point-to-point InfiniBand switch. This medium-sized computing facility is used for operation and most common analysis. This hardware is used for the day-to-day analysis and provides enough processing power for preliminary MonteCarlo loops.

The HFI-DPC infrastructure is also available at several other computing centre (CCIN2P3, Darwin at CPAC, NERSC). These larger machines are available for massive computations, in particular large-scale Monte-Carlo simulations.

A.7. TOI simulations

The simulation methodology consists of two parts: LevelS-Core, focused on the calculation of the sky power falling on detectors and LevelS-Desire, which simulates the HFI detectors response. Both are described below. The simulated detector response is specific to each instrument and requires access to information contained and updated in the unique centralised database of parameters of the instrument model, the *imo*.

A.7.1. LevelS-Core: sky power infalling on detector

The LevelS-Core is a set of modules (programs) developed jointly by the HFI, LFI and MPA teams and integrated at MPA to compute the sky power infalling on Planck detectors (Reinecke et al. 2006). Its HFI avatar takes advantage of the features of the HFI DMC.

The first pipeline, LSCmission, takes as input a Pre-programmed Pointing List (PPL, a plain text file containing one fixed-length formatted line per pointing period of

the mission, typically generated by MOC) and translates it into the HFI DMC objects containing the mission parameters, namely:

- the satellite's position, rotation speed, spin axis orientation, start and end time for each pointing period;
- precise satellite position and orientation at 1 Hz;
- start and end sample number for each pointing period;
- a catalogue of Solar System Objects (SSO) positions for each pointing period.

And optionally:

- a quaternion representing the pointing and attitude of the satellite at the bolometer's sampling frequency;
- a vector of the satellite's spin axis in ecliptic spherical coordinates for each pointing period.

The second pipeline, LSCorePipe, takes as inputs the results of LSCmission, together with:

- maps from the *Planck* Sky Model;
- a point sources catalogue from the PSM;
- beam descriptions in GRASP format (from the *imo*);
- the spectral response of the bolometers (from the *imo*).

LSCorePipe generates TOIs of antenna temperature per bolometer, containing the simulated power received from the user's selection of sky components (CMB, orbital dipole, Sunyaev-Zeldovich effect, planets, point sources and Galactic emission). We refer to them as "sky signal" TOIs, and they are in units of mK_{RJ}.

A.7.2. LevelS-Desire: detectors simulated response

The LevelS-Desire (Detectors simulated response) is a set of modules that simulates the HFI instrument. They convolve the sky signal TOIs from the LevelS-Core with the instrument response to produce TOIs of modulated signal, in ADUs, as given by the L1. These include:

- scientific signal of the 52 bolometer channels;
- fine thermometers – 10 channels over the 4 K, 1.6 K and 0.1 K stages;
- housekeeping, readout electronics unit.

It is divided into two parts that deal separately with the bolometers and thermometers, and it accounts for the following instrumental effects:

- temperature fluctuations of the telescope and cryogenic stages;
- non-linear response of the bolometers;
- temporal response of the bolometers;
- response of the electronic chain – gain and filtering;
- various components of the noise (see below).

Models of HFI response to temperature fluctuations of the telescope and the three cryogenic stages (4 K, 1.6 K and 0.1 K) have been implemented. The behaviour of the detectors has been divided into a non-linear and a linear time response. These parameters depend on the electronic set-up of the REU and of the instrument (telescope temperature, cryogenic stage temperatures, sampling frequency). The non-linear response is modelled by a polynomial law and gives the conversion factor from Watts received by the detector to ADU. The time response effect is computed in Fourier space. The complex filters contain the electronic

time response and the bolometer time response that is modelled by two components: one short time constant (about a few ms) and a long time constant (LTC) of a few 100 ms. These properties have been integrated into a complete model of the instrument response SEB (Simulation of the Electronics and Bolometer) that has been used to provide the inputs to the Desire module.

Finally one module is dedicated to the various components of the noise that are added on the signal:

- white noise (REU and JFET noise);
- convolved noise (phonon and photon noise);
- glitches;
- 4 K harmonics (electromagnetic coupling between the 4 K cooler and the detectors);
- RTS noise.

These various components are optional and can be switched on or off to test the specific impact of each systematic effect. The parameters of these systematic effects have been estimated during the various calibration runs of the instrument.

In addition, to ensure the completeness of the simulated dataset, the housekeeping (HK) data are written to the DMC database to be read subsequently by the TOI processing and L2 pipelines. This pipeline has been written to work within the DPC environment (e.g., DMC+ThinC), and uses the understanding of the instrument accrued in the IMO.

The performance of the Levels-Desire pipeline was evaluated pre-launch. Generating one year of data needs 2.5 cpu hours for each bolometer and 2 cpu hours for thermometers with 37 GBytes of data generated for each. This leads to 170 cpu-hours and 2.7 TBytes storage to generate a simulation of one year of data for the entire focal plane of the *Planck* HFI.

Appendix B: Focal-plane measurements

In this appendix we describe the algorithms used to measure and monitor the focal-plane geometry and the shape of the individual detector beams.

B.1. The algorithm

The pipeline for extracting beam and focal-plane measurements uses a series of modules linked by the HFI DPC infrastructure (see Appendix A). As input data, the pipeline uses the product of the TOI processing pipeline (cf. Sect. 4). This data has been calibrated, flagged for glitches, and has had various temporal filtering applied as described in previous sections. The pipeline is iterative, requiring starting values for the focal-plane geometry which are then updated by the pipeline.

To obtain a first in-flight check of the focal plane geometry prior to the observation of the planets, we cross-correlated the TOIs of different detectors to obtain the time lag of the easily identified crossings of the Galactic plane. These lags were combined with the satellite rotation rate to obtain the in-scan separations. The results proved consistent with pre-launch values, taking into account that the measured lags are affected also by the cross-scan displacement of the detectors and also by their observing frequency.

For a given object (planet or other compact source) we first find the rings for which the focal plane intersects the object. This part of the pipeline is also capable of removing constant offsets for each ring (as calculated by the map-making pipeline). From this significantly reduced volume of destriped data we make a “naive” map (i.e. averaging into map pixels assuming constant noise) around the source (for planets, the map is centred

around the known, moving, position) using the nominal focal-plane geometry. This allows us to produce visualizations from each detector.

We then fit a parametric beam model either to these maps, or to the destriped time-stream data. The two-dimensional Gaussian is parametrized as

$$B(x_1, x_2) = \frac{A}{|2\pi\Sigma|^{1/2}} \exp\left[-\frac{1}{2} \sum_{i,j=1}^2 (x_i - \bar{x}_i)\Sigma_{ij}^{-1}(x_j - \bar{x}_j)\right], \quad (\text{B.1})$$

where A is an overall amplitude, (x_1, x_2) are two-dimensional Cartesian coordinates (we project to a flat sky), (\bar{x}_1, \bar{x}_2) are the coordinates of the beam centre, and the correlation matrix is given by

$$\Sigma = \begin{pmatrix} \sigma_1^2 & \rho\sigma_1\sigma_2 \\ \rho\sigma_1\sigma_2 & \sigma_2^2 \end{pmatrix}. \quad (\text{B.2})$$

Hence, for the Gaussian model, we fit for the parameters $A, \bar{x}_1, \bar{x}_2, \sigma_1, \sigma_2, \rho$. These can also be expressed in terms of the ellipticity, e (defined here as the ratio between the major and minor axes), and rotation angle α , of the Gaussian ellipse.

The *Planck* beams are known to have non-Gaussian features. Hence, we model deviations from Gaussianity as a series of elliptical Gauss-Hermite polynomials as discussed in the *Planck* context by Huffenberger et al. (2010). Note that we first fit an elliptical Gaussian as above and then (i.e. not simultaneously) solve for the Gauss-Hermite coefficients. The basis functions are defined as

$$\Phi_{n_1 n_2}(\mathbf{x}) \propto H_{n_1}(x'_1)H_{n_2}(x'_2) \exp(-\mathbf{x}' \cdot \mathbf{x}'/2), \quad (\text{B.3})$$

where $H_n(x)$ is the order- n Hermite polynomial and the primed coordinates \mathbf{x}' rotates into a system aligned with the axes of the Gaussian and scaled to the major and minor axes σ_i (i.e. to the principle axes of the correlation matrix Σ). Note also that the Gaussian approximation, in general, underestimates the effective area of the beam compared to the Gauss-Hermite parametrization.

In practice, we have found that the TOI-based code is better suited to measuring the beam parameters, and the map-based code to the focal-plane positions (using the result from the TOI code as a first guess to a Levenberg-Marquardt search). Because the projection to a two-dimensional coordinate system requires prior knowledge of the detector positions, we can iterate this procedure to account for any inaccuracies induced by differences with respect to the nominal detector positions. In practice, this correction is negligible.

Within the DPC infrastructure, detector positions (and all other directions relative to the spacecraft frame) are stored and manipulated as quaternions (Shuster 1993). The translation from our two-dimensional fits into quaternions complicates the error analysis somewhat. We represent the error (a difference between two rotations) as another rotation. However, because it is an error, it is convenient to represent it with quantities that are both numerically small for small errors and are not subject to constraints (e.g., to represent a rotation, the four entries in a quaternion must be normalized, and a rotation matrix must be orthonormal); hence we store rotation errors as a vector pointing along the rotation axis with magnitude given by the rotation angle. We can then store a rotation error covariance matrix as a non-singular three-by-three positive definite symmetric matrix.

To monitor the focal-plane geometry, we collect the results for all detectors with a single source and calculate the offset of

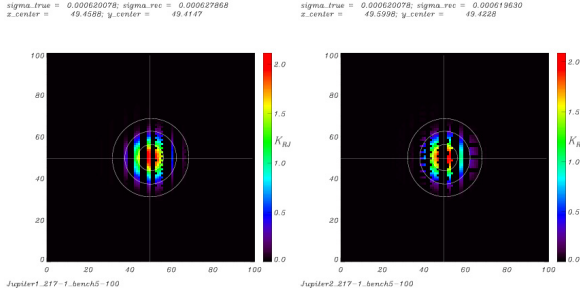


Fig. B.1. Simulated mini-map images of Jupiter for the 217-1 detector, from the first scan (*left*) and second scan (*right*).

each detector position with respect to the nominal (input) position. This produces a diagnostic of any overall shift in the positions as well as an estimate of the noise on the measurement. The results from individual detectors are then combined to determine an overall rotation (quaternion, with errors as explained above) and scaling with respect to the nominal model.

B.2. Validation on simulated data

In Fig. B.1, we show simulated maps of scans of Jupiter for the 217-1 detector (see Sect. A.7 for further information on the simulations). (Unlike the flight data, these simulations do not include a nonlinear response for Jupiter observations, nor glitch residuals, but these are small effects compared to the other sources of uncertainties.) Vertical striping in the map is due to the discrete jump of 2.5 arcmin between observation of rings. Hence, measurements of detector positions and beam shapes in the scan direction are considerably better than in the cross-scan direction.

In Fig. B.2 we show simulation results of scans of Saturn, including realistic noise. The results for the entire HFI focal plane are plotted as offsets with respect to the actual detector positions used in the simulations. For the majority of detectors, we find agreement to an accuracy of about 10 arcsec, except for several conspicuous outliers; these are the multi-moded horns at 545 GHz, for which the input detector positions were defined as the points of maximum response, as opposed to the centre of an appropriately fitted beam shape. Discounting those points, we conclude that we can recover the detector positions within the focal plane to an rms accuracy of ~ 4 arcsec.

Appendix C: Detector noise measurements

Our goal is to characterize the detector noise, as accurately as possible, starting from the time-streams produced by the TOI preprocessing pipeline. We have therefore developed a diagnostic toolbox to monitor, among other things, localized auto and cross-power spectra of noise to provide information about the mean white noise level per detector, low frequency drift behaviour, narrow lines (caused, for example, by microphonic noise from the 4 K cooler) and common noise modes between detectors. To monitor time variable trends in the noise properties, the estimates are made on a ring-by-ring basis. The noise estimation pipeline consists of three different modules:

- noise time-stream estimation from the input data²³ time-stream, on a ring-by-ring basis;

²³ By “input data” we mean the output of the TOI processing pipeline, namely the total signal (sky + noise) time-stream calibrated in units of absorbed power.

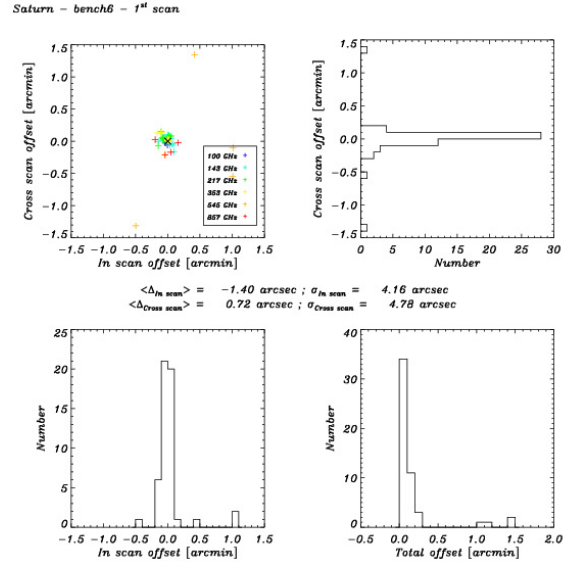


Fig. B.2. Recovery of the focal plane position in the in-scan and cross-scan directions using simulated scans of Saturn. *Upper left* shows individual detectors, other three show histograms, as marked.

- empirical auto and cross-spectra estimation on predefined “stationary zones” (in practice, the rings);
- fitting to a parametric noise model to provide, e.g., the Noise Equivalent Power, knee frequency, and the spectral index of the low-frequency noise component.

C.1. Theory

C.1.1. Noise power statistics

Ferreira & Jaffe (2000) show that the joint maximum likelihood estimation of the signal and noise power spectrum can be obtained iteratively. Let us assume that the data time-stream, d_t is related to the signal and the noise via

$$d_t = s_t + n_t = A_{tp} T_p + n_t, \quad (C.1)$$

and \mathbf{A} is the projection matrix relating the sky signal \mathbf{T} in the map pixel p to the signal detected in the time-stream at time t (i.e. the pointing matrix). The noise is assumed to be a Gaussian stationary process with covariance matrix $N_{t't'} = N(t - t')$. If the signal and noise are assumed to be independent (which is a good approximation except perhaps for very strong signals where the linearity of the detector breaks down), then the joint posterior probability on signal and noise power can be factorized as follows:

$$P(T_p, \tilde{N}(\omega) | d_t) \propto P(\tilde{N}(\omega)) \times P(T_p) \times P(d_t | \tilde{N}(\omega), T_p), \quad (C.2)$$

where the last term is just the joint likelihood \mathcal{L} of the signal and noise power spectrum $\tilde{N}(\omega)$, where

$$N(t - t') = \int \frac{d\omega}{2\pi} \tilde{N}(\omega) e^{-i\omega(t-t')}. \quad (C.3)$$

The joint likelihood can be expressed in the following way:

$$\begin{aligned} -2 \ln \mathcal{L} &= \ln |\mathbf{N}| + (\mathbf{d} - \mathbf{s})^T \mathbf{N}^{-1} (\mathbf{d} - \mathbf{s}) \\ &\approx \sum_k \ln \tilde{N}_k + |\tilde{d}_k - \tilde{s}_k|^2 / \tilde{N}_k, \end{aligned} \quad (C.4)$$

where the last line expresses the likelihood in terms of the discrete Fourier modes and is approximate because the noise matrix

\mathbf{N} is Toeplitz rather than circulant. Let us now express the derivatives of the joint posterior, where the noise power is assumed to be constant within frequency band α :

$$\frac{\partial \ln P(T_p, \bar{N}_\alpha | d_t)}{\partial \mathbf{T}} = (\mathbf{d} - \mathbf{A}\mathbf{T})^T \mathbf{N}^{-1} \mathbf{A}, \quad (\text{C.5})$$

$$\frac{\partial \ln P(T_p, \bar{N}_\alpha | d_t)}{\partial \bar{N}_\alpha} = -\frac{1}{2\bar{N}_\alpha} \left[(n_\alpha + 2\nu) - \frac{1}{\bar{N}_\alpha} \times \sum_{k \in \alpha} \sum_p |\tilde{d}_k - \tilde{A}_{kp} T_p|^2 \right], \quad (\text{C.6})$$

where n_α is the number of wavenumbers within the band α , and we have assumed a noise prior of the form

$$P(\bar{N}_\alpha) \propto \frac{1}{\bar{N}_\alpha^\nu}. \quad (\text{C.7})$$

Setting these derivatives to zero, we obtain the following equations that can be solved iteratively:

$$\mathbf{T} = (\mathbf{A}^T \mathbf{N}^{-1} \mathbf{A})^{-1} \mathbf{A}^T \mathbf{N}^{-1} \mathbf{d}, \quad (\text{C.8})$$

$$\bar{N}_\alpha = \frac{1}{n_\alpha + 2\nu} \sum_{k \in \alpha} \sum_p |\tilde{d}_k - \tilde{A}_{kp} T_p|^2. \quad (\text{C.9})$$

However, here we are not interested in the signal estimate itself and so we marginalize over all possible values of the signal to find the posterior distribution on the noise power. For an idealized ring scanning strategy, in which the pointing matrix selects spin-harmonic frequencies, the a posteriori solution for the noise power spectrum with signal marginalization can be expressed as a periodogram estimate on the signal subtracted data time-stream, renormalized to take into account the projection of the spin-synchronous noise modes. For a realistic scanning strategy, the projection operator on spin-synchronous signal modes is however more complicated and the marginalized posterior is no longer factorized over frequencies. In practice, we compute the joint posterior maximum, with the simplification of replacing the maximum posterior estimate of the signal at fixed noise spectrum with the “naive” (equal-weight) signal estimate. This is justified because the noise covariance in phase modes is almost diagonal (because of the specific scanning strategy on a ring). For the pure diagonal case, the optimal signal estimator and the naive ones are identical as the signal estimation can be done independently for each phase mode. Nevertheless, as we discuss below, the noise power estimates around the spin-synchronous frequencies are pathological.

C.1.2. Unbiased periodogram estimates

In practice, the data time-streams contain flagged data, identifying the presence of cosmic ray glitches, unstable pointing periods, etc. The missing data complicates the estimation of noise. Our approach here is similar to the estimation of pseudo power spectra: we compute the “raw” periodogram on the estimated noise time-stream, with flagged data set to zero and we perform the same operation on the flagged time-stream (set equal to one in valid regions and zero otherwise). We then compute the Fourier transform of both periodograms, divide the first by the second, and take the inverse Fourier transform. This gives an unbiased estimate of the underlying power spectrum. Finally, in their Eq. (5), [Ferreira & Jaffe \(2000\)](#) make the approximation that the noise covariance matrix is circulant whereas it is, in fact, Toeplitz. To correct for this, we replace the simple periodogram

estimates by windowed periodogram estimates ([Dalhaus 1988](#)). The length of the periodograms is a parameter of the pipeline, as is the overlapping factor between adjacent periodograms. All periodogram estimates are averaged over a “stationary zone”, chosen in practice to coincide with a given ring. The procedure outlined above generalizes easily to the multi-channel case, where power spectra are complemented with cross-power spectra between detector time-streams.

C.1.3. Signal estimation procedure

As described in Sect. C.1.1, the iterative optimal signal estimates required to maximize the joint likelihood of signal and noise power can be replaced by a “naive” (flat-weighted) estimate of the signal power to good accuracy. This is because, to a first approximation, the only non-zero sub-block of the pointing matrix (when expressed as relating time frequencies to phase frequencies) on a given ring is equal to the identity matrix (for the subset of time-frequency modes that are spin-synchronous). Small deviations from this pointing matrix model leads to second order corrections to the signal estimates²⁴. In fact, the more significant problem is to find an *unbiased* signal estimate (rather than a minimum variance estimate), especially in the regime where the signal-to-noise is very large (e.g., on strong sources or when crossing the Galactic plane). A simple phase-binning procedure (corresponding to the idealized case where the sampling frequency is an integer multiple of the spin frequency) is not accurate enough for our purposes. Instead, we assume that the beam smoothing allows us to use a band-limited signal parametrization in phase space, and that the pointing matrix acts as an (irregular) sampler in phase space. The problem, then, is to compute these irregular samples to high accuracy in a reasonable time. The solution that we have adopted is to use a Fourier-Taylor (see [Colombi et al. 2009](#), and references therein) expansion of the phase Fourier modes to achieve the irregular sampling. Through simulations of different frequency channels, we found that the signal bias using this solution can be made arbitrarily small by increasing the order of the Taylor expansion. In practice, a 4th order expansion was sufficient to leave no signal residuals in the estimated noise time-streams.

C.1.4. Parametric estimation of the noise power

The noise power spectrum estimates in different frequency bins are expected to be mildly correlated. However, for wide frequency bins this correlation is expected to be small. We thus model the likelihood of a given parametrized model power spectrum as factorized over the frequency bins. Each (averaged) periodogram estimate is therefore modelled as χ^2 distributed, where the number of degrees of freedom is given by twice the number of periodograms used in the averaging (accounting for the cosine and sine mode for each periodogram frequency). The model power spectrum is then a simple scaling factor in the distribution.

The joint likelihood over all frequency bins is then maximized with respect to the parameters using a Levenberg-Marquardt algorithm. The user can choose to include or exclude any given number of frequency bins from the fit, which is useful if one wants to compute a simple noise power amplitude

²⁴ This reasoning implicitly assumes the circular stationarity of the noise on any given ring, whereas the noise covariance matrix is Toeplitz rather than circulant; therefore, we expect that a weighting scheme that takes into account edge effects would result in a slightly more optimal estimate of the signal.

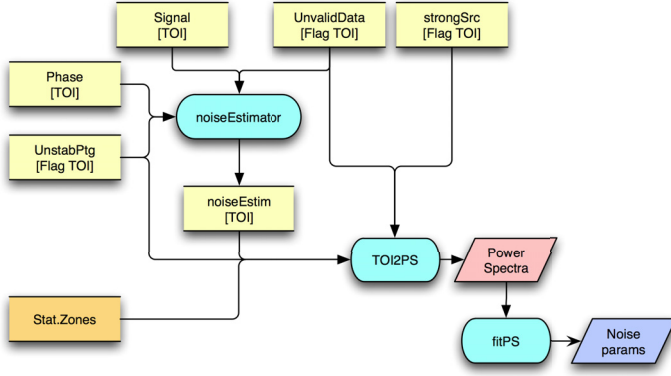


Fig. C.1. Schematic diagram of the noise estimation pipeline.

(e.g., a white noise model) by restricting the fitting procedure to the specific spectral range.

C.2. Implementation

The *detnoise* pipeline is implemented in Python using HFI DPC’s `THIN` library, and it is maintained under CVS in the `HL2_FMpipes` package. A block diagram of the pipeline for a single detector is shown in Fig. C.1. The pipeline consists of three modules:

- the *noiseEstim* module produces the TOIs of noise. For each ring, the valid (i.e. excluding glitched data and data obtained during periods of unstable pointing) input data are binned in phase and combined as described above to produce a phase-binned-ring, or PBR, containing the best estimate of the sky signal component. The PBR is defined to contain 10 822 bins, to match the detector sampling time²⁵. The signal PBR is then subtracted from the original input TOI by first interpolating it back onto the TOI, and then subtracting. This results in a timeline containing mostly noise;
- the *TOI2PS* module computes, for each ring, the power spectrum of the noise timeline. Within each ring, power spectra are computed over successive chunks of 2^p samples with, depending on the window function, some overlap between successive chunks. The power spectra are averaged, divided by the sampling frequency, and the square root of the result is returned as the spectrogram for the ring, which is in units of [units of the input noise TOI]/ $\sqrt{\text{Hz}}$. The length of the final spectrograms and the associated frequency resolution as a function of p is given in Table (C.1). The value $p = 18$ is used for the sample spectra shown below. A flag TOI is used to specify which data samples to skip. This same flag is then used to correct the empirical autocorrelation function (Fourier transform of the reversed periodogram) by the autocorrelation of the gaps;
- the *fitPS* module fits one of several noise models to the ring spectra. The simplest model is pure white noise within a given spectral range,

$$P(f; \sigma) = \sigma^2. \quad (\text{C.10})$$

A more complex model includes low frequency $1/f$ noise,

$$P(f; \sigma, f_{\text{knee}}, \alpha) = \sigma^2(1 + (f_{\text{knee}}/f)^\alpha), \quad (\text{C.11})$$

²⁵ Note that since the satellite’s spin rate varies by $\pm \sim 0.05$ s peak-to-peak around the nominal rate of 1 rpm, there is not a perfect match between the sampling time, which is fixed in time, and the bin size, which is fixed in space.

Table C.1. Length of the data chunks ($=2^p$) on which the power spectra are computed and the associated minimum frequency, F_{min} .

p	Length	F_{min}
10	5.68 s	176.2 mHz
12	22.7 s	44.04 mHz
14	1.51 min	11.01 mHz
16	6.06 min	2.752 mHz
17	12.1 min	1.376 mHz
18	24.2 min	0.688 mHz

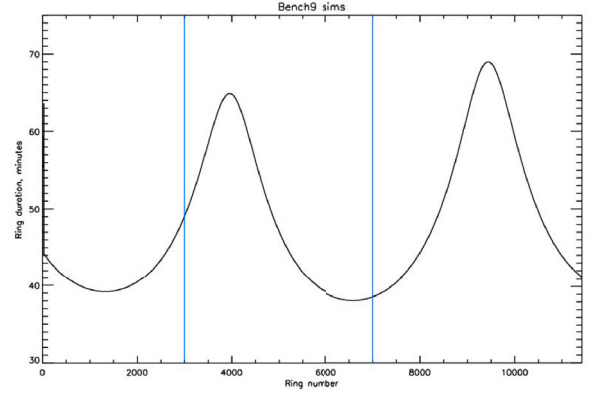


Fig. C.2. Length of pointing periods in the simulations. The vertical blue lines indicate the range of rings used.

where α is the slope of the $1/f$ component, and f_{knee} is an effective “knee-frequency”. Finally, we have also implemented a three parameter model including photon and phonon noise

$$P(f; \sigma_b, \sigma_p, \tau) = \sigma_b^2 + \sigma_p^2/[1 + (2\pi\tau f)^2], \quad (\text{C.12})$$

where σ_b and σ_p are the white noise components due to photons and phonons, respectively, and τ is a phonon time constant.

C.3. Results on simulated data

The pipeline was tested extensively on simulations that include the full sky signal (CMB, Galaxy, point sources). The noise of the HFI instrument is modelled by Eq. (C.11). The details are presented in [Planck Collaboration \(2011v\)](#), but a brief description is given here for completeness.

The results given below were obtained from simulations that used a mission-like scanning strategy, in which the ring length varied with time, as shown in Fig. C.2. The analysis was performed over rings 3000–7000, indicated by the blue vertical lines in the figure. Four detectors at different frequencies were studied, all of which showed the behaviour reported below.

C.3.1. Effects on the spectra

The noise estimator can be applied to the sky+noise timeline or to the pure noise timeline. The differences between the two are negligible except when the timeline includes very strong sources (planets or, at high frequencies, the central regions of the Galactic plane). Below we report results on the noise estimator obtained from the pure noise timeline.

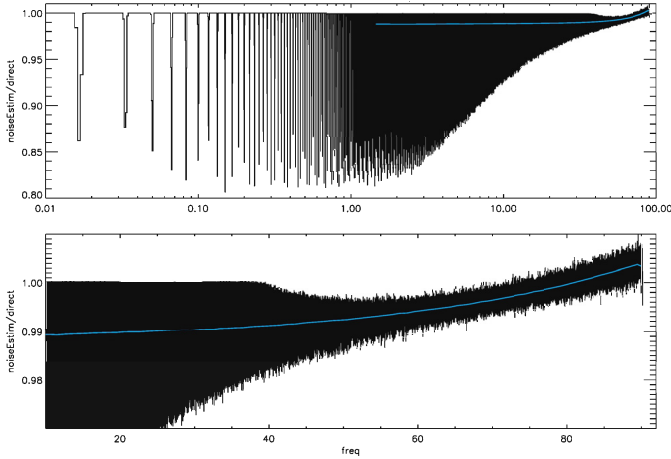


Fig. C.3. Ratio of the power spectra obtained on the noise estimator timeline to that from the input noise timeline. *Top*: on a logarithmic frequency scale, to emphasise the effect at low frequency. *Bottom*: on a linear frequency scale. The blue line is the same spectrum smoothed to 1 Hz resolution to show the mean value of the bias.

This bias is best determined by comparing the spectrum of the noise estimator to that of the input noise TOI. To accentuate the difference, we compare the average (in quadrature) of 4000 ring spectra. The ratio of the two power spectra is shown in Fig. C.3 and displays dips at multiples of the spin frequency. These dips arise from the particular ring-based scanning strategy of *Planck*. In the case of an idealized scanning where the sampling frequency is an integer multiple of the spin frequency, the signal subtraction operation would remove all power at spin-harmonic frequencies, and leave other frequencies of the timeline untouched. Since this idealized situation is not realized in practice, the spin-harmonic frequencies do not coincide exactly with the discrete (time) frequencies of the periodogram, and the dips (decrement of power around spin harmonics) acquire wings.

The white noise level is measured, in practice, in the 1–3 Hz region of the spectra to avoid the rise due to the $1/f$ component at lower frequencies and the rise caused by the time constant deconvolution at higher frequencies. The bias in the white noise level measured from the 1–3 Hz range is $\sim 1\%$. This bias can also be determined by comparing the mean and the median value of the spectrum in the desired frequency range. Provided the spectral resolution is sufficiently high, as is the case in the region selected, the median will reflect that level of the “continuum” which is identical to the noise level measured directly on the pure noise timelines.

C.3.2. Comparison to expected values

The input noise timeline is computed using detector-specific input NET and ϵ (cross-polar leakage) values that are stored in an instrument database. Given those input parameters, the NET measured from the noise estimation pipeline is expected to be:

$$\text{NET}_{\text{out}} = 0.5 \sqrt{2} (1 + \epsilon) \text{NET}_{\text{in}}. \quad (\text{C.13})$$

The simulations agree with this expectation to much better than 1% once the bias in the noise estimator described above is corrected.

Appendix D: Determination of the effective beams

Pure analytical approaches to the effect of asymmetrical beams, as in Fosalba et al. (2002) are illuminating, but are usually of

limited accuracy due to a number of simplifying assumptions. This appendix provides some details on the results with the two approach which we have developed to deal in practice with *Planck* data, FEBeCoP and FICSBell.

D.1. The FEBeCoP method

The “Fast Effective Beam Convolution in Pixel space” algorithm, referred to as FEBeCoP, and associated software to derive the effective beams appropriate to a fixed observing period of the *Planck* mission is described in detail in Mitra et al. (2011). FEBeCoP uses a record of detector pointings and a mathematical model of the scanning beam (either as an analytical function or a numerical table of the scanning beam values) to produce a data object of effective beams computed over a few hundred pixels centred at every pixel of the sky map produced from the detector pointings. After this large data object is computed, a convolution of the full sky input signal with the spatially varying effective beam becomes a numerically fast contraction of the stored beam with the sky model. Further, once the effective beam data object is computed, the point spread function in any specific direction on the sky can easily be extracted and utilized in the analysis of the compact sources detected in the *Planck* sky maps.

We present two sets of results for the effective beams. The first set is based upon the elliptical Gaussian scanning beams and the second uses a truncated Gauss-Hermite series, as described in Sect. 6.1.2.

Figures D.1 and D.2 shows images at 143 and 857 GHz of four sources from the ERCSC (detected at all six frequencies of the HFI) together with the FEBeCoP derived Point Spread Functions evaluated at the same locations on the sky. At frequencies of 353 GHz or less, the main errors in the FEBeCoP representation of the scanning beams are in the low-amplitude outer parts of the effective PSF. The 143 GHz PSFs plotted in Fig. D.1 represent *Planck*’s most sensitive frequency channel. These detectors also have the most symmetric beams. The multi-moded nature of the 857 GHz and 545 GHz channels leads to flat-topped beam profiles that are poorly described by an elliptical Gaussian. This is apparent in Fig. D.2 which show that the differences between the FEBeCoP results based on elliptical Gaussian versus Gauss-Hermite fits are more pronounced than at 143 GHz.

The *Planck* scanning strategy leads to large variations in the number of observations of a given map pixel and in the range of scanning beam orientations (see, for example, the “hit-count” maps plotted in Fig. 33). As a result, effective beams vary in size, shape, and orientation depending on location with no azimuthal or latitudinal symmetry. To give an impression of the range of these variations, we sampled the effective beams and PSFs at 3000 uniformly distributed locations on the sky. At each location we fitted an elliptical Gaussian to the FEBeCoP beam. We then constructed histograms of the fitted values of the FWHM (the geometric mean of the major and minor axes), ellipticity, and orientation with respect to the local meridian of the central pixel of the beam. Figure D.3 shows those histograms for the Gauss-Hermite fits to the scanning beams. Overall, we find a dispersion of few percent in the FWHM and ellipticity around the sky. Numerical values are given in the summary Table 4.

D.2. The FICSBell method

The FICSBell method (Hivon & Ponthieu, in prep.) generalizes to polarization and to include other sources of systematics the

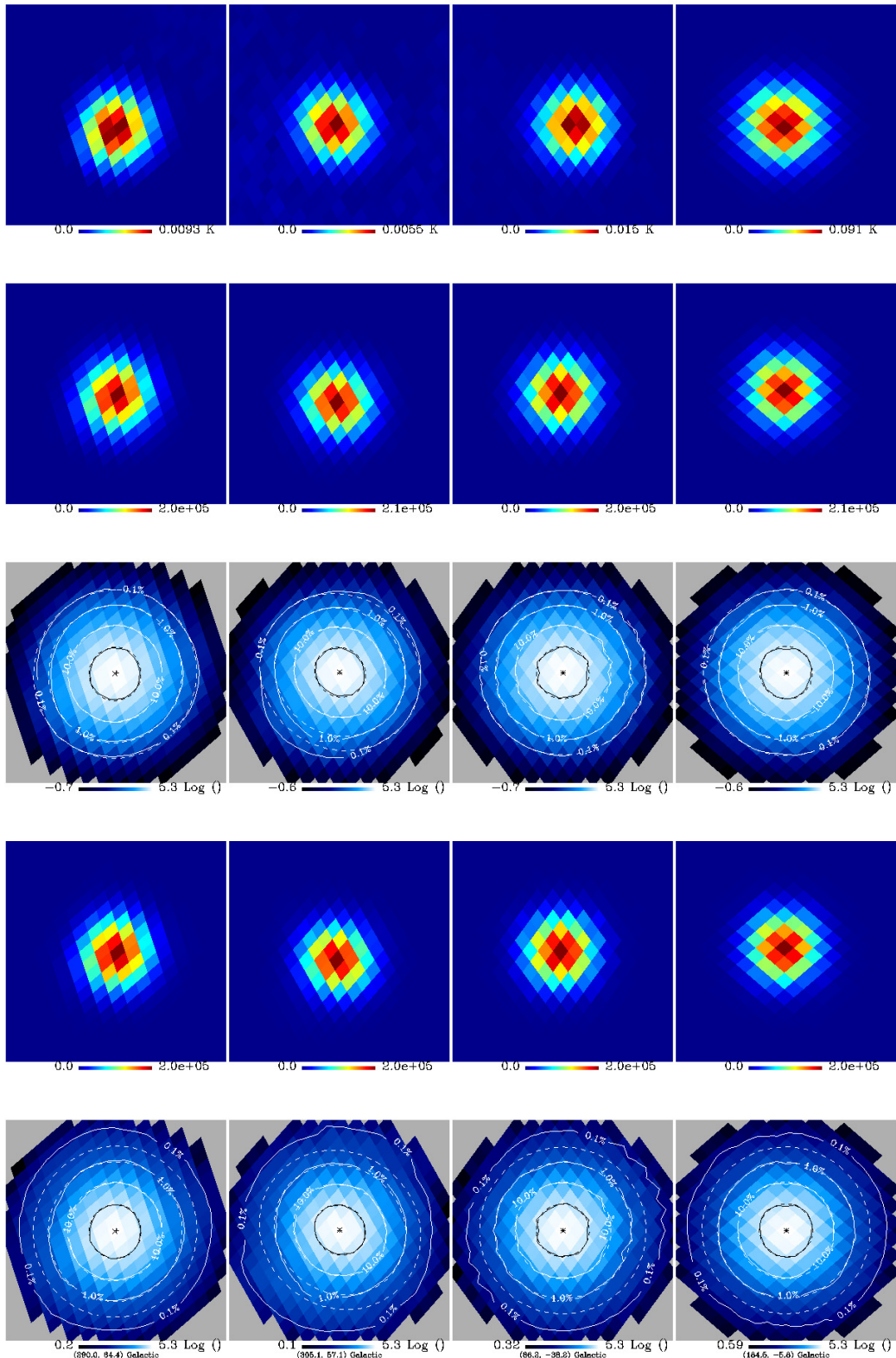


Fig. D.1. Images obtained at 143 GHz. Each column corresponds to one of four sources. **a)** The first row displays a zoom of the 143 GHz map around each source. **b)** The second row shows the FEBeCoP beam at that location, as computed when using the elliptical Gaussian description of the scanning beam derived from Mars observations. **c)** The third row shows on a logarithmic scale the same Point Spread Functions (PSF) with superimposed iso-contours shown in solid line, to be compared with elliptical Gaussian fit iso-contours shown in broken line. **d)** The fourth row shows the FEBeCoP beam at that location, as in b), when using instead the Gauss-Hermite description of the scanning beam in input. **e)** The fifth row shows as in c) the PSF on a logarithmic scale, for the Gauss-Hermite input.

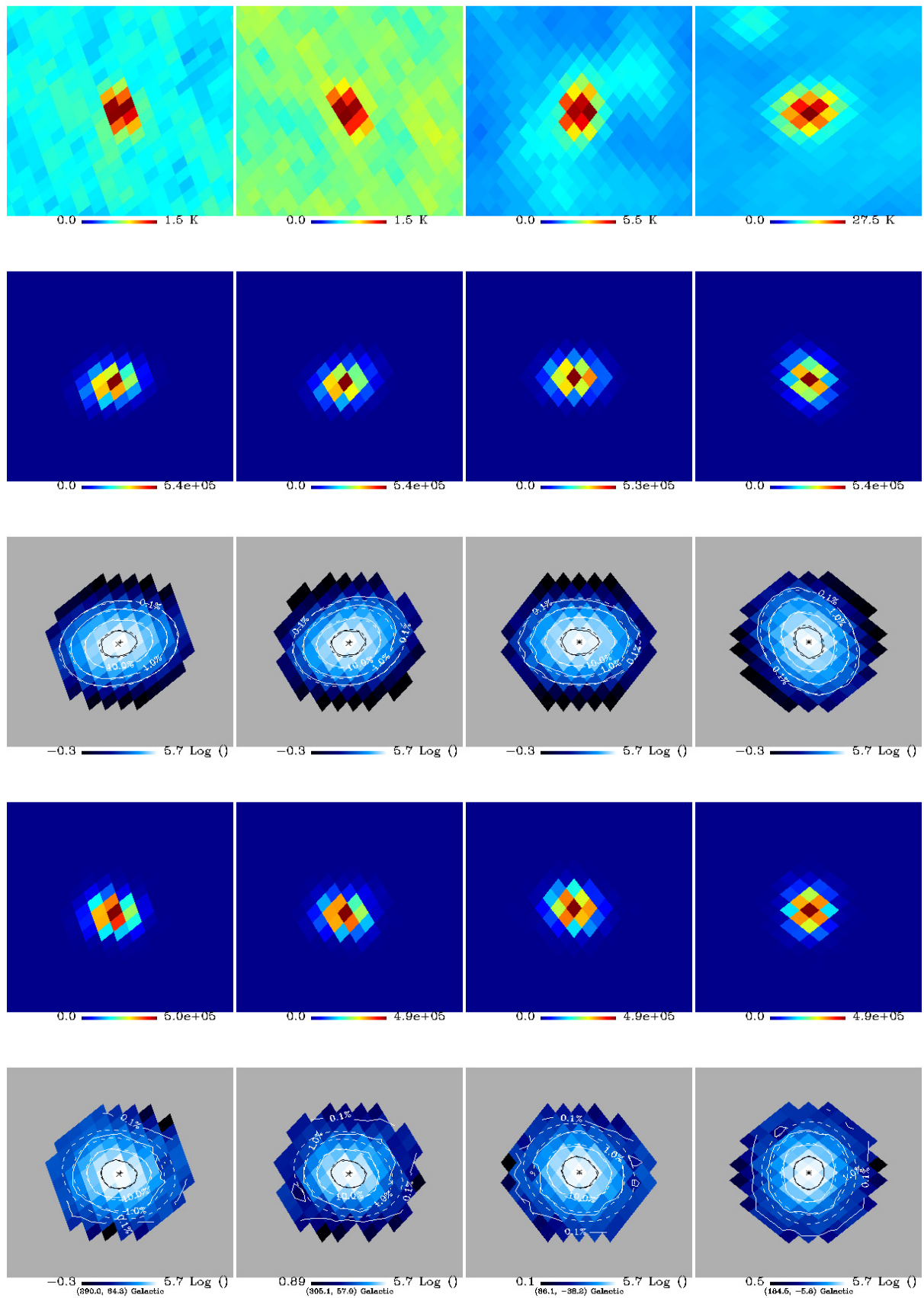


Fig. D.2. Images obtained at 857 GHz. The arrangement is the same than for the four sources at 143 GHz displayed in Fig. D.1.

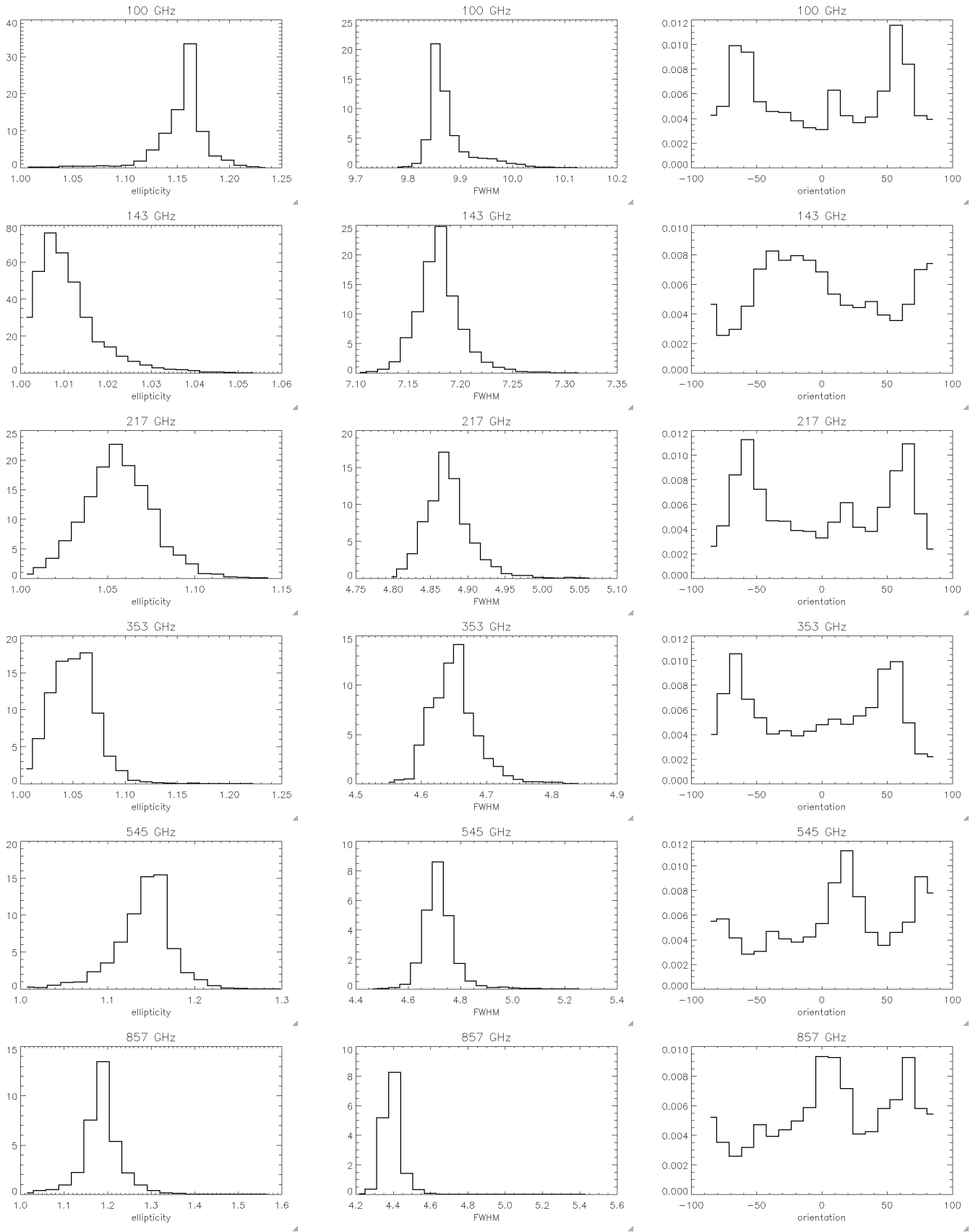


Fig. D.3. Statistics of the variation in ellipticity, effective beam width and orientation of elliptical Gaussian fits to the FEBeCoP beam pattern around the sky. These plots are for the Gauss-Hermite fits to the scanning beams.

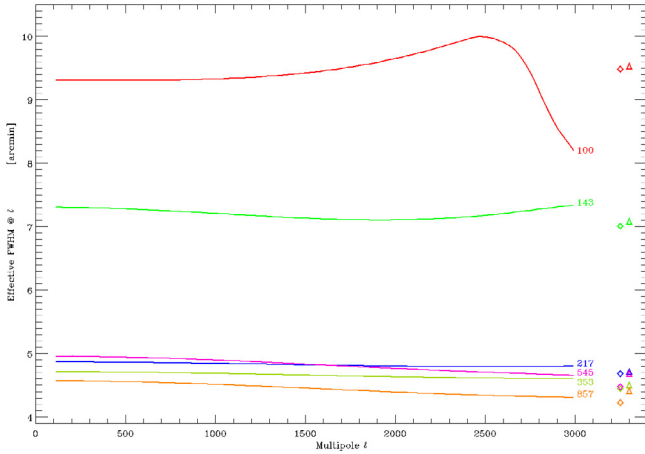


Fig. D.4. FWHM versus multipole of the Gaussian which would give the same value as effective beam transfer function at that multipole. The diamond at right gives the scanning FWHM obtained from Mars observations, and the triangle the value derived from our best estimate of the beam solid angle given in line b1 of the summary table (Table 4).

approach used for temperature power spectrum estimation in WMAP-3yr (Hinshaw et al. 2007) and by Smith et al. (2007) in the detection of CMB lensing in WMAP maps. The different steps of the method can be summarized as follows:

1. the scanning related information (i.e., statistics of the orientation of each detector within each pixel) is computed first, and only once for a given observation campaign. Those hit moments are only computed up to degree 4, for reasons described below;
2. the (Mars based) scanning beam beam map (or any beam model) of each detector d is analyzed into its Spherical Harmonics coefficients

$$b_{ls}^d = \int d\mathbf{r} B_d(\mathbf{r}) Y_{ls}(\mathbf{r}), \quad (\text{D.1})$$

where $B_d(\mathbf{r})$ is the beam map centred on the North pole, and $Y_{ls}(\mathbf{r})$ is the Spherical Harmonics basis function. Higher s indexes describes higher degrees of departure from azimuthal symmetry and, for HFI beams, the coefficients b_{ls}^d are decreasing functions of s at most multipoles. It also appears that, for $l < 3000$, the coefficients with $|s| > 4$ account for 1% or less of the beam throughput. For this reason, only modes with $|s| \leq 4$ are considered in the present analysis. Armitage-Caplan & Wandelt (2009) reached a similar conclusion in their deconvolution of Planck-LFI beams;

3. the b_{ls}^d coefficients computed above are used to generate s -spin weighted maps for a given CMB sky realization;
4. the spin weighted maps and hit moments of the same order s are combined for all detectors involved, to provide an “observed” map;
5. the power spectrum of this map can then be computed, and compared to the input CMB power spectrum to estimate the effective beam window function over the whole sky, or over a given region of the sky.

Monte-Carlo (MC) simulations in which the sky realisations are changed can be performed quickly by repeating steps 3, 4 and 5 only. The impact of beam model uncertainties can be studied by including step 2 into the MC simulations.

Figure D.4 shows that a Gaussian beam is a reasonably accurate approximation of the effective beam. Indeed one sees that

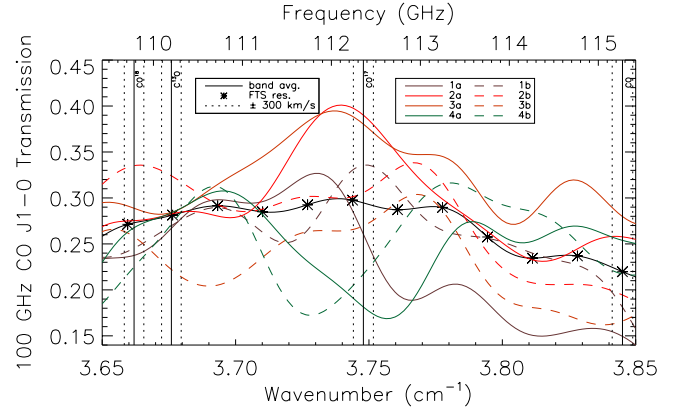


Fig. E.1. The spectral response for the CO J 1-0 transition region. The spectral resolution has been oversampled by a factor of ~ 10 for a window surrounding each of the CO transitions listed in Table E.1, the asterisks show the spacing of independent spectral data points. This region was selected to include the rest frequency ($\pm 300 \text{ km s}^{-1}$ – vertical dotted lines) for each of the CO, C^{13}O , CO^{17} , and CO^{18} isotopes. Also shown is the band average spectrum for each region.

on average the effective beam derived from the Mars scanning beam differs only little from a Gaussian, except for 100 GHz for which the scanning beam is quite elliptical. The 857 GHz scanning beams are also rather elliptical but this would show up at higher multipoles than those shown in the plot. In most cases the deviations are only at the $0.1'$ level, which is negligible for the analyses of the early results.

Appendix E: Band-pass measurements at the rest-frame frequency of CO lines

After launch it became apparent that the contribution of CO rotational transitions to the HFI measurements was greater than anticipated, especially for the 100 GHz band. To isolate the narrow CO features from the rest of the signal components (CMB, dust, etc.), precise knowledge of the instrument spectral response as a function of frequency is required. The original spectral resolution requirement for the spectral response measurements of a given HFI detector was $\sim 3 \text{ GHz}$; this corresponds to a velocity resolution of $\sim 8000 \text{ km s}^{-1}$ for the CO J 1-0 line. As *Planck* does not have the ability to measure absolute spectral response within a frequency band during flight, the ground-based FTS measurements may provide the most accurate data on the HFI spectral transmission. With good S/N , spectral information can be inferred to a fraction (i.e. $\sim 1/10$ th) of a spectral resolution element (Spencer et al. 2010). Thus, the Saturne FTS measurements (Pajot et al. 2010), which were carried out at a spectral resolution of $\sim 0.6 \text{ GHz}$, may be used to estimate the spectral response at a resolution equivalent to $\sim 150 \text{ km s}^{-1}$ for the CO J 1-0 line.

For spectral regions near CO rotational transitions, therefore, the spectral response was oversampled by a factor of ~ 10 using an interpolation based on the instrument line shape of the FTS. Table E.1 lists the relevant CO transitions, and the frequency ranges over which the HFI spectral response was oversampled. The oversampling ranges were extended to include all of the common CO isotopes. The vertical bars above the spectral response curves of Fig. 44 illustrate these oversampled regions. The spectral responses for the CO J 1-0 frequency range are shown in Fig. E.1; similar data is available for all of the CO transitions within HFI bands.

Table E.1. Rotational CO transitions within the HFI bands.

Band (GHz)	CO transition ($J_{\text{upper}} - J_{\text{lower}}$)	$\nu_{\text{rot}} \text{ } ^{12}\text{C}^{16}\text{O}$ (GHz)	Over-sampled region (GHz)
100	1–0	115.2712018	109.67–115.39
217	2–1	230.5380000	219.34–230.77
353	3–2	345.7959899	329.00–346.15
545	4–3	461.0407682	438.64–461.51
545	5–4	576.2679305	548.28–576.85
857	6–5	691.4730763	657.89–692.17
857	7–6	806.6518060	767.48–807.46
857	8–7	921.7997000	877.04–922.73
857	9–8	1036.9123930	986.57–1037.95

References

- Armitage-Caplan, C., & Wandelt, B. D. 2009, *ApJS*, 181, 533
- Ashdown, M. A. J., Baccigalupi, C., Balbi, A., et al. 2007, *A&A*, 467, 761
- Bersanelli, M., Mandolesi, N., Butler, R. C., et al. 2010, *A&A*, 520, A4
- Cardoso, J., Martin, M., Delabrouille, J., Betoule, M., & Patanchon, G. 2008, *IEEE Journal of Selected Topics in Signal Processing*, 2, 735, special issue on Signal Processing for Astronomical and Space Research Applications
- Colombi, S., Jaffe, A., Novikov, D., & Pichon, C. 2009, *MNRAS*, 393, 511
- Dalhaus, R. 1988, *The Annals of Statistics*, 16, 808
- Dame, T. M., Hartmann, D., & Thaddeus, P. 2001, *ApJ*, 547, 792
- Delabrouille, J. 1998, *A&AS*, 127, 555
- Delabrouille, J., Cardoso, J.-F., & Patanchon, G. 2003, *MNRAS*, 346, 1089
- Delabrouille, J., Cardoso, J., Le Jeune, M., et al. 2009, *A&A*, 493, 835
- Efstathiou, G. 2007, *MNRAS*, 380, 1621
- Ferreira, P. G., & Jaffe, A. H. 2000, *MNRAS*, 312, 89
- Finkbeiner, D. P., Davis, M., & Schlegel, D. J. 1999, *ApJ*, 524, 867
- Fixsen, D. J., Weiland, J. L., Brodd, S., et al. 1997, *ApJ*, 490, 482
- Fosalba, P., Doré, O., & Bouchet, F. R. 2002, *Phys. Rev. D*, 65, 063003
- Giorgini, J. D., Yeomans, D. K., Chamberlin, A. B., et al. 1996, *BAAS*, 28, 1158
- Górski, K. M., Hivon, E., Banday, A. J., et al. 2005, *ApJ*, 622, 759
- Haslam, C., Stoffel, H., Salter, C. J., & Wilson, W. E. 1982, *A&ASS*, 47, 1
- Hinshaw, G., Nolta, M. R., Bennett, C. L., et al. 2007, *ApJS*, 170, 288
- Hinshaw, G., Weiland, J. L., Hill, R. S., et al. 2009, *ApJS*, 180, 225
- Huffenberger, K. M., Crill, B. P., Lange, A. E., Górski, K. M., & Lawrence, C. R. 2010, *A&A*, 510, A58
- Kaiser, J. F. 1974, *Proc. IEEE Int. Symp. Circuit Theory*, 20
- Keihänen, E., Kurki-Suonio, H., Poutanen, T., Maino, D., & Burigana, C. 2004, *A&A*, 428, 287
- Keihänen, E., Kurki-Suonio, H., & Poutanen, T. 2005, *MNRAS*, 360, 390
- Lamarre, J., Puget, J., Ade, P. A. R., et al. 2010, *A&A*, 520, A9
- Leach, S. M., Cardoso, J., Baccigalupi, C., et al. 2008, *A&A*, 491, 597
- Macías-Pérez, J. F., Lagache, G., Maffei, B., et al. 2007, *A&A*, 467, 1313
- Maino, D., Burigana, C., Górski, K. M., Mandolesi, N., & Bersanelli, M. 2002, *A&A*, 387, 356
- Mandolesi, N., Bersanelli, M., Butler, R. C., et al. 2010, *A&A*, 520, A3
- Mennella, A., Butler, R. C., Curto, A., et al. 2011, *A&A*, 536, A3
- Mitra, S., Rocha, G., Górski, K. M., et al. 2011, *ApJS*, 193, 5
- Onishi, T., Mizuno, A., Kawamura, A., Tachihara, K., & Fukui, Y. 2002, *ApJ*, 575, 950
- Pajot, F., Ade, P. A. R., Beney, J., et al. 2010, *A&A*, 520, A10
- Planck Collaboration 2011a, *A&A*, 536, A1
- Planck Collaboration 2011b, *A&A*, 536, A2
- Planck Collaboration 2011c, *A&A*, 536, A7
- Planck Collaboration 2011d, *A&A*, 536, A8
- Planck Collaboration 2011e, *A&A*, 536, A9
- Planck Collaboration 2011f, *A&A*, 536, A10
- Planck Collaboration 2011g, *A&A*, 536, A11
- Planck Collaboration 2011h, *A&A*, 536, A12
- Planck Collaboration 2011i, *A&A*, 536, A13
- Planck Collaboration 2011j, *A&A*, 536, A14
- Planck Collaboration 2011k, *A&A*, 536, A15
- Planck Collaboration 2011l, *A&A*, Vol., A16
- Planck Collaboration 2011m, *A&A*, 536, A17
- Planck Collaboration 2011n, *A&A*, 536, A18
- Planck Collaboration 2011o, *A&A*, 536, A19
- Planck Collaboration 2011p, *A&A*, 536, A20
- Planck Collaboration 2011q, *A&A*, 536, A21
- Planck Collaboration 2011r, *A&A*, 536, A22
- Planck Collaboration 2011s, *A&A*, 536, A23
- Planck Collaboration 2011t, *A&A*, 536, A24
- Planck Collaboration 2011u, *A&A*, 536, A25
- Planck Collaboration 2011v, *The Explanatory Supplement to the Planck Early Release Compact Source Catalogue (ESA)*
- Planck Collaboration 2011w, *A&A*, 536, A26
- Planck HFI Core Team 2011a, *A&A*, 536, A4
- Planck HFI Core Team 2011b, *A&A*, 536, A6
- Reinecke, M. 2011, *A&A*, 526, A108
- Reinecke, M., Dolag, K., Hell, R., Bartelmann, M., & Enßlin, T. A. 2006, *A&A*, 445, 373
- Revenu, B., Kim, A., Ansari, R., et al. 2000, *A&AS*, 142, 499
- Rosset, C., Tristram, M., Ponthieu, N., et al. 2010, *A&A*, 520, A13
- Schlegel, D. J., Finkbeiner, D. P., & Davis, M. 1998, *ApJ*, 500, 525
- Shoemake, K. 1985, in *SIGGRAPH '85: Proc. 12th annual Conf. on Computer graphics and interactive techniques* (New York, NY, USA: ACM), 245
- Shuster, M. D. 1993, *J. Astronaut. Sci.*, 41, 439
- Smith, K. M., Zahn, O., & Doré, O. 2007, *Phys. Rev. D*, 76, 043510
- Spencer, L. D., Naylor, D. A., & Swinyard, B. M. 2010, *Measurement Science and Technology*, 21, 065601
- Stute, T. 2004, in *SPIE Conf. Ser. 5495*, ed. J. Antebi, & D. Lemke, 1
- Tauber, J. A., Mandolesi, N., Puget, J., et al. 2010, *A&A*, 520, A1
- Tristram, M., Macías-Pérez, J. F., Renault, C., & Santos, D. 2005, *MNRAS*, 358, 833
- Tristram, M., Filliard, C., Perdureau, O., et al. 2011, *A&A*, 534, A88
- Viterbi, A. 1967, *IEEE Trans. Inform. Theor.*, 13, 260
- Walraven, R. 1984, *Proc. of the Digital Equipment User's Society*, Fall 1984
- Zacchei, A., Maino, D., Baccigalupi, C., et al. 2011, *A&A*, 536, A5

¹ Agenzia Spaziale Italiana Science Data Center, c/o ESRIN, via Galileo Galilei, Frascati, Italy

² Astroparticule et Cosmologie, CNRS (UMR7164), Université Denis Diderot Paris 7, Bâtiment Condorcet, 10 rue A. Domon et Léonie Duquet, Paris, France

³ Astrophysics Group, Cavendish Laboratory, University of Cambridge, J J Thomson Avenue, Cambridge CB3 0HE, UK

⁴ Atacama Large Millimeter/submillimeter Array, ALMA Santiago Central Offices, Alonso de Cordova 3107, Vitacura, Casilla 763 0355, Santiago, Chile

⁵ CITA, University of Toronto, 60 St. George St., Toronto, ON M5S 3H8, Canada

⁶ CNRS, IRAP, 9 Av. colonel Roche, BP 44346, 31028 Toulouse Cedex 4, France

⁷ California Institute of Technology, Pasadena, California, USA

⁸ DAMTP, University of Cambridge, Centre for Mathematical Sciences, Wilberforce Road, Cambridge CB3 0WA, UK

⁹ DSM/Irfu/SPP, CEA-Saclay, 91191 Gif-sur-Yvette Cedex, France

¹⁰ DTU Space, National Space Institute, Juliane Mariesvej 30, Copenhagen, Denmark

¹¹ Département de Physique Théorique, Université de Genève, 24 Quai E. Ansermet, 1211 Genève 4, Switzerland

¹² Department of Astronomy and Astrophysics, University of Toronto, 50 Saint George Street, Toronto, Ontario, Canada

¹³ Department of Physics, Princeton University, Princeton, New Jersey, USA

¹⁴ Department of Physics, University of California, One Shields Avenue, Davis, California, USA

- ¹⁵ Department of Physics, University of Illinois at Urbana-Champaign, 1110 West Green Street, Urbana, Illinois, USA
- ¹⁶ Department of Physics, University of Oxford, 1 Keble Road, Oxford, UK
- ¹⁷ Dipartimento di Fisica, Università La Sapienza, P.le A. Moro 2, Roma, Italy
- ¹⁸ Dipartimento di Fisica, Università degli Studi di Milano, via Celoria 16, Milano, Italy
- ¹⁹ European Southern Observatory, ESO Vitacura, Alonso de Cordova 3107, Vitacura, Casilla 19001, Santiago, Chile
- ²⁰ European Space Agency, ESTEC, Keplerlaan 1, 2201 AZ Noordwijk, The Netherlands
- ²¹ INAF - Osservatorio Astronomico di Trieste, via G.B. Tiepolo 11, Trieste, Italy
- ²² INAF/IASF Bologna, via Gobetti 101, Bologna, Italy
- ²³ INAF/IASF Milano, via E. Bassini 15, Milano, Italy
- ²⁴ INSU, Institut des sciences de l'univers, CNRS, 3 rue Michel-Ange, 75794 Paris Cedex 16, France
- ²⁵ IPAG: Institut de Planétologie et d'Astrophysique de Grenoble, Université Joseph Fourier, Grenoble 1 / CNRS-INSU, UMR 5274, 38041 Grenoble, France
- ²⁶ Imperial College London, Astrophysics group, Blackett Laboratory, Prince Consort Road, London, SW7 2AZ, UK
- ²⁷ Infrared Processing and Analysis Center, California Institute of Technology, Pasadena, CA 91125, USA
- ²⁸ Institut Néel, CNRS, Université Joseph Fourier Grenoble I, 25 rue des Martyrs, Grenoble, France
- ²⁹ Institut d'Astrophysique Spatiale, CNRS (UMR8617) Université Paris-Sud 11, Bâtiment 121, Orsay, France
- ³⁰ Institut d'Astrophysique de Paris, CNRS UMR7095, Université Pierre & Marie Curie, 98bis boulevard Arago, Paris, France
- ³¹ Institut de Ciències de l'Espai, CSIC/IEEC, Facultat de Ciències, Campus UAB, Torre C5 par-2, Bellaterra 08193, Spain
- ³² Institut de Radioastronomie Millimétrique (IRAM), Avenida Divina Pastora 7, Local 20, 18012 Granada, Spain
- ³³ Institut de Radioastronomie Millimétrique (IRAM), Domaine Universitaire de Grenoble, 300 rue de la Piscine, 38406 Grenoble, France
- ³⁴ Institute of Astronomy, University of Cambridge, Madingley Road, Cambridge CB3 0HA, UK
- ³⁵ Instituto de Astrofísica de Canarias, C/Vía Láctea s/n, La Laguna, Tenerife, Spain
- ³⁶ Jet Propulsion Laboratory, California Institute of Technology, 4800 Oak Grove Drive, Pasadena, California, USA
- ³⁷ Jodrell Bank Centre for Astrophysics, Alan Turing Building, School of Physics and Astronomy, The University of Manchester, Oxford Road, Manchester, M13 9PL, UK
- ³⁸ Kavli Institute for Cosmology Cambridge, Madingley Road, Cambridge, CB3 0HA, UK
- ³⁹ LERMA, CNRS, Observatoire de Paris, 61 Ave de l'Observatoire, Paris, France
- ⁴⁰ Laboratoire AIM, IRFU/Service d'Astrophysique - CEA/DSM - CNRS - Université Paris Diderot, Bât. 709, CEA-Saclay, 91191 Gif-sur-Yvette Cedex, France
- ⁴¹ Laboratoire Traitement et Communication de l'Information, CNRS (UMR 5141) and Télécom ParisTech, 46 rue Barrault, 75634 Paris Cedex 13, France
- ⁴² Laboratoire d'Astrophysique de Marseille, 38 rue Frédéric Joliot-Curie, 13388, Marseille Cedex 13, France
- ⁴³ Laboratoire de Physique Subatomique et de Cosmologie, CNRS/IN2P3, Université Joseph Fourier Grenoble I, Institut National Polytechnique de Grenoble, 53 rue des Martyrs, 38026 Grenoble Cedex, France
- ⁴⁴ Laboratoire de l'Accélérateur Linéaire, Université Paris-Sud 11, CNRS/IN2P3, Orsay, France
- ⁴⁵ Lawrence Berkeley National Laboratory, Berkeley, California, USA
- ⁴⁶ Max-Planck-Institut für Astrophysik, Karl-Schwarzschild-Str. 1, 85741 Garching, Germany
- ⁴⁷ National University of Ireland, Department of Experimental Physics, Maynooth, Co. Kildare, Ireland
- ⁴⁸ Observational Cosmology, Mail Stop 367-17, California Institute of Technology, Pasadena, CA, 91125, USA
- ⁴⁹ Optical Science Laboratory, University College London, Gower Street, London, UK
- ⁵⁰ Rutherford Appleton Laboratory, Chilton, Didcot, UK
- ⁵¹ SUPA, Institute for Astronomy, University of Edinburgh, Royal Observatory, Blackford Hill, Edinburgh EH9 3HJ, UK
- ⁵² School of Physics and Astronomy, Cardiff University, Queens Buildings, The Parade, Cardiff, CF24 3AA, UK
- ⁵³ Space Research Institute (IKI), Russian Academy of Sciences, Profsoyuznaya Str, 84/32, 117997 Moscow, Russia
- ⁵⁴ Space Sciences Laboratory, University of California, Berkeley, California, USA
- ⁵⁵ Stanford University, Dept of Physics, Varian Physics Bldg, 382 via Pueblo Mall, Stanford, California, USA
- ⁵⁶ Universität Heidelberg, Institut für Theoretische Astrophysik, Albert-Überle-Str. 2, 69120 Heidelberg, Germany
- ⁵⁷ Université de Toulouse, UPS-OMP, IRAP, 31028 Toulouse Cedex 4, France
- ⁵⁸ Universities Space Research Association, Stratospheric Observatory for Infrared Astronomy, MS 211-3, Moffett Field, CA 94035, USA
- ⁵⁹ University of Granada, Departamento de Física Teórica y del Cosmos, Facultad de Ciencias, Granada, Spain
- ⁶⁰ University of Miami, Knight Physics Building, 1320 Campo Sano Dr., Coral Gables, Florida, USA
- ⁶¹ Warsaw University Observatory, Aleje Ujazdowskie 4, 00-478 Warszawa, Poland